EVOLUTION OF THE LUNAR CRUST RECORDED IN THE METEORITIC FELDSPATHIC REGOLITH BRECCIAS NORTHWEST AFRICA 10291 AND 11182: INSIGHTS INTO THE HETEROGENEITY AND PETROGENESIS OF CRUSTAL LITHOLOGIES USING PETROLOGY AND MINERAL CHEMISTRY

By

SHANNON BOYLE

A thesis submitted to the

School of Graduate Studies

Rutgers, The State University of New Jersey

In partial fulfillment of the requirements

For the degree of

Master of Science

Graduate Program in Earth and Planetary Science

Written under the direction of

Doctor Juliane Gross

And approved by

_____

_____

_____

_____

New Brunswick, New Jersey

October 2019

ABSTRACT OF THE THESIS

Evolution of the lunar crust recorded in the meteoritic feldspathic regolith breccias Northwest Africa 10291 and 11182: Insights into the heterogeneity and petrogenesis of crustal lithologies using petrology and mineral chemistry

by SHANNON BOYLE

Thesis Director:

Doctor Juliane Gross

The geology of the Moon represents nearly a continuous geological record from its formation during the giant impact that resulted in the Earth-Moon system, to its state today. Therefore, it is a prime location for understanding one path of planetary evolution. Lunar meteorites are on average samples of rock and regolith from random areas on the lunar surface. As such, they represent our best available tools to study the crustal evolution of the Moon because they provide data on lunar petrology, geochemistry, and chronology, as well as data on the variety of existing lunar lithologies different from Apollo and Luna mission sample return sites. We investigated two lunar feldspathic regolith breccias found in 2017, Northwest Africa (NWA) 10291 and NWA 11182, to understand their petrogenetic origin and, more broadly, the evolution of lithologies present in unsampled areas of the Moon and place constraints on lunar crustal evolution in these areas. Both meteorites experienced terrestrial weathering, NWA 10291 less so than NWA 11182. NWA 10291 contains a variety of lithic clasts from the lunar highlands ranging from anorthosites to norites and gabbronorites, to pyroxenites. The matrix is mostly dominated by pyroxene grains that mostly have a very low Ti-basalt signature. In addition, NWA

10291 contains mineral grain fragments in the matrix of zircon, silica, and Na- and K-rich plagioclase. The bulk composition of other meteorites paired with NWA 10291, however, show low Th and low FeO content, indicating that this meteorite may have originated from the lunar farside feldspathic highland terrane (FHT), within the vicinity of South Pole Aitken basin. In contrast, most clasts in NWA 11182 are granulites, impact melt breccias, or recrystallized impact melt. They show a large compositional variation in Mg# ranging from hyperferroan (Mg# ~40) to highly magnesian (Mg# 80); however, a bimodal distribution between ferroan anorthosites (FAN) and magnesium-anorthosites (MAN) was identified using the Lilliefors test at the 95 and 99% confidence level. Judging from the lack of KREEP and presence of both FAN and MAN lithologies, NWA 11182 most likely originated from a region far from the Procellarum KREEP Terrane, between the lunar farside highland terrane (more Mg-rich) and the nearside highland terrane (more ferroan). Future bulk composition measurements could be used to further constrain the source regions of both meteorites.

TABLE OF CONTENTS

TITLE PAGE _____ i

ABSTRACT _____ ii

ACKNOWLEDGMENT _____ vi

LIST OF TABLES _____ vii

LIST OF FIGURES _____ viii

INTRODUCTION _____ 1

METHOD _____ 10

Qualitative elemental X-ray mapping _____ 10

Quantitative point analyses _____ 10

Statistical Analyses _____ 11

SAMPLE _____ 13

NWA 10291 _____ 13

NWA 11182 _____ 13

RESULTS _____ 15

Clast definitions _____ 15

NWA 10291 _____ 15

Petrography and mineral chemistry _____ 15

Lithic clasts _____ 17

Impact-related clasts _____ 20

Mineral grains _____ 21

NWA 11182 22

Petrography and mineral chemistry 22

Lithic clasts 22

Impact-related clasts 24

Mineral grains 25

DISCUSSION 27

Verification of lunar origin 27

Evidence of terrestrial weathering 28

Maturity and pristinity of NWA 10291 and 11182 31

Origin and affinity of clasts and mineral grains in NWA 10291 and 11182 to known lunar rock suites 33

Origin and heritage of NWA 10291 and 11182 to crustal source regions on the Moon 39

CONCLUSION 47

REFERENCES 49

ACKNOWLEDGMENT

I would like to thank all the people responsible for the completion of this project: my advisor Doctor Juliane Gross for her insight and guidance; my committee for their time and assistance; the Graduate School and the Department of Earth and Planetary Science for funding this project; my husband Neil for all those coffee runs and loving words; my parents John and Patricia for their everlasting support and Rita's care packages; my siblings Kelly and Sean for being some of the best role models I know; and my friends for the laughs and Omega runs.

LIST OF TABLES

Table 1: Electron microprobe conditions for mapping and data collection. 62

Table 2: Nomenclature used to describe clasts in NWA 10291 and 11182. 63

Table 3: Inventory of clasts measured in NWA 10291 and NWA 11182. 64

Table 4: Averaged chemistry of olivine, plagioclase, and pyroxene in mafic clasts in NWA 10291. 65

Table 5: Averaged chemistry of pyroxene and plagioclase in representative clasts in NWA 11182. 72

Table 6: Fe/Mn ratio of olivine in NWA 10291 and NWA 11182. 74

Table 7: Fe/Mn ratio of pyroxene in NWA 10291 and NWA 11182. 75

LIST OF FIGURES

Figure 1: Structure of the lunar regolith. 76

Figure 2: Full Back Scattered Electron (BSE) image of NWA 10291. 77

Figure 3: Full Back Scattered Electron (BSE) image of NWA 11182. 78

Figure 4: BSE images of representative lithic clasts in NWA 10291. 79

Figure 5: BSE images of representative impact-related clasts in NWA 10291. 80

Figure 6: BSE images of representative lithic clasts in NWA 11182. 81

Figure 7: BSE images of representative impact-related clasts in NWA 11182. 82

Figure 8: BSE images of altered olivine mineral grain in lunar NWA 11182 and L6 chondrite Forrest 009. 83

Figure 9: Mafic mineral chemistry of lithic clasts in NWA 10291. 84

Figure 10: Plagioclase mineral chemistry of lithic clasts in NWA 10291. 85

Figure 11: Mafic mineral chemistry of impact-related clasts in NWA 10291. 86

Figure 12: Plagioclase mineral chemistry of impact-related clasts in NWA 10291. 87

Figure 13: Mafic mineral chemistry of mineral grains in NWA 10291. 88

Figure 14: Plagioclase mineral chemistry of mineral grains in NWA 10291. 89

Figure 15: Mafic mineral chemistry of lithic clasts in NWA 11182. 90

Figure 16: Plagioclase mineral chemistry of lithic clasts in NWA 11182. 91

Figure 17: Mafic mineral chemistry of impact-related clasts in NWA 11182. 92

Figure 18: Plagioclase mineral chemistry of impact-related clasts in NWA 11182. 93

Figure 19: Mafic mineral chemistry of mineral grains in NWA 11182. 94

Figure 20: Plagioclase mineral chemistry of mineral grains in NWA 11182. 95

Figure 21: Fe/Mn ratio of pyroxene and olivine in NWA 10291 and NWA 11182. 96

Figure 22: Energy Dispersive Spectroscopy (EDS) spectra of barite grains in NWA 11182. __ 97

Figure 23: Energy Dispersive Spectroscopy (EDS) spectra of barite vein in NWA 11182. ___ 98

Figure 24: An/Mg# of lithic clasts in NWA 10291 and 11182. _____ 99

Figure 25: An/Mg# of impact-related clasts in NWA 10291 and 11182._____ 100

Figure 26: Ni/Co ratios in Fe-Ni metal in NWA 10291 and 11182._____ 101

Figure 27: TiO_2/FeO of silica-phases in NWA 10291._____ 102

Figure 28: Bulk composition of meteorites paired to NWA 10291._____ 103

Figure 29: Potential Highland lithology parentage of pyroxene mineral grains, granulites, and recrystallized impact melt in NWA 10291 and 11182._____ 104

Figure 30: Potential basaltic parentage for pyroxene mineral grains in NWA 10291 and 11182. _____ 105

INTRODUCTION

The Moon is a prime location to investigate planetary evolution because it represents nearly a continuous geologic record (Taylor and McLennan, 2009; Gross and Joy, 2016; Pernet-Fisher and Joy, 2016). Current models of terrestrial planetary formation and differentiation processes rely heavily on paradigms crafted during the Apollo era (NRC, 2007; Elkins-Tanton, 2008). Within a year of the return of Apollo 11, the concept of a magma ocean was formed (Smith et al., 1970; Wood et al., 1970) and it is still the favored model of the thermal evolution of rocky bodies (e.g. Elkins-Tanton, 2012). The Apollo 11 samples, along with data from pre-Apollo landers, revealed a large amount of Ca-rich plagioclase (anorthite) across the lunar surface (Smith et al., 1970; Wood et al., 1970). Early studies concluded that there must have been large-scale melting to account for the immense volume of surficial anorthite (Smith et al., 1970; Wood et al., 1970; Warren, 1993). This differentiation process was termed the lunar magma ocean.

The lunar magma ocean describes a cooling sequence from a largely melted Moon to a stratified and solidified Moon (Smith et al., 1970; Wood et al., 1970; Shearer et al., 2006 and references therein; Elardo, 2016). The cooling process took 10 to 10s of millions of years (Elkins-Tanton et al., 2011) and produced a crust, mantle, and core (Smith et al., 1970; Wood et al., 1970; Taylor and Jakes, 1974; Elkins-Tanton, 2012). Dense elements, such as iron and nickel, sank to form the core. The remaining melt formed Mg- and Fe-rich silicate minerals (olivine and pyroxene), beginning with Mg-rich olivine, followed by low-Ca-pyroxene, then high-Ca pyroxene. The olivine and pyroxene crystals were denser than the melt and therefore they settled out of the liquid and formed a silicate mantle with density of ~3400 kg m^{-3} according to models and remote sensing (Grimm, 2013). Calcium-rich plagioclase began forming after 74-

80% crystallization of the melt (Elkins-Tanton et al., 2011; Rapp and Draper, 2018). The plagioclase crystals were less dense (~2900 kg m^{-3}) than the surrounding liquid and therefore floated to the surface (Grimm, 2013). This plagioclase formed a floatation crust composed of ferroan anorthosite (FAN); a rock type prevalent in Apollo samples and lunar meteorites, typified by Fe enrichment in olivine or pyroxene (Mg# = 100*Mg/(Mg+Fe) = ~50-70) and a narrow range of Ca composition in plagioclase (An = 100*Ca/(Ca+Na) = ~94-97) (e.g. Smith et al., 1970; Wood et al., 1970; Dowty et al., 1974; Taylor and Jakes, 1974; Taylor, 1982; Warren, 1985; Shearer et al., 2006 and references therein). The remaining liquid between the settling mantle and floating crust formed a material rich in incompatible elements, such as U and Th, called KREEP (potassium, rare-earth elements, and phosphorous) (e.g. Warren 1985; Shearer et al., 2006).

Magmatism on the Moon continued in the form of intrusive and extrusive volcanism after mantle overturn (e.g. Shearer et al., 2006; Shearer et al., 2015). Mantle overturn is a large-scale process prompted by density instability (Elkins-Tanton et al, 2003). Early cumulates formed from a crystallizing melt are Mg-rich and incompatible-poor. Primitive is a term used to describe these early cumulates and indicates their Mg-rich and incompatible-poor chemistry (Best, 1982). As the melt continues to cool, Fe- and incompatible-rich cumulates crystallize. These late forming cumulates are termed evolved (Best, 1982). Iron-rich cumulates, however, are denser than Mg-rich cumulates; but since Fe-rich cumulates are formed later in the crystallization sequence, they settle out of the liquid (sink) and rest above Mg-rich cumulates. This density instability is rectified by the sinking of Fe-rich cumulates and the rising of Mg-rich cumulates (e.g. Elkins-Tanton et al., 2002, 2011; Shearer et al., 2015). This upwelling, primitive (Mg-rich) material may have experienced decompression melting during its ascent and subsequently

intruded the feldspathic crust as plutons (Shearer et al., 2015; Elardo et al., 2017). Mantle overturn may have transported primitive, deep material to the crust, that subsequently melted and assimilated KREEP material and cooled as intrusive plutons (Shearer et al., 2015; Elardo et al., 2017). Such intrusive volcanism produced igneous rocks such as the Mg-suite and alkali-suite.

Both suites were sampled by Apollo missions and were named for their enrichment in either Mg or alkalis (Warner et al., 1976; Shearer and Papike, 1999; Shearer et al., 2015). The alkali-suite is composed of alkali-rich (An < 90), Mg-intermediate to poor (Mg# < 65) anorthosites, gabbros, monzodiorites, quartz monzodiorites, and some silica-rich rocks (e.g. Shearer and Papike, 1999). The Mg-suite (Mg# ~65-93) approximates a fractional crystallization sequence from troctolites to norites to gabbros and displays cumulate or coarse granulitic textures, which suggest plutonic formation (Warner et al., 1976; Warren, 1985; Shearer and Papike, 1999). The chemistry of the Mg-suite, however, suggests a more complicated petrogenetic history. The Mg-suite has primitive (i.e., consistent with early crystallization) major element chemistry (Mg# ~65-93) but evolved (i.e., consistent with late crystallization) minor element chemistry (KREEP-rich); the occurrence of these two elemental patterns in one rock are in direct contrast (e.g. Shearer and Papike, 1999; Korotev, 2005). Decompression melting of primitive upwelling material, due to mantle overturn, may be the source of the Mg-enrichment of the Mg-suite (Shearer et al., 2006). The hot, upwelling magma may have assimilated KREEP, which may be the source of the evolved chemistry of the Mg-suite (Shearer et al., 2006; Elardo, 2017). Extensive fractionation of the plutons formed from upwelled, primitive material may have produced the alkali suite as well. A petrogenetic link between the alkali suite and Mg-suite has been suggested, due to their concentration of KREEP and Nd isotope systematics (Shearer et al.,

2006). The two lithologies may approximate a crystallization sequence of a KREEP basalt parent magma (Warren and Wasson, 1980; Snyder et al., 1995; Shervais and McGee, 1999).

Extrusive magmatism on the Moon produced material such as mare basalts and pyroclastics (e.g. Lucey et al., 2006 and references therein). Pyroclastic deposits, in the form of glass beads, are found in lunar regolith material sampled by both Apollo and lunar meteorites (Lucey et al., 2006). Pressure build-up of ascending magmas, due to the presence of volatile elements such as C, S, or H, results in explosive magmatism (Nicholis and Rutherford, 2005; Scaillet, 2015; Wetzel et al., 2015; Li et al., 2017). These fire fountains are one mechanism responsible for glass spherules found throughout the lunar soil (e.g. Ridley et al., 1973; Heiken et al., 1974; Delano, 1979, 1986; Elkins-Tanton et al., 2003).

However, glass spherules can also be formed through impact processes, as seen in terrestrial basins (Melosh and Vickery, 1991). Impacts can vaporize, melt, and eject material from the target rock as melt droplets (Melosh, 1990). Impacts are one of the most important metamorphic process on the Moon (Hiesinger and Head, 2006) because they mix, churn, and garden the surface, producing the extensive lunar regolith and soil observed today. The uppermost lunar crust is composed of surface regolith (Figure 1), which is about 10 m thick (Hiesinger and Head, 2006 and references therein). Broken and fractured ejecta and crustal rocks exist beneath the surface regolith to a depth of about 25 km (French et al., 1991). The full column of impact-affected rocks is known as megaregolith (Figure 1) (Hiesinger and Head, 2006).

The impacts responsible for producing the lunar regolith can also metamorphose the target rocks by heating (thermal metamorphism) or shocking them (shock metamorphism) and create mixtures of glasses, melts, and lithic material (e.g. Lucey et al., 2006). These impact-

related products may get transported long distances and subsequently mix with non-adjacent lithologies (Haskin, 2000). Large basin forming impacts (diameter > 20km) were more common on the early Moon than recent history (Wilhelms et al., 1987; Stöffler et al., 2006). These impacts were responsible for early, large-scale breaking and churning of the surface (Hiesinger and Head, 2006). More recent impactors, < 3 Ga, are smaller (diameter << 20 km) and churn only the uppermost layer, known as "gardening", and produce the fine-grained surface regolith (Wilhelms et al., 1987; Stöffler and Ryder, 2001; Hiesinger and Head, 2006; Stöffler et al., 2006). Surface gardening produces brecciated material that may contain a wealth of lithologies not adjacent to the underlying parent bedrock. Therefore, lunar feldspathic breccias may contain a large amount of information about the lunar crust in a single breccia, including impact-related material. One such impact-related material are granulites.

Granulites are metamorphic rocks found in both Apollo samples and meteorites that contain mostly plagioclase (~>50%) with variable amounts of olivine and pyroxene and other phases, such as ilmenite, chromite, and Fe-Ni metal (e.g. Lindstrom and Lindstrom, 1986; Treiman et al., 2010). They are formed by impact events that mix and warm the target rock. Over time, the rock cools and produces rocks with granulitic textures, such as rounded mineral grains and 120° mineral grain junctions, due to prolonged annealing (Cushing et al., 1999). Equilibration temperatures of granulites range from 1000-1150 C (Cushing et al., 1999; Hudgins et al., 2008). These temperatures suggest two formation mechanisms: shallow (20 to 200 m) burial in or around impact craters 30 to 90 km in diameter (Cushing et al., 1999) or contact to superheated impact melts and ejecta associated with large (basin) impacts (Hudgins et al., 2008). The protolith of Mg-rich granulites is an enigmatic rock type because, based on their chemistry,

they cannot be a simple mixture of known, pristine lunar rock types (Lindstrom and Lindstrom, 1986; Korotev and Jolliff, 2001; Korotev et al., 2003).

Unlike Mg-suite, magnesian granulites are REE-poor (An ~93-98), but they are also too Mg-rich (Mg# ~65-75) to be similar to FAN (Lindstrom and Lindstrom, 1986; Treiman et al., 2010). Yet granulites with similar Mg# are common in feldspathic meteorites, which suggests that magnesian granulites are a widespread rock type (Treiman et al., 2010; Gross et al., 2014a). The magnesian anorthosite (MAN) crustal lithology (An ~95-97; Mg# ~70-77) has been suggested as the magnesian granulite protolith (Takeda et al., 2006; Treiman et al., 2010; Gross et al., 2014a). MAN has been identified as a unique crustal lithology due to its potentially pristine (Takeda et al., 2006) nature and minor element chemistry dissimilarities with Mg-suite and FAN. The plagioclase studied in MAN in lunar meteorite Dhofar 489 is twinned. Takeda et al. (2006) argue that that is an indication of pristinity because if the rock was metamorphosed, that texture would have been overwritten. Since twinning is still observable, MAN may be a common crustal rock type. Gross et al. (2014a) suggested that MAN formation was hard to explain in the current, simple lunar magma ocean paradigm because a LMO magma that crystallizes high Mg# mafic phases would not be dense enough to allow plagioclase to float to the surface. Serial magmatism was suggested as an alternative (Gross et al., 2014a; Longhi and Ashwal, 1985; Longhi, 2003) that could explain MAN formation. Recent models of LMO progression, however, suggest that MAN (Mg# > 70) may be produced when the first liquidus plagioclase forms (Charlier et al., 2018) and thus, could be widespread. This is consistent with findings from Takeda et al. (2006) who argued that MAN may be the deep anorthositic layer observed in crater peak rings by remote sensing.

Identification of crustal lithologies, such as purest anorthosite (~98 volume% plagioclase) (Ohtake et al., 2009), and formations, such as silicic domes (Glotch et al., 2010), have been greatly facilitated by remote sensing observations. Similarly, the chemistry of the surface has been mapped by orbiters such as Clementine and Lunar Prospector, which led to a re-evaluation of crustal terminology (Jolliff et al., 2000). The lunar magma ocean model, crafted in the wake of Apollo sampling, suggests that KREEP is a global layer. Therefore, surface concentration of Th should be uniform. However, Th is almost exclusively concentrated in the Procellarum Basin, a large impact crater on the nearside (Jolliff et al., 2000). Consequently, Jolliff et al. (2000) named three terranes that describe the chemical, petrologic, and geophysical differences in the crust: the basaltic Procellarum KREEP terrane (PKT), the thick farside feldspathic highlands terrane (FHT), and the South Pole-Aitken basin terrane (SPAT). The PKT blankets a large portion of the equatorial nearside and is coincidentally where the Apollo missions landed (Jolliff et al., 2000). Thus, while Apollo samples provide an incredible amount of information, they are not representative of the average lunar crust. Therefore, to obtain a better understanding of the origin, formation, and evolution of the Moon other samples from areas distal from the returned sample suite need to be investigated (e.g. Palme et al., 1991; Warren 1994; Korotev et al., 2003; Korotev, 2005; Warren et al., 2005; Joy et al., 2010; Gross et al., 2014a).

Data from the Lunar Prospector and Clementine spacecraft show that, relative to the Apollo and Luna landing sites, most of the lunar surface has low abundances of FeO and incompatible elements (Jolliff et al., 2000; Gillis et al., 2004), with an average composition more like that of the feldspathic lunar meteorites (Korotev, 2003). In addition, lunar meteorites in general come from random places on the Moon, including areas not visited by the Apollo and Luna missions and are therefore, more representative, of the whole lunar crust and

represent an excellent target for investigation to better understand the lunar crustal evolution (Korotev et al., 2003; Korotev, 2005; Day et al., 2006; Joy and Arai, 2013; Gross et al., 2014a). Lithologies and rock fragments that are similar in Mg# to Apollo Mg-suite rocks are present in most lunar feldspathic meteorites (e.g. Gross et al., 2014a). However, most lack the KREEP component which is characteristic to Apollo Mg-suite rocks, which suggests that KREEP may not be globally distributed (Jolliff et al., 2000; Korotev, 2005; Gross et al., 2014a). Additionally, lunar meteorites are known to contain rock types that are rare or not represented in the Apollo collection, such as: magnesian anorthosite e.g., in Dhofar (Dho) 489; Dar al Gani (DaG) 400, Dho 025, Dho 304, Dho 305, Dho 489, NWA 482, NWA 2996, NWA 6888, Yamato (Y) 791197, Y 82193, Y 86032 (Takeda et al., 2006; Gross et al., 2014a); spinel-rich troctolites and Mg-spinel-rich lithologies in Dho 489 and Allan Hills A (ALHA) 81005 (Gross and Treiman, 2011; Takeda et al., 2006); very high-K KREEP lithology (Lin et al., 2012); pure anorthosites (Nagaoka et al., 2014); and clasts that are either magmatically unique or non-lunar (Joy et al., 2014; Gross, 2014). Therefore, lunar meteoritic samples provide a unique opportunity to investigate lithologies and rock types that may not be represented in the Apollo sample collection and are crucial to help improve our understanding of unsampled areas of the Moon, enlarge our knowledge of lunar highland rock types, and understand of the global formation of the Moon, including its magmatic and crustal evolution and its early history (e.g., Korotev et al., 2003; Korotev, 2005; Day et al., 2006; Gross and Treiman, 2011;Joy and Arai, 2013; Gross et al., 2014a,b).

For this study, we have obtained two new lunar feldspathic breccia meteorites, Northwest Africa (NWA) 10291 and 11182. We present a complete survey of lithologies in each meteorite and petrographically and geochemically describe and characterize selected clast lithologies to

constrain their formation history. We then place these small-scale observations into the large-scale petrogenetic schemes of lunar evolution (i.e. lunar magma ocean and crustal formation) by comparing their geochemical relationship to other known lunar rock types (Apollo and meteoritic). Finally, we constrain the petrogenetic origin and evolution of lithologies present in unsampled areas of the Moon.

METHOD

Qualitative elemental X-ray mapping

NWA 10291 and 11182 were mounted in epoxy and polished, creating one thick section of each rock. Images of the samples in plane polarized light and crossed polarized light were obtained using a petrographic microscope. Qualitative composite maps were created from those images using GIMP©, an image processing program. Additionally, elemental X-ray, cathodoluminescence, and back-scattered electron (BSE) maps (Figure 2-3) were obtained using the Electronprobe Microanalyzer (EPMA) on the JEOL JXA-8200 Superprobe in the Department of Earth and Planetary Sciences at Rutgers University. Conditions for mapping were: 15 keV acceleration voltage, 25 nA beam current, and 3 μm beam diameter. The following elements were mapped: Al, Ca, Cr, Fe, Mg, Ni, K, Si, Na, S, and Ti. Reflected light (Figure S71, S148), elemental X-ray (Figures S44-54; Figures S122-132) and cathodoluminescence maps (Figure S55, S147) can be found in the supplemental material. The samples were segmented into nine images, each with a resolution of 1024x1024, pixel step size of 3 μm, and dwell time of 20 ms. Element maps were combined into the following Red-Green-Blue (RGB) mosaics for cursory mineral identification: Al-Si-Mg, Ca-Si-Al, Ca-Si-Fe, Ca-Si-Mg, Cr-Fe-Mg, Cr-Si-Fe, K-Si-Mg, Na-Si-Al, Na-Si-Fe, Na-Si-Mg, S-Si-Fe, S-Si-Mg, and Ti-Fe-Mg (Figures S56-S71; Figures S133-S146). Combined BSE, X-ray element mosaics, as well as RGB maps were used to identify minerals and clasts of interest for further quantitative analyses.

Quantitative point analyses

Quantitative point analyses for major and minor elements were obtained via EPMA on the JEOL-8200 superprobe with conditions listed in Table 1 (Figures S1, S72 for analysis points). For plagioclase and glass analyses, the beam current was lowered to 20 nA and the beam

diameter increased to 3 μm to minimize loss of volatile elements (Na, K in plagioclase; Na, K, and Si in glass) in those phases. Count times were adjusted for volatile elements to 10 seconds since high count times on volatiles elements may lead to volatile loss and incorrect measurements. The following elements were measured, listed with detection limits in oxide wt%. For olivine and pyroxene: Na (0.02), Mg (0.01), Fe (0.07), Si (0.02), Al, (0.02), Ca (0.01), Mn (0.01), Ti (0.01), Ni (0.02), Cr (0.05), Co (0.02); for plagioclase, glass, and silica: K (0.01), Na (0.02), Ca (0.01), Al (0.01), Si (0.02), Fe (0.06), Mg (0.01), Mn (0.01), Ti (0.01), Cr (0.05); for metal and sulfides (detection limits given in element wt% (el.wt%): Fe (0.06), Ni (0.08), Mg (0.01), Mn (0.02), Cr (0.04), S (0.01), Si (0.01), Ti (0.01), Co (0.02) P (0.01). The Mean-Atomic-Number method was used for background calculations. Cobalt data was corrected for the Co-kα and Fe-kβ peak overlap. Peak overlap also exists between Mn and Cr. Due to low concentrations of both elements in the analyzed mineral phases in this study a correction was not necessary. Natural and synthetic secondary standards were used to test standardization and to ensure data quality. Analyzed clasts and minerals were chosen by size and/or chemistry, as determined in preliminary X-ray mapping. The clasts needed to be large enough and uniform enough for at least two points (~10 μm) to be measured without overlap. Secondary to size, chemistry was considered when choosing clasts. Some small (<40 μm) clasts were investigated because of their elevated concentration of K or P (potential KREEP signature), Na (alkali-rich), or Fe-Ni (metal) relative to the rest of the sample.

Statistical Analyses

The mineral chemistry of pyroxene in granulites in NWA 11182 required a quantitative method to understand the chemical distribution of the granulite clasts and identify whether a bimodal distribution of the data exists (see Results-NWA 11182-Impact-related clasts). Data may

form histograms in several shapes, including unimodal, bimodal, and multimodal (Devore, 2015). Unimodal histograms contain a single peak (mean), bimodal histograms contain two peaks, and multimodal histograms contain more than two peaks (e.g. Devore, 2015). A unimodal histogram can, generally, be approximated by the normal distribution (Devore, 2015). The normal distribution is a bell-shaped curve that has a single mean and variance greater than zero (Devore, 2015).

The Lilliefors test was run on the Mg# of pyroxenes in granulites in NWA 11182 using MATLAB to determine if the granulites sampled came from a normally distributed population (Lilliefors, 1967). In this analysis, alpha (significance level) was set at 0.05, per standard MATLAB input, as well as 0.01 to further investigate normality. Low values of alpha were chosen to minimize type I (rejecting the null when it is true) and type II (not rejected the null when it is false) errors (e.g. Devore, 2015). This test assumes a null hypothesis, which means the pyroxene chemistry of granulites in NWA 11182 are not significantly different than a normally distributed population. The output of the test is either 1 or zero, where 1 signifies that the test rejects the null. A similar normality test, the Kolmogorov-Smirnov test, was considered; however, the Kolmogorov-Smirnov test requires a specified normal distribution input, whereas the Lilliefors test does not (Lilliefors, 1967). Utilization of the student t-test was also considered; however, the student t-test is best applied to normal distributions and it was unknown if the pyroxene chemistry distribution is normal. Therefore, the Lilliefors test allows for a more general investigation into the potential normality of a dataset.

SAMPLE

Table 2 contains the clast nomenclature and the definition of each clast type that is used throughout this study. Detailed clast definitions are given in the "Results" section below.

NWA 10291

NWA 10291 is a feldspathic polymict regolith breccia found in Morocco in 2015 and is paired with the following meteorites: NWA 7834, NWA 7848, NWA 8306, NWA 10149, NWA 10172, NWA 10203, NWA 10272, NWA 10253, NWA 10258, NWA 10263, NWA 10317, NWA 10376, 10546, NWA 10599, NWA 10644, NWA 10782, NWA 10810, NWA 10989, NWA 11109, NWA 11185, NWA 11249, NWA 11563, and Galb Inal (Bouvier et al., 2017). This clan of meteorites all represents a group of mafic lunar meteorites with similar Sm and Sc chemistry (Korotev and Irving, 2014; Korotev and Irving, 2015; Korotev and Irving, 2016; Korotev and Irving, 2017). The sample has no fusion crust (Bouvier et al., 2017). The rock contains lithic clasts, impact-related clasts, and mineral fragments (Table 3). Lithic clasts in NWA 10291 include mafic, evolved, and symplectite clasts (Figure 4) and range chemically from Mg-suite to ferroan anorthosites (FAN) to alkali suite. Impact melt breccias and recrystallized impact melt clasts are the most common form of impact-related clasts in NWA 10291, but the rock also contains granulites and one glass bead (Figure 5). Mineral grain fragments of plagioclase, pyroxene, and olivine grains are abundant throughout the rock, as well as smaller fragments of Fe-Ni metal, a silica-phase, ilmenite, sulfides, and zircon. Vesicles are abundant in the matrix and occur in lithic and impact-related clasts as well.

NWA 11182

NWA 11182 is a feldspathic polymict regolith breccia, found in 2017 in an unspecified location in northwest Africa (Gattacceca et al., 2019). Similar to NWA 10291, NWA 11182 does

not have a fusion crust (Gattacceca et al., 2019). The sample has experienced some degree of terrestrial weathering, indicated by the presence of Ba-S-rich material in cracks (Figure S154-157). It contains lithic clasts, impact-related clasts, and mineral fragments (Table 3). The lithic clasts in NWA 11182 are all mafic (Figure 6). The meteorite is dominated by granulites and recrystallized impact melt, with a few impact melt breccias (Figure 7). Mineral grain fragments of plagioclase, pyroxene, olivine, and Fe-Ni metal are present throughout the sample (Figure 8).

RESULTS

Clast definitions

Clasts within both meteorites were classified into two groups based on their chemistry and texture (Table 2): 1) Lithic clasts that formed on the Moon in the absence of impacts and 2) impact-related clasts. Lithic clasts come from rock types that are either products of magmatic differentiation or subsolidus re-equilibration (e.g. Shearer et al., 2006; Fagan, 2007; Seddio et al., 2013). They are further subdivided into mafic, evolved, and symplectitic clasts (Table 2). Symplectites are formed from the breakdown of unstable phases during prolonged annealing (Fagan, 2007). The breakdown of hedenbergite (Fe-Ca-rich pyroxene) produces a fine-scaled, interwoven pattern of pyroxene and olivine, along with a complimentary silica-phase, that has been observed in lunar rocks (e.g. Fagan, 2007). Impact-related clasts were formed post-impact in or near an impact crater and or impact-ejecta blanket (e.g. Lucey et al., 2006) and are further divided into impact breccia, recrystallized impact melts, and granulites (Table 2). Glass beads were excluded from this definition because they may form either during impact events (an impactor melting lunar surface material) or represent pyroclastic eruption products (volcanic origin) (e.g. Arndt et al., 1984; Melosh and Vickery, 1991; Zeng et al., 2018). Mineral grains are defined in this study as grains that contain more than 95% of a single mineral. Images of all clasts can be found in the Supplemental Material (Figures S2-43; Figures S72-121).

NWA 10291

Petrography and mineral chemistry

Sixty-six clasts were analyzed in NWA 10291; they include mineral grains, lithic clasts, and impact-related clasts; the analyzed clasts span 25% of the sample's surface. The clasts studied have been reported in meteorites paired with NWA 10291, so they are likely

representative of the rock. However, the rock may contain other unique clasts deeper within the rock not visible from the current face. Additionally, it has been noted that larger grains are more likely to be measured in a rock due to a greater chance of intersecting the surface of a thin or thick section (Sahu, 1977) and that coarser grained (~>0.4 mm) meteorites have a larger sampling bias than fine-grained meteorites (Beck et al., 2013). Therefore, a sampling bias probably exists for clast data from NWA 10291 and the chemistries and modes presented may not accurately represent the full population or chemistries in NWA 10291.

Lithic clasts in NWA 10291 are represented by a variety of mafic, evolved, and symplectite clasts (Table 3) set in a matrix of glass and individual mineral grains varying in size from < 20 μm to 600 μm. Cracks and holes are abundant in the meteorite (Figure 2). Some are filled with terrestrial weathering products. The mafic clasts include the following rock types: anorthosite, anorthositic gabbro, anorthositic norite, norite, noritic anorthosite, olivine gabbro, olivine norite, peridotite, pyroxenite, and troctolitic anorthosite (Figure 4). These lithic clasts range in size from ~100 up to 1050 μm. Most impact-related clasts in NWA 10291 are impact melt breccias and recrystallized impact melts (Figure 5). They range in size from as small as 300 μm up to ~3 mm. They are mostly composed of recrystallized or glassy anorthitic plagioclase (An ~97) with skeletal crystals of pyroxene and sometimes olivine; or polymict impact breccias. In addition, one glass bead was identified and analyzed; it is ~340 μm wide and contains two vesicles that range in size from 90 to 100 μm.

Below are petrographic and mineralogic descriptions of all clasts studied based on the nomenclature described in Table 2 and the clast inventory reported in Table 3.

Lithic clasts

One anorthosite clast was identified in NWA 10291. It is 680 μm in length. The plagioclase is anorthitic (An 96) (Figure 10) and contains a pyroxene inclusion that is Fe-rich (En 26, Fs 52, Wo 22) (Table 4, Figure 9). The plagioclase is heavily cracked and contains some needle-like Fe-rich material that too small for analysis (< 3 μm). At the clast rims, plagioclase appears to be glassy, evident in the smoother texture and the absence of cracks, compared to the center of the clast. The only pyroxene inclusion is anhedral, 60 μm in size, and exhibits exsolution lamellae.

An anorthositic gabbro was measured (Table 4) that is 630 μm in length. The Ca-rich plagioclase (An 93) is heavily cracked and contains small (< 3 μm) inclusions of Fe-rich material that are too small for analysis (Figure 10). Pyroxene in the clast is subhedral, Fe-rich (En 18-28, Fs 43-47, Wo 29-34), exhibits thin (< 1 μm) exsolution lamellae and is fractured (Figure 11, Figure 4). Plagioclase partially encloses pyroxene in some areas, but most of the pyroxene is adjacent to the matrix.

Like most lithic clasts in NWA 10291, the 350 μm long anorthositic norite clast is heavily fractured. Some igneous texture has been preserved and is evident in the euhedral to subhedral plagioclase laths (30-60 μm long) that are surrounded by subhedral pyroxene and olivine grains that range in size from 20 to 120 μm and 40 to 80 μm, respectively (Figure 4). The plagioclase in the center of the clast is more calcic (An 97) compared to plagioclase found near the rim (An 91) (Table 4; Figure 10). The pyroxene and olivine grains range in Mg# from hyperferroan to Mg-rich (En 44-58, Fs 16-25, Wo 17-40 and Mg# 62-64, respectively) (Figure 9). Small (<3μm) inclusions of ilmenite grains occur at the edges of some pyroxene grains.

The norite in NWA 10291 is 770 μm long and contains plagioclase and pyroxene (Figure 10). The plagioclase is fractured, but its composition remains homogenous (An 97) (Table 4, Figure 10). The pyroxene is Ca-rich (En 45-61, Fs 12-26, Wo 13-43) and contains small (<2 μm) inclusions of ilmenite (Figure 4; Figure 11). Some plagioclase is poikiolitically enclosed by pyroxene. Both mineral phases are anhedral, but some igneous texture is preserved as small plagioclase laths (30 to 120 μm in size) in pyroxene.

The noritic anorthosite clast is one of the largest clasts in the sample at 1050 μm (Figure 4). The plagioclase is anhedral, heavily fractured, Ca-rich (An 94) and contains inclusions of Fe-rich pyroxene and ilmenite (Ti# 50) that are ~150 and 80 μm in size, respectively (Table 4, Figure 10). Pyroxene in the clast is subhedral, Fe-rich, and ranges in composition from En 9-26, Fs 50-73, Wo 18-36 (Figure 9). Additionally, an inclusion of Fe-S-sulfide (270 μm in size) is present in the plagioclase.

The olivine gabbro is also one of the largest clasts at 1050 μm (Figure 4). It contains subhedral plagioclase laths and anhedral, sometimes rounded, olivine grains set in pyroxene. Plagioclase composition ranges in composition from An 88-94 (Table 4; Figure 9). The less calcic plagioclase in general is smaller (40-210 μm in length) and more lath-like than the larger (720 μm), more calcic grain. Pyroxene composition also varies with location in the clast. The center of the clast contains less calcic, more magnesian pyroxene (En 61-64, Fs 30-31, Wo 6-9) compared to the rim (En 59-60, Fs 27-28, Wo 12-15). Olivine in the sample is forsteritic and homogenous in composition (Mg# 64) (Figure 9). Plagioclase and olivine in the clast are poikiolitically enclosed by pyroxene.

The olivine norite clast in NWA 10291 is ~550 μm in size, fractured, and comprised of mostly (70 %) olivine with a forsteritic composition of Mg# 63. Subhedral pyroxene (En 58-62,

Fs 27-30, Wo 9-15) and Ca-rich plagioclase (An 89-91) are adjacent to the large olivine grain (Table 4). Pyroxene with a composition of En 56, Fs 24, Wo 20 and small (20 μm) ilmenite grains can be found as inclusions in the olivine (Figure 4; Figure 9).

A small (210 μm in size) peridotite fragment was measured that is composed of olivine (80%) and pyroxene (20%). Pyroxene along the edge of the clast fragment is more magnesian and less calcic (En 59, Fs 28, Wo 13) than pyroxene near the center (En 48, Fs 17, Wo 35) (Table 4). Olivine is homogenous and forsteritic with Mg#64.

A pyroxenite clast was measured that is ~470 μm in length, ~300 μm in width, and is composed of a single pyroxene grain (94%) and a plagioclase grain (6%, 170 μm in size). The pyroxene displays thin (<1 μm) exsolution lamellae that are not straight but curved into flow-like patterns (Figure 4). The composition of the pyroxene varies but is generally Fe-rich (En 28-32, Fs 36-60, Wo 8-32) (Table 4; Figure 11). Plagioclase in the pyroxenite clast is subhedral and compositionally less calcic (An 92) than plagioclase measured in many other lithic clasts in this meteorite. A large crack runs through this rock fragment.

A small (330 μm in size) troctolitic anorthosite was measured near the edge of a large swath of melt. Plagioclase in the clast is calcic (An 97) and contains small inclusions of olivine (50 μm) (Table 4; Figure 10). The olivine (Mg# 61) is associated with an ilmenite phase too cracked for analysis. Much like the other lithic clasts in NWA 10291, phases in the troctolitic anorthosite are cracked (Figure 4; Figure 9). The plagioclase partially encloses the olivine and completely encloses the ilmenite. The edges of the clast show interaction with the nearby vesicular melt.

Four evolved clasts were identified in NWA 10291 (C1b, C7, C22, and C32 (Table 4). C1b is a small (~100 μm) clast that contains a silica-phase and mafic-rich pyroxene (En 52, Fs

44, Wo 4). C7 is comprised of mostly (95%) exsolved pyroxene (En 28-39, Fs 32-50, Wo 11-38) (Figure 9). Small (40-80 μm) plagioclase laths are observed as inclusions in the moderately sized clast (315 μm). The composition of the plagioclase is less calcic than the mafic clasts (An 89). C22 has K-rich plagioclase (An 1, Ab 13, Or 86) and Ca-rich pyroxene (En 12-15, Fs 46-49, Wo 17-40) (Figure 10). The ~240 μm long clast is enclosed by vesicular melt. The clast boundaries have been melted by the surrounding material, producing an anhedral pyroxene grain. C32 contains Na-rich plagioclase (An 51, Ab 47, Or 2), apatite, and ilmenite. It is a small (150 μm) clast near the edge of the sample.

Two symplectite clasts were measured in NWA 10291 (C19 and C21) and are composed of fine (< 1 μm) symplectitic intergrown of olivine, pyroxene, and potentially silica (Figure 4). Pyroxene compositions in both clasts are En 11, Fs 58, Wo 31 and En 5, Fs 59, Wo 36 (Table 4; Figure 9). Olivine in both samples is highly fayalitic with Mg# 6 and 3, respectively. Both symplectites contain small amounts of plagioclase, though of different compositions. C21 has an inclusion of Ca-rich plagioclase (An 97) (Figure 10) whereas C19, which has a much finer intergrowth of olivine and pyroxene, has Na-rich plagioclase (An 85) along the rim, as well as ilmenite.

Impact-related clasts

Recrystallized impact melt clasts have a slightly more varied composition than impact melt breccias. Plagioclase composition ranges from An ~90-99 (Figure 12). The clasts display quench textures of olivine (0-10%) and pyroxene (10-30%) crystals (<40 to ~100 μm in size) set in plagioclase (60-90%) (Figure 5).

One granulite was observed in NWA 10291. Olivine (8%) and pyroxene (6%) crystals are inclusions in a plagioclase groundmass (86%) (Figure 5). The inclusions are small (< 10 μm) and

granular (rounded) (Figures 17, 18). The plagioclase is mostly calcic (An 92) and the mafic minerals are moderately Fe-enriched (En 44-50, Fs 18-35, Wo 15-39 and Mg# 60-61). Plagioclase is cracked on one side of the clast.

One glass bead was found in NWA 10291. It is 350 μm in diameter and contains two large (100 μm wide) vesicles (Table 4; S4). The composition in oxide wt% is: SiO_2=45.57 ± 0.10, TiO_2=0.52 ± 0.04, Al_2O_3=9.04 ± 0.04, Cr_2O_3=0.50 ± 0.07, FeO=19.51 ± 0.37, MnO=0.31 ± 0.06, MgO=14.44 ± 0.64, and CaO=9.50 ± 0.45.

Mineral grains

Pyroxene mineral grains are abundant throughout the sample. They vary in size from ~100 to 600 μm and composition from En 17-79, Fs 13-67, Wo 3-42. Most display exsolution lamellae; few are homogenous. One small (~20 μm) olivine grain was found near a melted plagioclase grain (An 90) and a silica-phase (wt% SiO_2=98.37). Its chemistry is more fayalitic with Mg# 66 than most olivine found in mafic clasts (Figure 13). Few plagioclase mineral grains were measured. They range in size from ~100 to 300 μm and vary compositionally from An 63 to 93. Most grains have compositions around An ~95, though one grain is much more sodic with An ~63.

Metal grains were observed in NWA 10291. Most were found as single grains in the matrix. One was found next to a silica-phase and another is in an impact melt breccia. Metallic composition (in el.wt%) varies from 2-53 Ni, 1-2 Co and 46-98 Fe (Figure 26). Fe-S-sulfide phases are in the matrix as well as near clasts, sometimes associated with Fe-Ni metal. One zircon was found near the edge of the sample but not measured. Small ilmenite grains are found in the matrix and range in composition from Ti# 52-93. There are abundant silica-rich mineral grains in NWA 10291. They are generally small (~100 μm) and some are associated with nearby

Ca-carbonate. Their composition is nearly 100 wt% silica but contains up to (in oxide wt%) 0.16 Na2O, 1.72 MgO, 1.20 Al2O3, 0.45 K2O, 0.32 CaO, 0.22 TiO2, 0.06 Cr2O3, and/or 0.18 FeO.

NWA 11182

Petrography and mineral chemistry

Seventy clasts were analyzed in NWA 11182; together, they comprise about 44% of the surface. The restricted chemistry of these clasts suggests that they may be representative of the rock (Figures 15-20). As for NWA 10291, a sampling bias may exist in the selection of clasts from NWA 11182. Therefore, the chemistries and rock-types presented may not represent the full population of rocks or breadth of chemistries present in NWA 11182.

Of the measured clasts, several represent mafic clasts that include: anorthosite, norite, noritic anorthosite, peridotite, and troctolite (Table 3). However, most of the measured clasts (>50%) are impact-related clasts. Most of these impact-related clasts are granulites. Impact melt breccias display are the largest clasts, ranging from 540 μm up to 1.6 mm. The pyroxene crystals in impact melt breccias are anhedral and skeletal Granulites are slightly smaller in size, ranging from 350 μm to 1.5 mm. Recrystallized impact melt clasts are generally even smaller, ranging in size from 70 to 540 μm. Several clasts, as well as the matrix, display cracks, fractures, or holes that can be filled with barite (Figure 3: Full Back Scattered Electron (BSE) image of NWA 11182.).

Lithic clasts

Anorthosite clasts are common in NWA 11182. Plagioclase composition ranges from An 90-98 (Table 5; Figure 16). Both Ca-rich (En 37-48, Fs 10-31, Wo 29-45) and Ca-poor pyroxene rich (En 57-65, Fs 26-36, Wo 5-10) populations are present and are magnesian. Clast sizes range from 140 μm up to 1540 μm. Some anorthosite clasts have small (<10 μm), rounded olivine

inclusions, in addition to pyroxene (170 μm). In some anorthosite clasts, plagioclase is cracked or has a hole (Figure 6). One clast has several large cracks filled with barite that run the length of the clast (300 μm long). All phases are anhedral to subhedral.

Norite clasts are also common in NWA 11182. Ca-rich and Ca-poor pyroxene (En 46-78, Fs 10-32, Wo 3-42) are present in all norite clasts. Plagioclase composition is uniform (An 96) (Table 5; Figure 16). These clasts are highly fractured and range in size from 80 to 300 μm. In some clasts, plagioclase (<50 μm) encloses pyroxene (30-40 μm). In others, pyroxene (120 μm) encloses plagioclase (30 μm). Crystals are anhedral.

Two noritic anorthosite clasts were measured. Plagioclase composition is homogenous among both clasts (An 96) (Table 5; Figure 16). Magnesian Ca-rich and Ca-poor pyroxene exists in both clasts (En 42-60, Fs 18-30, Wo 10-40). One has an inclusion too small (<5 μm) for EPMA analysis, however composition measured using EDS indicates that it is likely an olivine. Both clasts are heavily fractured in both the plagioclase and pyroxene. Pyroxene in one of the noritic anorthosites is rounded (300 μm) and its corresponding plagioclase (1200 μm) is anhedral and has many holes and cracks. Other noritic anorthosites have anhedral crystals, with some pyroxene nearing subhedral boundaries.

A small (290 μm) peridotite clast was measured in the matrix. Most pyroxene is Ca-poor (En 64-78, Fs 22-24, Wo 3-11) but there is a large inclusion of Ca-rich pyroxene (70 μm in size), along with small (<10 μm up to 30 μm), lath-like Ca-rich pyroxene crystals (En 45-48, Fs 11-13, Wo 39-43). The plagioclase inclusion in the pyroxene is calcic (An 96) (Table 5). Large fractures penetrate all phases and run the length of the clast. The olivine is large (180 μm), magnesian (Mg# 64), and heavily altered with cracks and pits throughout. Plagioclase and pyroxene are anhedral, while the corresponding olivine is subhedral.

One, small, fractured troctolite clast was measured in the matrix. Plagioclase is calcic (An 96) and pyroxene is magnesian (En 64, Fs 26, Wo 10) (Figure 15, Figure 16). The clast is 120 μm in length. Small (<5 μm), rounded plagioclase crystals are enclosed in pyroxene, while the larger plagioclase groundmass encloses skeletal pyroxene (40 μm in length).

Impact-related clasts

Impact melt breccias exhibit quench textures of small (<10 μm) pyroxene crystals set in a plagioclase groundmass. Plagioclase composition is calcic (An ~95) and pyroxene is magnesian (En 44-76, Fs 15-25, Wo 4-39) (Figure 17, Figure 18). Small (<20 μm) inclusions of forsteritic olivine are present in the plagioclase, with Mg# 71, and are generally associated with pyroxene (Figure 7).

Clasts of recrystallized impact melt are abundant throughout the rock. Plagioclase composition ranges from An 93-97. Pyroxene compositions are magnesian and range in Ca-content (En 25-76, Fs 10-45, Wo 4-45). The pyroxene crystals are anhedral and skeletal. Some clasts contain small inclusions of olivine that range in Mg# from 57 to 71. Two recrystallized impact melt clasts contain small (<10 μm) inclusions of Fe-Ni metal too small for analysis.

More than 50% of the analyzed impact-related clasts in NWA 11181 are granulite clasts. The plagioclase groundmass is calcic ranging from An 90 to 98 and contains inclusions of pyroxene and olivine. Pyroxene compositions vary in Mg# from hyperferroan (Mg# 38) to highly magnesian (Mg# 84) and Ca-poor to Ca-rich (En 28-76, Fs 10-47, Wo 3-46). Granulated olivine is generally associated granulated pyroxene and range in Mg# ranging from 41 to 74. Many olivine crystals are fractured and display alteration textures. Some granulite clasts contain chromite inclusions with a composition of Mg# 13-16, Cr# 66-94, and Ti#= 6-34. One granulite

clast contains a small inclusion of Fe-Ni metal with el.wt% of Fe= 91.09 ± 0.33, Ni= 8.74 ± 0.02, Co= 0.62 ± 0.02, P= 0.16 ± 0.01, and Ca=0.11 ± 0.01.

The granulites in NWA 11182 appear to form two populations (a bimodal distribution; Figure 25b) when the Mg# of pyroxene is considered: a high-Mg population and a low-Mg population. Data may form histograms in several shapes, including unimodal, bimodal, and multimodal (Devore, 2015). Unimodal histograms contain a single peak (mean), bimodal histograms contain two peaks, and multimodal histograms contain more than two peaks (e.g. Devore, 2015). A unimodal histogram can, generally, be approximated by the normal distribution (Devore, 2015). The normal distribution is a bell-shaped curve that has a single mean and variance greater than zero (Devore, 2015). To understand if the granulites in NWA 11182 truly have a chemical difference, the Lilliefors test was run on the entire population of Mg# of pyroxenes in granulites in NWA 11182. The test rejects the null hypothesis at both the 95 and 99% significance levels. Therefore, the granulites in NWA 11182 are significantly different from a normally distributed population. This indicates that the distribution of pyroxenes in granulites in NWA 11182 has more than one peak, which suggests that the two groups (Mg-rich and Fe-rich) of granulites observed in their histogram are distinct.

Mineral grains

Pyroxene mineral grains are abundant in the sample. They range from <20 μm to 420 μm in size. Compositions are varied from Ca-poor (Wo 4) to Ca-rich (Wo 47) and Mg-rich (En 76) and Mg-poor (En 18) (Fs 7-50). Mineral grains of olivine range from 50 to 380 μm in size and are found throughout the meteorite. Some, like olivine in granulite clasts, are cracked and altered (Figure 8). Others are cracked but retain homogeneity. Compositionally the olivine grains range from fayalitic (Mg# 48) to forsteritic (Mg# 82). Plagioclase mineral grains are the most common

mineral phase in NWA 11182 (An 59-97). They are all heavily cracked and some are intruded by veins of barite, as well as Ca-carbonate. One small (<10 μm) Fe-Ni metal grain was measured in the matrix.

DISCUSSION

Verification of lunar origin

The ratio of Fe/Mn in olivine and pyroxene is widely used as a "planetary fingerprint" to identify the planetary origin of extraterrestrial materials (e.g., Papike et al., 1998; Karner et al., 2003, 2006; Berlin et al., 2011). Iron and Mn do not fractionate appreciably during normal igneous processes (Papike et al., 1998) but are very sensitive to redox conditions and volatility (e.g., Miyamoto et al. 1993; Goodrich and Delaney 2000; Papike et al.2003). Therefore, any observed differences in the ratio are indicative of the parental melt conditions such as starting composition and oxygen fugacity (Papike et al., 1998; Karner et al., 2003; Berlin et al., 2011). The average lunar Fe/Mn ratio for pyroxene and olivine is 75 and 65, respectively, but can range from 25-120 and 45-145 (Papike et al., 1998; Fagan et al., 2002; Anand et al., 2003; Karner et al., 2003, 2006; Zeigler et al., 2005; Joy et al., 2008, 2014).

Both olivine and pyroxene in NWA 10291 and NWA 11182 are mostly consistent with lunar origin (Table 6, Table 7), ranging from 60-131 for olivine and 25-160 for pyroxene. Most clasts are centered along the lunar Fe/Mn trend line and no trends due to lithologic type are observed (Figure 21). Pyroxene in both meteorites, at low Fe, plots above the expected lunar trendline, but is still consistent with Fe/Mn ratios reported for other lunar meteorites (Figure 21a,b; e.g. Fagan et al., 2002; Anand et al., 2003; Zeigler et al., 2005; Joy et al., 2008).

The olivine in NWA 10291 plots in two populations, an Fe-rich and Fe-poor group (Figure 21c). The Fe-rich population consists of the symplectites and a fayalitic mineral grain. The mineral grain is likely not from a broken symplectite clast because it is much larger than any olivine seen in other symplectites in NWA 10291. All other olivine-bearing clasts belong to the Fe-poor population. Olivine in NWA 11182 are all comparatively Fe-poor (Figure 21d). Though

the Fe-poor olivine population in NWA 10291 and the olivine in NWA 11182 appears scattered and plot below the lunar trendline, most data points agree with the chemistry of other lunar meteorites (e.g. Fagan et al., 2002; Anand et al., 2003; Zeigler et al., 2005; Joy et al., 2008).

One possible explanation for the clasts with Fe/Mn ratios different than expected lunar values is that these clasts may have experienced different crystallization histories. For example, oxygen fugacity may change locally to more reducing or oxidizing conditions due to impacts or the presence of water, which may change the amount of available Fe^{2+}, Fe^{3+}, and Fe^{0} in the melt that then would be incorporated into silicate phases such as olivine and pyroxene (McCanta et al., 2004). Additionally, impacts can redistribute Fe and Mn in impact melt (Ganino et al., 2018). Such redistribution may occur due to unmixing of the melt via silicate liquid immiscibility (Rowan and Ahrens, 1994; Hamann et al., 2017), or through unrepresentative sampling of the impact melt sheet due to inhomogeneous mixing of target and impactor material (Ganino et al., 2018). However, another way to explain the different Fe/Mn ratios of these clasts is that the analytical count rates for Fe and Mn were not very long to achieve high precision and thus the data is more scattered. Taken the analytical error into account, the higher and lower Fe/Mn ratios of both olivine and pyroxene fall within the range expected for the Moon.

Evidence of terrestrial weathering

Both meteorites contain evidence of terrestrial weathering and both meteorites are fractured. NWA 10291 appears to be more heavily fractured than NWA 11182. These fractures and cracks may have formed during brecciation on the Moon through impact events, ejection from the lunar surface, or landing on Earth by traveling through the terrestrial atmosphere (Flynn, 2004). Neither meteorite has a fusion crust, so it is unclear whether these fractures occurred before or after descent in the Earth's atmosphere (Flynn, 2004). The lack of fusion crust

is not uncommon for meteorites found in the desert (Korotev, 2019). Sand carried by desert winds ablate any surface and can result in the flaking and destruction of a fusion crust (Korotev, 2019). Some of the cracks are filled with terrestrial weathering products such as K-rich material, Ca-carbonates, and or Ba-sulfides; other cracks remain empty.

In NWA 10291 clast 38 contains silica-phase mineral grains adjacent to a large crack or hole. The silica grains are set in Ca-carbonate groundmass. Calcium carbonate has been observed as a terrestrial weathering product in meteorites found in hot desert such as Northwest Africa (e.g. Crozaz and Wadhwa, 2001; Lee and Bland, 2004), and thus could have entered NWA 10291 through cracks and fractures. The Ca-carbonate may have either altered pre-existing silica in C38, or alternatively, the silica grains could also represent terrestrial weathering, since silica has also been noted as hot desert weathering precipitates and is sometimes associated with Ca-carbonate (e.g. Stelzner et al., 1999; Crozaz and Wadhwa, 2001; Lee and Bland, 2004). Therefore, it is more likely that the clast C38 in NWA 10291 represents a terrestrial weathering product instead of representing an igneous crystallization product (impact or igneous related). A second clast in NWA 10291, C30, also contains Ca-carbonate weathering products. This clast contains several mineral grain inclusions (plagioclase, olivine, and pyroxene) set in a vesicular matrix composed of calcium carbonate. A small crack runs from the clast to the edge of the sample. An aqueous solution may have entered the meteorite through this crack, or a crack not visible from this cut of the sample and precipitated the corresponding Ca-carbonate and silica phase (Crozaz and Wadhwa, 2001; Lee and Bland, 2004). These Ca-carbonate and silica weathering products were only found in NWA 10291.

Weathering products in NWA 11182 consist of barite (BaS). Barite, just like Ca-carbonate and silica, has been observed in meteorites found in hot deserts (e.g. Stelzner et al.,

1999; Crozaz and Wadhwa, 2001; Korotev, 2012) and represents a terrestrial weathering product (Lee and Bland, 2004). Barium can be found as a component in desert varnish, which coats much desert material and occurs in aqueous solutions that can intrude hot desert meteorites via cracks where it precipitates out as barite (Lee and Bland, 2003). NWA 11182 contains barite only in veins, holes, and as small grains throughout the sample (Figure 22, 23), indicating that barium most likely precipitated as BaS from an aqueous solution that intruded the rock through a fracture. The small grains most likely represent different cutting effects of veins that run through the sample, since barite in visible veins has the same composition as the single barite grains.

Another indicator for weathering is cracked, pitted, and altered olivine that occurs throughout NWA 11182 as either single mineral grains within the matrix or mineral components in clasts. In some altered olivine, the original olivine composition is preserved, evident texturally and stoichiometrically (Table 5; Figure 8a). In the altered parts of the grain the stoichiometry produces low totals, indicative of the presence of a volatile phase bound within the crystal structure such as water, which can't be measured via EPMA. Most olivine in granulitic clasts is altered. Olivine is the only phase that exhibits such alteration, which suggests an alteration mechanism other than impact as impact processes would 1) affect other minerals as well, and 2) would not result in low totals of the olivine analyses. Olivine is the silicate most susceptible to weathering, due to its mineral structure readily allowing dislocation along the crystallographic b-axis (Goldich, 1938; Wilson, 2004). Moderately acidic aqueous alteration of olivine progresses at least 8 times faster than pyroxene (Franke and Teschner-Steinhardt, 1994). That rate increases with increasing acidity. The hydrous products that olivine is known to weather into are serpentine and iddingsite (e.g., Wicks and Whittaker, 1977; Delvigne et al., 1979; Wilson, 2004). The chemistry of the altered olivine analyzed in this study best matches iddingsite (Table 5). Just

like weathered olivine on Earth generally contains pits, or etched material (Kirby and Wegner, 1978; Wilson, 2004), altered olivine in NWA 11182 also contains pits and cracks. These pit patterns in terrestrial olivine are seen along cracks or planes of weakness within the olivine mineral grain and is suggested to be a product of weathering and not pre-weathering aqueous alteration attributed to serpentinization (Velbel, 2009). The pits may remain empty or fill with precipitates (Lee and Bland,2004; Wilson, 2004; Velbel, 2009).

Altered olivine in Forrest 009, a hot desert L6 chondrite, formed a so called "boxwork" structure observable in BSE image (Figure 8b) that represents a network of connected angular pores (Lee and Bland, 2004). Although the structure seems similar to the texture observed in altered olivine in NWA 11182 (Figure 8), this so called boxwork structure in Forrest 009 olivine formed as a result of dissolution of olivine and pyroxene after 23% of oxidation had occurred and is associated with heavily weathered Fe-Ni metal and troilite grains. In NWA 11182, however, neither high oxidation products are present nor is pyroxene affected by the weathering process, making it unlikely that both meteorites experienced similar weathering history. In addition, NWA 11182 and Forrest 009 were found in different locations, Northwest Africa and western Australia, respectively, which may account for the observed differences in texture (Graham, 1990).

Maturity and pristinity of NWA 10291 and 11182

The relative abundance, shape, and texture of feldspathic regolith breccias can be used to interpret the relative maturity of the regolith from which they consolidated (e.g. McKay et al., 1991; Zeng et al., 2018). Both, NWA 10291 and 11182 contain angular clasts that widely vary in size from a few 10s of microns to several mm. A relative high abundance of the larger clasts comprises material that was either melted and recrystallized by impact events or otherwise

affected by impact related processes (such as granulites). This indicates that both NWA 10291 and 11182 consolidated from relatively mature regolith (e.g. McKay, 1991). Additionally, NWA 10291 contains a glass spherule which is a typical component in regolith (either from volcanic or impact sources) and other impact glass, supporting a more mature regolith formation environment (McKay et al., 1991).

Most of the lithic clasts in NWA 10291 and 11182 are feldspathic and are mostly dominated by anorthitic plagioclase (Figures 10, 12, 14, 16, 18, 20). Figure 24 depicts the anorthite component in plagioclase and Mg# of coexisting mafic phases (olivine and pyroxene) compared to the compositional fields outlined by Goodrich et al. (1984) and Mercer et al. (2013) and is used here to determine the feldspathic clasts' affinity for the ferroan anorthositic suite and the Mg-suite. However, this diagram was originally developed for pristine none-mare (i.e., highland) Apollo samples (Warren and Wasson, 1977; Warren, 2012). Lunar samples are termed "pristine" if they satisfy the following criteria (Warren and Wasson (1977): low siderophile concentration ($< 3 \times 10^{-4}$ x chondrites), low incompatible trace element (ITE) concentration ($< 5 \times 10^{-3}$ x KREEP), grain sizes above 3 mm, ancient age (> 4.2 Ga), mineral composition homogeneity, $^{87}Sr/^{86}Sr < 0.6992$ (indicating products of early differentiation) , and cumulate textures (Warren and Wasson, 1977; Warren, 2012; Gross et al., 2014a). Most feldspathic regolith breccias contain some meteoritic (exogeneous) material in the form of meteoritic metal and NWA 10291 and 11182 are no different (e.g., Goldstein and Yakowitz, 1971; Anders and Grevesse, 1989; Taylor and Day, 2005; Day et al., 2006).

Both NWA 10291 and 11182 contain metal grains with compositions typical for material of exogenous origin (Figure 26). Morland et al. (2019) found Fe-Ni metal in NWA 10989, a meteorite paired to NWA 10291. The metal in NWA 10989 is chemically consistent with

chondrites and iron meteorites (exogenic), rather than endogenic basalts, much like some metal found in NWA 10291 (Morland et al., 2019). These metal grains likely represent material left from impactors. However, one metal grain in NWA 10291 has a Co/Ni ratio more consistent with metal found in Apollo 12, 15 and 17 basalts (Figure 26) (Goldstein and Yakowitz, 1971). Basaltic clasts have been observed in meteorites paired to NWA 10291(Ruzicka et al., 2015, 2017; Bouvier et al., 2016, 2017), supporting the potential basaltic affinity of this metal grain.

By the standards outlined above, NWA 10291 and 11182 as whole rocks and individual lithic clasts within each meteorite, are not pristine because the whole rocks contain some exogenous material and the majority of the clasts are generally smaller than 3 mm in size, meaning too small to contain coarse grained (>3 mm) minerals. However, until more lunar samples are available especially from the FHT either through sample return or meteorites, lunar meteorites represent, as argued by Gross et al. (2014a), the only other data set for characterization of the lunar crust and should not be excluded from consideration (Gross et al., 2014a).

Origin and affinity of clasts and mineral grains in NWA 10291 and 11182 to known lunar rock suites

Almost all the lithic and impact-related clasts in NWA 10291 and 11182 are feldspathic (>70% modally plagioclase) and dominated by anorthitic plagioclase. NWA 10291 has components that range in composition from hyperferroan (anorthosite) to ferroan (anorthositic norite, troctolitic anorthosite, and recrystallized impact melt), while the feldspathic clasts in NWA 11182 mostly fall within the FAN field (recrystallized impact melt, granulites) and intermediate between the FAN and Mg-suite field (anorthosites, granulites, recrystallized impact melt). Rare recrystallized impact melt clasts and granulites extend down to the Fe-rich

hyperferroan composition (Figure 24). Hyperferroan clasts are rare in lunar feldspathic meteorites and have only been reported in anorthosites in ALHA 81005 (Mg# 35) and Northeast Africa 001 (Mg# ~42) (Goodrich et al., 1984; Treiman and Gross, 2013; Gross et al., 2014a). The known lunar lithologies (Mg-suite, alkali suite, and FAN) are all more magnesian than hyperferroan clasts (e.g. Shearer et al., 2015), and therefore, cannot represent any mixtures between those lithologies as they would result in material that is too magnesian in composition to become hyperferroan. Iron-rich material is a late stage magmatic product, according to normal igneous crystallization processes. Therefore, these lithologies must be late-stage products of an evolved melt (Goodrich et al., 1984).

Granulites in NWA 11182 are the most common form of impact-related clasts. They range in composition from ferroan to intermediate between FAN and Mg-suite. Lindstrom and Lindstrom (1986) noticed a bimodal distribution in Apollo granulites. Similarly, the granulites in NWA 11182 appear to form two groups (Figure 25c). One group contains Mg-rich pyroxene that plots within the gap, ranging from Mg# 68 to 84. The second group contains Fe-rich pyroxene and plots within the FAN, ranging from Mg# 54 to 62. The Lilliefors test indicates that these chemistries are likely not sampled from a normally distributed population. Therefore, the bimodality observed in the plots (Figure 25c) may be indicative of two (magnesian or ferroan) granulitic populations. If these rocks are mixtures of Mg-suite and FAN, their chemistry would lie somewhere between the two end member lithologies and would have elevated KREEP, relative to FAN, from the Mg-suite component. Apollo Mg-suite rocks are known to contain evolved phases but unlike NWA 10291, NWA 11182, lacks any evolved lithologies, such as silica or K-rich feldspar. Instead, most rock types in NWA 11182 have a ferroan and magnesian feldspathic highland affinity and, thus, the magnesian material in NWA 11182 is likely not

sourced from the Apollo Mg-suite. However, the granulites in both NWA 10291 and 11182 show an affinity to Mg-suite rocks based on their TiO_2, Cr_2O_3, and FeO/MgO composition, suggesting some level of mixing with Mg-suite material. Therefore, future REE concentrations, especially Th, Sm, and Sc, of these granulites are needed to determine whether they are related to Mg-suite or not (Treiman et al., 2010).

Troctolites, norites, gabbros, and peridotites belonging to the Apollo Mg-suite and alkali-suite and are characterized by the following plagioclase and mafic chemistry: An ~90-95, Fo ~80-90; An ~82-93, Fo ~70-79; and An ~62-93, Fo ~35-74, respectively (Shearer et al., 2015). Most of the clasts in NWA 10292 and 11182 are feldspathic and may be sourced from these Apollo highland rocks or mixtures of them. The gabbroic (An ~88-97, Mg# ~25-70), noritic (An~ 86-98, Mg# ~62-79), and pyroxenitic (An ~90-93, Mg# ~30-48) clasts in NWA 10291 do not perfectly match the aforementioned Apollo highland rocks. However, gabbroic clasts in NWA 10291 may be a mixture of mostly alkali-suite rocks (accounting for the range of Mg#) and some Mg-suite or FAN rocks (accounting for the Ca-richness not entirely expected of Apollo gabbros). The noritic clasts in both NWA 10291 and 11182 and peridotitic clasts in NWA 11182 may also be mixtures of Apollo Mg-suite, alkali-suite, and/or FAN. Pyroxenitic clasts in NWA 10291 share similar chemistries to alkali-suite rocks but may also contain some Ca-rich plagioclase from Mg-suite or FAN. Additionally, some gabbroic, noritic, peridotitic, and pyroxenitic clasts texturally resemble mare basalts. Therefore, some components may have been sourced from or mixed with mare basalts. This would account for the Mg-poor nature of some mafic phases compared to other highland meteorites.

To further investigate the heritage and potential basaltic and Mg-suite/alkali-suite component for NWA 10291 and 11182, the compositional trend in Ti and Fe for pyroxene

mineral grains in the matrix was examined (Figure 30). Pyroxene mineral grains show distinct trends in Ti # vs Fe# for samples from highland and mare basalt origin (e.g. Arai, et al., 1996; Zeng et al., 2018; Hill et al., 2019). The most common types of basalts are classified by their Ti content: very low-Ti (<1 wt% TiO_2), low-Ti (1-6 wt% TiO_2), and high-Ti (>6 wt% TiO_2) (Lucey et al., 2006). Basalts collected at the Apollo 11 and 17 sites are mainly high-Ti basalts, while low-Ti basalts were collected at the Apollo 12, 14, and 15 sites (Lucey et al., 2006). The Apollo 17 site also contained small fragments of very low-Ti basalts in a drill core (Vaniman and Papike, 1977). Lunar basalts are also classified by their Al_2O_3 (>11 wt% = high-alumina) and K (>2000 ppm = high-K) content (Neal and Taylor, 1992; Lucey et al., 2006). Even within these classification schemes, basaltic chemistry varies among samples, notably in FeO content (Lucey et al., 2006). Generally, all basalt types found at Apollo landing sites contain opaque minerals, such as ilmenite, spinel, troilite (FeS), and Fe-Ni metal (Papike and Vaniman, 1978; Neal et al., 1988, 1989). High-Ti basalts from the Apollo 17 landing site contain the opaquest minerals (~24 modal %), while the very low-Ti basalts found at the same landing site contain the least (~1 modal %) (Lucey et al., 2006 and references therein). Most basalts also contain varying amounts of olivine (~0-12 modal %), with the exception of olivine basalts found at the Apollo 12 site (Papike and Vaniman, 1978).

Most of the pyroxene mineral grains in NWA 11182 fall within the compositional field expected for lithic clasts from the lunar highlands (Figure 30a). Pyroxene grains in NWA 10291, however, almost exclusively plot in the compositional field expected for mare basalts, with most pyroxene grains falling in the very low-Ti mare basalt field and some in the low-Ti basaltic field. Though similar in Ti content, basaltic pyroxene grains with Ti content similar to very low-Ti basalts in NWA 10291 have less Al and more Si and Fe than the very low-Ti basalts found at the

Apollo 17 site (Jolliff et al., 2006). Pyroxene grains similar to low-Ti basalts show a similar trend, with high Si and Fe and low Al compared to Apollo basalts (Jolliff et al., 2006). Basalts are largely concentrated on the lunar nearside, in the PKT, with some smaller patches on the farside (Lucey et al., 2006). The SPA terrane, located on the southern farside, also hosts basaltic lava flows with both Ca- and Fe-rich pyroxene, Mg-rich pyroxene, and feldspathic material (Moriarty and Pieters, 2018). Basaltic pyroxene grains in NWA 10291 tend to be more Fe-rich than those found at Apollo sites and SPA is rich in Fe; therefore, basalts located in SPA may be a better match to basaltic pyroxene grains in NWA 10291 than Apollo basalts (e.g. Ohtake et al., 2014). Robinson et al. (2012) showed that high-Ti basalts are overrepresented in the Apollo collection, consistent with the absence of high-Ti basaltic lunar meteorites and the absence of abundant clasts with high-Ti mare basalt affinity in this study. Additionally, some lithic clasts contain chromite inclusions surrounded by pyroxene and plagioclase. Unfortunately, those chromite inclusions are never associated with an olivine phase, preventing the use of chromite-olivine assemblages in determining if clasts have been re-equilibrated (e.g. Prissel et al., 2016 and references therein).

Some silica grains exist in the matrix of NWA 10291 that are unrelated to terrestrial weathering. Silica-phases are late stage crystallization products of normal igneous processing. The crystallographic arrangement informs crystallization conditions. If the silica-phase crystallized deep within the lunar crust, ~10 km deep, then the liquid may have become immiscible (Holmberg and Rutherford, 1994). Under high pressure conditions, a melt can separate into felsic and mafic complementary liquids. This would allow the felsic liquid to evolve slowly, which would form the quartz polymorph. If instead the liquid erupted, the pressure would be low. This would result in the formation of the high temperature silica

polymorphs tridymite or cristobalite (Holleman and Wiberg, 1984; Rykart, 1995; Wenk and Bulakh, 2003). Quartz is less likely to incorporate other cations, such as Al, Na, K, and Ti, than tridymite or cristobalite are, due to the structure of quartz being less open than cristobalite and tridymite (Papike and Cameron, 1976; Smith and Steele, 1984). Comparing the minor element chemistries, most silica in NWA 10291 is more likely to be quartz than cristobalite (Figure 27) (Seddio et al., 2015). One exception is an Fe-rich, Ti-poor silica grain associated with the symplectite C19. The elevated Fe content of the silica is likely due to the breakdown of low-Ca pyroxene and the redistribution of Fe in the clast. However, future collection of Raman spectral data of these phases is critical to classify the polymorph.

The formation of the silica in NWA 10291 could be achieved through processes such as fractional crystallization of KREEP or another evolved liquid (e.g. Longhi, 1990) and thus would represent fragments of felsic material typically found in the Apollo sample collection. Another process to form silica is represented by silicate liquid immiscibility (e.g. Hess et al., 1975; Rutherford et al., 1976; Neal and Taylor, 1989; Jolliff, 1991). Silicate liquid immiscibility similarly requires extensive fractionation of a melt. After 90-98% melt crystallization the magma may unmix and form two coexisting liquids, one Fe-rich, the other Si-rich (Roedder and Weiblen, 1970, 1971, 1972; Jolliff and Floss, 1997). The Si-rich liquid is then suggested to be the parent magma of silicic lunar rocks. However, Th preferentially goes into the Fe-rich liquid, yet Si-rich lunar rocks are high in Th (Hess and Rutherford, 1974; Neal and Taylor, 1989; Jolliff, 1991, 1998; Shearer et al., 2001; Lawrence et al., 2005; Hagerty et al., 2006). A third process that forms silica is partial melting of crustal material via crustal heating (e.g. Lawrence et al., 2005; Hagerty et al., 2006). Some terrestrial Si-rich rocks are created by partial melting of the crust. In such a scenario, the crust is heated by local warm, intruding magma and produces a

highly evolved magma capable of crystallizing Si-rich phases (e.g. Annen and Sparks, 2002). This process, however, has not been investigated in terms of lunar rocks and the lunar environment (Gullikson et al., 2016).

Origin and heritage of NWA 10291 and 11182 to crustal source regions on the Moon

The formation of the Mg-suite is not well understood (e.g. Shearer et al., 2015). Mafic minerals in Mg-suite rocks are Mg-rich and are, therefore, considered primitive (e.g. James, 1980; Papike et al., 1998; Shearer et al., 2015). Unexpectedly, however, many Mg-suite rocks also contain KREEP, which is indicative of generation from an evolved magma (e.g. Longhi et al., 2010; Shearer et al., 2015). Additionally, the coexistence of Mg-rich mafics with Ca-rich plagioclase in Mg-suite troctolites is unexpected (e.g. Warren, 1986; Wieczorek et al., 2006; Longhi et al., 2010; Shearer et al., 2015). Most basaltic melts lower the Mg concentration of the melt by crystallizing olivine before plagioclase (e.g. Hess, 1994; Prissel et al., 2016). Therefore, less Mg is available to incorporate into mafic phases that co-crystallize with plagioclase. This results in plagioclase associated with more Fe-rich mafics; a combination unlike that of Mg-suite troctolites (e.g. Hess, 1994; Prissel et al., 2016). Several formation mechanisms have been suggested to describe the complex petrogenetic history of Mg-suite rocks, such as: crystallization products of the LMO (e.g. Wood, 1975; Longhi and Boudreau, 1979; McCallum, 1983), ascent of Mg-rich melt that assimilates surrounding, evolved material (e.g. Warren and Wasson, 1977; Longhi, 1981; James and Flohr, 1983; Warren, 1986; Ryder, 1991; Papike et al., 1994, 1996; Prissel et al., 2016), hybrid cumulate re-melting in the deep or shallow mantle (e.g. Shearer and Floss, 1999; Shearer and Papike, 1999, 2005; Elardo et al., 2011).

Early investigations of the Mg-suite suggested that Mg-suite rocks were produced during crystallization of the LMO, contemporaneously with FAN (Wood, 1975). The cumulate nature of

Mg-suite rocks, and their dissimilar chemistry compared to FAN, was argued to be a byproduct of crystallization style; plagioclase in FAN formed via equilibrium crystallization, while Mg-suite crystals formed via fractional crystallization (Longhi and Boudreau, 1979). Similar crystallization trends in Mg# of mafics versus An of plagioclase were found at the Stillwater Complex on Earth (Raedeke and McCallum, 1980). One trend is vertical, like FAN, while the other is positively-sloped, like Mg-suite. The vertical trend was suggested to be the result of equilibrium crystallization, while the sloped trend was suggested to be the result of fractional (Raedeke and McCallum, 1980). However, trace elements of Mg-suite and FAN parental magmas are different, indicating that the two types of rock represent two distinct magmas (Norman and Ryder, 1979; Raedeke and McCallum, 1980; Warren and Wasson, 1977; James and Flohr, 1983; Warren, 1983, 1986). The difficulties reconciling distinct magmas within the LMO sparked further consideration of Mg-suite petrogenesis.

Other models explore the formation of Mg-suite magmas post-LMO crystallization. These models suggest either assimilation of evolved LMO products or hybrid mixing in the deep or shallow mantle are responsible for the formation of the Mg-suite (e.g. Warren and Wasson, 1977; Longhi, 1981; James and Flohr, 1983; Warren, 1986; Ryder, 1991; Papike et al., 1994, 1996; Shearer and Floss, 1999; Shearer and Papike, 1999, 2005; Elardo et al., 2011). Assimilation of evolved LMO products, such as KREEP and anorthosite, in a Mg-rich melt has been suggest to produce the unique, primitive (Mg-rich) yet evolved (KREEP-rich) Mg-suite (e.g. Warren and Wasson, 1977; Longhi, 1981; James and Flohr, 1983; Warren, 1986; Ryder, 1991; Papike et al., 1994, 1996; Prissel et al., 2016). However, Al diffuses in basaltic melts (~10^{-12} – 10^{-11} m^2s^{-1}) on timescales similar to those on which magmatic intrusions cool (Finnila et al., 1994). Therefore, the Mg-rich melts may not be able to incorporate enough evolved material to

produce the chemistry observed (Shearer and Floss, 1999). Though beholden to the same Al diffusion rate (i.e., incorporation of Al into the Mg-rich melt via melting of anorthosite), hybrid mixing models may produce enough heat to melt and mix more rapidly (Shearer et al., 2015), though Al-rich melts yield pink spinel – an accessory mineral phase found only in a fraction of lunar troctolites (Prissel et al., 2016).

Mantle overturn is the process by which less dense material in the mantle rises while denser material sinks (e.g. Hess and Parmentier, 1995; Zhong et al., 2000; Parmentier et al., 2002; Stegman et al., 2003; Elkins-Tanton et al., 2002, 2003; Shearer et al., 2006). Overturn of the cumulate pile may have either transported KREEP material deep in the mantle, where it mingled with early LMO cumulates, or resulted in early LMO cumulates rising to the base of the crust (e.g. Shearer and Floss, 1999; Shearer and Papike, 1999, 2005; Elardo et al., 2011). The large volume of primitive material deposited beneath the crust may provide enough heat to assimilate evolved material at the base of the crust and produce rocks with Mg-rich mafics and anorthite and, perhaps, KREEP (Shearer et al., 2015). It is unclear whether Mg-suite rocks require KREEP to form the Mg-suite and be considered part of the Mg-suite or if proximity to the PKT enriched some Mg-suite magmas in KREEP (e.g. Papike et al., 1998; Takeda et al., 2006; Lucey and Cahill, 2009; Cahill et al., 2009; Taylor, 2009; Gross and Treiman, 2011; Prissel et al., 2014, 2016; Shearer et al., 2015). If KREEP is not required for Mg-suite magmatism, then clasts in NWA 10291 and 11182 resembling Mg-suite may be sourced from the far side, away from the PKT.

MAN is a common rock type in lunar feldspathic breccias (e.g. Gross et al., 2014a). It was suggested that MAN is difficult to explain as a sole crystallization product of a simple LMO (Gross et al., 2014a). Those rocks, instead, may have formed from the cooling of individual

diapirs, rich in primitive (magnesian) material (Gross et al., 2014a). Charlier et al. (2018), however, produced an LMO model that detailed phases and chemistry of phases as the LMO cooled. This model was able to produce MAN, with appropriately high Mg# (>70), from a simple LMO crystallization sequence and did not have to evoke other formation processes (Charlier et al., 2018). Remote sensing and abundance in lunar meteorites suggest that these rocks may be a significant proportion of the lunar crust; so clasts, such as those found in NWA 10291 and NWA 11182 are resources that can be used to understand the evolution of MAN (Takeda et al., 2006; Treiman et al., 2010; Gross et al., 2014a).

Basalts are largely concentrated on the lunar nearside in the PKT and in a few basins on the farside including SPA (Head, 1976; Robinson et al., 2012; Mercer et al., 2013; Wang and Zhao, 2018). Basalt fragments in regolith breccia meteorites mostly represent basalt flows within a few hundred kilometers of the meteorite's source region (Delano 1975; Vaniman et al. 1978; Zeigler et al. 2006; Robinson et al., 2012). Basaltic fragments and mineral grains can be incorporated into feldspathic breccias by a process in which ejecta gets laterally dispersed from impacts on nearby maria (Robinson et al., 2012). Therefore, identification of different types of mare basalts in individual meteorites could potentially help constrain the meteorite's provenance, by comparing basalt composition with remotely sensed compositional data, such as bulk TiO_2 content to remotely measured surface values of TiO_2 (Joy et al. 2008; Arai et al. 2010; Basilevsky et al.2010; Robinson et al., 2012).

In addition to basaltic material, the PKT also contains rocks from the alkali-suite, Mg-suite, and material enriched in incompatible elements (KREEP). Such late-stage magmatic products are present in NWA 10291, in phases such as Na-rich plagioclase, quartz, apatite, and zircon. Thorium is used as a marker for KREEP-rich material (Jolliff et al., 2000). Bulk rock

incompatible data has been collected for some meteorites paired to NWA 10291 (Ruzicka et al., 2015, 2017; Bouvier et al., 2016, 2017). The bulk composition of the reported meteorites indicates that the group consists of feldspathic, highland lithologies with some mare material (Figure 28), which is consistent with the clasts in NWA 10291. Thorium content of NWA 10291 paired meteorites is low (<1.0 ppm), which is consistent with Th levels measured in the lunar highlands (< 3 ppm) (Wieczorek et al., 2006; Ruzicka et al., 2015, 2017; Bouvier et al., 2016, 2017). The bulk FeO content of NWA 10291 paired stones (~7.3 wt%) is also consistent with FeO surface composition of the FHT (< 10 wt%) as measured by Lunar Prospector (Lawrence et al., 2002; Ruzicka et al., 2015, 2017; Bouvier et al., 2016, 2017). Thus, based on the very low bulk Th and FeO content of paired stones, NWA 10291 most likely originated from the FHT. However, based on the abundance of very-low Ti basaltic affinity of pyroxene grains in the matrix and the presence of some evolved mineral fragments and clasts, NWA 10291 most likely originated from a region in which FHT and KREEP-rich material got mixed. Such regions exist on the lunar nearside, chemically similar to the Apollo 16 landing site and on the lunar farside near SPA, chemically similar to the origin of meteorite NWA 2996 (Mercer et al., 2013).

The South Pole-Aitken basin (SPA) is a 2,500 km diameter basin located on the southern farside (Spudis et al., 1994; Garrick-Bethell and Zuber, 2009). Formation models suggest that the impactor may been large enough to excavate mantle material (Melosh et al., 2017); however, the basin lacks strong remote sensing indications of olivine, which is an expected mantle component (Lucey, 2004). Instead, the floor of the basin contains feldspathic lithologies rich in low- and high-Ca pyroxene, as well as mare basalt (Pieters et al., 1997, 2001; Lucey, 2004; Mercer et al., 2013; Ohtake et al., 2014; Crites and Lucey, 2015; Moriarty and Pieters, 2018). Recent observations have also noted the presence of small concentrations of olivine toward the outer

ring of SPA (Zhang et al., 2019). Additionally, SPA has anomalously high concentrations of FeO, TiO_2, K, and Th relative to the FHT (e.g., Lucey et al. 1998; Gillis et al. 2004; Kobayashi et al. 2010; Yamashita et al. 2010), but low concentrations of these elements relative to the PKT (e.g., Jaumann et al., 2012 and references therein). The SPA impactor may have excavated this KREEP material from depth, in compliance with the magma ocean model (Jolliff et al., 2000, 2011; Lawrence et al., 2000, 2007). Alternatively, the impactor may have produced a large impact melt pool that differentiated during cooling, separating the dense olivine from the lighter KREEP material (Hurwitz and Kring, 2014; Vaughan and Head, 2014).

Various model calculations estimate the ejecta thickness expected a certain distance away from a crater center (Melosh, 1989; Kruger et al., 2017). Thickness of ejecta scales with distance from crater by a power of -3. If we take t_e to be ejecta thickness, R_T to be transient crater radius (the initial cavity created before ejecta fills the newly formed basin and more complex features form, such as rings and a central peak), and r to be distance from the center of the crater:

$$t_e = 0.033 R_T \left(\frac{r}{R_T}\right)^{-3}$$

(Melosh, 1989). Estimates of transient crater diameter of SPA range from a minimum of 1160 km to a maximum of 1470 km (Spudis, 1993). For both SPA endmember transient crater sizes, ejecta thickness drops below 1 km at a distance of ~3000 km from the center of SPA and below 10 m at a distance of ~10000 km. The circumference of the Moon is only ~11000 km, so the SPA basin ejecta likely coated much of the farside. In fact, it has been suggested that ejecta from the formation of SPA covered just over 50% of the lunar surface ~4.1 Ga (Hiesinger and Head, 2006). The ejecta would have been reworked and mixed with existing rock, producing part of the lunar regolith (Lucey et al., 2006). The mixing rate of the lunar regolith (i.e., burying regolith that has been exposed to surface effects), identified by observations of the Apollo 12 regolith

cores, is 100 μm per 1 million year (Morris, 1978). More recent estimates of regolith mixing rate have been calculated using dust density distribution measured by the Lunar Atmosphere and Dust Environmental Explorer (LADEE) (Szalay and Horanyi, 2016). Those estimates identify regolith mixing at a rate of 40 μm per 1 million year (Szalay and Horanyi, 2016).

Impacts and secondary impacts allow for mixing of crustal lithologies, such as MAN and FAN and can transport lithologies 100s-1000s of meters (Petro and Pieters, 2008). NWA 11182 most likely originated from a region rich in MAN and FAN highland material, explaining the bimodal distribution of the granulite clasts. Such a region would be located far from the PKT, such as between the FHT (more magnesian) and the nearside highland terrane (more ferroan). Future bulk composition measurements, including REE concentrations, will determine is NWA 11182 contains an Mg-suite component (enriched in KREEP) and restrict the source region of NWA 11182 by comparing its bulk composition to Lunar Prospector data sets (Joy et al., 2010, 2011).

Meteorites from the SPA region, or with SPA ejecta, most likely contain a mixture of mafic crustal lithologies, ultramafic impact-melt, feldspathic crustal material, some mare basalt, and perhaps some mantle material. Additionally, SPA contains elevated concentrations of both clino- and orthopyroxene (Crites and Lucey, 2015; Zhang et al., 2019). Orthopyroxene is notably absent from much of the PKT in lunar surface maps but is abundant throughout the FHT and SPA (Crites and Lucey, 2015). Olivine is also found remotely in greater concentration in SPA compared to the surrounding highlands, though present in abundance in the PKT (Zhang et al., 2019). To date, only two known meteorites have may have originated from SPA: Dhofar 961 (Jolliff et al., 2007, 2009; Korotev et al., 2007) and NWA 2996 (Mercer et al., 2013). Given the very low concentration of Th and FeO in NWA 10291, the diverse clast variety (ranging from

feldspathic crustal rocks, to mafic crustal material, to very low-Ti basaltic affinity of the pyroxene grains), and the high abundance of low- and high-Ca pyroxene grains relative to olivine in clasts and the matrix, NWA 10291 most likely originated from the FHT within the vicinity of SPAT. Derivation from the SPA region (moderate KREEP composition), as opposed to the PKT (KREEP-rich), would explain the few evolved lithologies and mineral grains. To fully distinguish between an origin of the nearside feldspathic region similar to the Apollo 16 landing site and an origin of the FHT near the SPAT, the method outlined in Joy et al (2010, 2011) should be applied, in which the Lunar Prospector gamma-ray spectrometer datasets can be searched for source regions using the bulk composition as parameters (Robinson et al., 2012; Mercer et al., 2013).

CONCLUSION

Lunar meteorites are an important resource in lunar studies. They are a random sampling of the surface and therefore are a better representation of average crustal composition than current return samples (Korotev, 2005). Northwest Africa (NWA) 10291 is a lunar feldspathic breccia that contains several evolved minerals, including silica, Na- and K-rich plagioclase, apatite, hyperferroan mafics, and zircon. Bulk FeO and Th concentrations measured on meteorites paired with NWA 10291 are consistent with (1) derivation from the farside Feldspathic Highlands Terrane (FHT). The diversity of clast types in NWA 10291 suggests mixing of non-adjacent rock types, perhaps near the South Pole-Aitken Terrane (SPAT), where evolved lithologies, basalts, and low- and high-Ca pyroxene have been recorded. Or (2) NWA 10291 could have formed from a FHT area similar to Apollo 16 highland areas, far from KREEP-bearing terrane (K, rare-earth elements, P). NWA 11182 is also a lunar feldspathic breccia and contains many impact-related clasts, most of which are granulites. The lithic and impact-related clasts in NWA 11182 are lithologically diverse and span the range measured in feldspathic lunar meteorites, from Mg# ~40-80. The granulites in NWA 11182 form a bimodal distribution, which indicates two protoliths (ferroan anorthosite [FAN] and magnesian anorthosite [MAN]). Judging from the presence of FAN-related rocks, the lack of KREEP in the form of evolved lithologies, and granulites with MAN composition, NWA 11182 likely formed from an area between the near side and the far side highland areas.

Both meteorites show evidence of terrestrial weathering. Some silica in NWA 10291 is associated with a Ca-carbonate phase. These minerals are always associated with a nearby crack, suggesting that terrestrial carbonates may have intruded the rock along these fractures and precipitated the observed phases. NWA 11182 does not have carbonates, but rather many barite-

filled veins and holes, a precipitate of hot desert weathering. Additionally, most olivine in NWA 11182 shows evidence of alteration in the form of iddingsite precipitates. The altered olivine is pitted along small fractures in the mineral and cracked, which is a product of terrestrial weathering also seen in terrestrial olivine. The altered olivine phases, like Ca-carbonate in NWA 10291, are also associated with nearby cracks, which suggests that weathering material may have intruded along those fractures.

Additional data is still required to fully understand these meteorites. For example, Raman spectroscopy of the silica-phases in NWA 10291 will reveal the specific silica polymorph. Since polymorphs form under different pressure and temperature conditions, understanding its crystalline structure will inform its crystallization history. Additionally, REE measurements of clasts in NWA 10291 and 11182 are required to determine if compositionally intermediate clasts are simple mixtures of Mg-suite and FAN (would have elevated KREEP) or are more similar to MAN (no KREEP component). Bulk composition measurements of NWA 11182 are required for comparison with remote sensing spectral data. Comparing the bulk chemistries of NWA 10291 and 11182 to remote sensing spectral datasets will further constrain their source regions.

REFERENCES

Anand, M., Taylor, L. A., Misra, K. C., Demidova, S. I., and Nazarov, M. A. (2003). KREEPy lunar meteorite Dhofar 287A: A new lunar mare basalt. *Meteoritics and Planetary Science*, *38*(4), 485-499.

Anders, E. and Grevesse, N. (1989). Abundances of the elements: Meteoritic and solar. *Geochimica et Cosmochimica acta*, *53*(1), 197-214.

Annen, C., and Sparks, R. S. J. (2002). Effects of repetitive emplacement of basaltic intrusions on thermal evolution and melt generation in the crust. *Earth and Planetary Science Letters*, *203*(3-4), 937-955.

Arai, T., Hawke, B. R., Giguere, T. A., Misawa, K., Miyamoto, M., and Kojima, H. (2010). Antarctic lunar meteorites Yamato-793169, Asuka-881757, MIL 05035, and MET 01210 (YAMM): Launch pairing and possible cryptomare origin. *Geochimica et Cosmochimica Acta*, *74*(7), 2231-2248.

Arndt, J., Engelhardt, W. V., Gonzalez-Cabeza, I., and Meier, B. (1984). Formation of Apollo 15 green glass beads. *Journal of Geophysical Research: Solid Earth*, *89*(S01), C225-C232.

Basilevsky, A. T., Neukum, G., and Nyquist, L. (2010). The spatial and temporal distribution of lunar mare basalts as deduced from analysis of data for lunar meteorites. *Planetary and Space Science*, *58*(14-15), 1900-1905.

Beck, A. W., Viviano, C. E., and McCoy, T. J. (2013). Limitations of Sample Size in Meteorite Thin Section and Spectroscopic Studies: Implications for the HEDs and Vesta. In Lunar and Planetary Science Conference (Vol. 44, p. 3069).

Berlin, J., Jones, R. H., and Brearley, A. J. (2011). Fe-Mn systematics of type IIA chondrules in unequilibrated CO, CR, and ordinary chondrites. Meteoritics and Planetary Science, 46(4), 513-533.

Best, M. G. (1982). *Igneous and Metamorphic Petrology*. New York, NY: W. H. Freeman and Company.

Bouvier, A., Gattacceca, J., Grossman, J., and Metzler, K. (2016). The Meteoritical Bulletin, No. 105. *Meteoritics and Planetary Science*, *52*.

Bouvier, A., Gattacceca, J., Agee, C., Grossman, J., and Metzler, K. (2017). The Meteoritical Bulletin, No. 104. *Meteoritics and Planetary Science*, *52*(10), 2284-2284.

Cahill, J. T. S., Lucey, P. G., and Wieczorek, M. A. (2009). Compositional variations of the lunar crust: Results from radiative transfer modeling of central peak spectra. Journal of Geophysical Research: Planets, 114(E9).

Charlier, B., Grove, T. L., Namur, O., and Holtz, F. (2018). Crystallization of the lunar magma ocean and the primordial mantle-crust differentiation of the Moon. Geochimica et Cosmochimica Acta, 234, 50-69.

Clayton, R. N., Onuma, N., and Mayeda, T. K. (1976). A classification of meteorites based on oxygen isotopes. *Earth and Planetary Science Letters*, *30*(1), 10-18.

Crites, S. T., and Lucey, P. G. (2015). Revised mineral and Mg# maps of the Moon from integrating results from the Lunar Prospector neutron and gamma-ray spectrometers with Clementine spectroscopy. American Mineralogist, 100(4), 973-982.

Crozaz, G., and Wadhwa, M. (2001). The terrestrial alteration of Saharan shergottites Dar al Gani 476 and 489: A case study of weathering in a hot desert environment. *Geochimica et Cosmochimica Acta*, *65*(6), 971-977.

Cushing, J. A., Taylor, G. J., Norman, M. D., and Keil, K. (1999). The granulitic impactite suite: Impact melts and metamorphic breccias of the early lunar crust. *Meteoritics and Planetary Science*, *34*(2), 185-195.

Day, J. M., Taylor, L. A., Floss, C., Patchen, A. D., Schnare, D. W., and Pearson, D. G. (2006). Comparative petrology, geochemistry, and petrogenesis of evolved, low-Ti lunar mare basalt meteorites from the LaPaz Icefield, Antarctica. *Geochimica et Cosmochimica Acta*, *70*(6), 1581-1600.

Delano, J. W. (1975). Petrology of the Apollo 16 mare component-Mare Nectaris. In *Lunar and Planetary Science Conference Proceedings* (Vol. 6, pp. 15-47).

Delano, J. W. (1979). Apollo 15 green glass-chemistry and possible origin. In *Lunar and Planetary Science Conference Proceedings* (Vol. 10, pp. 275-300).

Delano, J. W. (1986). Pristine lunar glasses: Criteria, data, and implications. *Journal of Geophysical Research: Solid Earth*, *91*(B4), 201-213.

Delvigne, J., Bisdom, E. B. A., Sleeman, J., and Stoops, G. (1979). *Olivines, their pseudomorphs and secondary products*. Stiboka.

Devore, J. L. (2015). Probability and Statistics for Engineering and the Sciences. Cengage Learning.

Dowty, E., Prinz, M., and Keil, K. (1974). Ferroan anorthosite: A widespread and distinctive lunar rock type. *Earth and Planetary Science Letters*, *24*(1), 15-25.

Elardo, S. (2016). Lunar Magma Ocean Theory, Origins, and Rationale. *Encyclopedia of Lunar Science*, 1-8.

Elardo, S. M., Draper, D. S., and Shearer Jr, C. K. (2011). Lunar Magma Ocean crystallization revisited: Bulk composition, early cumulate mineralogy, and the source regions of the highlands Mg-suite. Geochimica et Cosmochimica Acta, 75(11), 3024-3045.

Elardo, S. M., Shearer, C. K., and McCubbin, F. M. (2017). The Role of KREEP in the Production of Mg-Suite Magmas and Its Influence on the Extent of Mg-Suite Magmatism in the Lunar Crust.

Elkins-Tanton, L. T. (2008). Linked magma ocean solidification and atmospheric growth for Earth and Mars. *Earth and Planetary Science Letters*, *271*(1-4), 181-191.

Elkins-Tanton, L. T. (2012). Magma oceans in the inner solar system. *Annual Review of Earth and Planetary Sciences*, *40*, 113-139.

Elkins-Tanton, L. T., Burgess, S., and Yin, Q. Z. (2011). The lunar magma ocean: Reconciling the solidification process with lunar petrology and geochronology. *Earth and Planetary Science Letters*, *304*(3-4), 326-336.

Elkins-Tanton, L. T., Chatterjee, N., and Grove, T. L. (2003). Magmatic processes that produced lunar fire fountains. *Geophysical Research Letters*, *30*(10).

Elkins-Tanton, L. T., Parmentier, E. M., and Hess, P. C. (2003). Magma ocean fractional crystallization and cumulate overturn in terrestrial planets: Implications for Mars. *Meteoritics and Planetary Science*, *38*(12), 1753-1771.

Elkins-Tanton, L. T., Van Orman, J. A., Hager, B. H., and Grove, T. L. (2002). Re-examination of the lunar magma ocean cumulate overturn hypothesis: melting or mixing is required. *Earth and Planetary Science Letters*, *196*(3-4), 239-249.

Fagan, T. J. (2007). Formation of symplectite-like inclusions by direct quenching from igneous liquid in lunar meteorite NWA 773. *Meteoritics and Planetary Science Supplement*, *42*, 5204.

Fagan, T.J., Taylor, G.J., Keil, K., Bunch, T.E., Wittke, J.H., Korotev, R.L., Jolliff, B.L., Gillis, J.J., Haskin, L.A., Jarosewich, E. and Clayton, R.N. (2002). Northwest Africa 032: Product of lunar volcanism. *Meteoritics and Planetary Science*, *37*(3), 371-394.

Finnila, A. B., Hess, P. C., and Rutherford, M. J. (1994). Assimilation by lunar mare basalts: Melting of crustal material and dissolution of anorthite. Journal of Geophysical Research: Planets, 99(E7), 14677-14690.

Flynn, G. J. (2004). Physical properties of meteorites and interplanetary dust particles: Clues to the properties of the meteors and their parent bodies. *Earth, Moon, and Planets*, *95*(1-4), 361-374.

Franke, W. A., and Teschner-Steinhardt, R. (1994). An experimental approach to the sequence of the stability of rock-forming minerals towards chemical weathering. *Catena*, *21*(2-3), 279-290.

Ganino, C., Libourel, G., Nakamura, A. M., Jacomet, S., Tottereau, O., and Michel, P. (2018). Impact-induced chemical fractionation as inferred from hypervelocity impact experiments with silicate projectiles and metallic targets. *Meteoritics and Planetary Science*, *53*(11), 2306-2326.

Garrick-Bethell, I., and Zuber, M. T. (2009). Elliptical structure of the lunar South Pole-Aitken basin. Icarus, 204(2), 399-408.

Gattacceca, J., Bouvier, A., Grossman, J., Metzler, K., and Uehara, M. (2019). The Meteoritical Bulletin, No. 106. *Meteoritics and Planetary Science*, *54*(2), 469-471.

Gillis, J. J., Jolliff, B. L., and Korotev, R. L. (2004). Lunar surface geochemistry: Global concentrations of Th, K, and FeO as derived from lunar prospector and Clementine data. *Geochimica et Cosmochimica Acta*, *68*(18), 3791-3805.

Glotch, T.D., Lucey, P.G., Bandfield, J.L., Greenhagen, B.T., Thomas, I.R., Elphic, R.C., Bowles, N., Wyatt, M.B., Allen, C.C., Hanna, K.D. and Paige, D.A. (2010). Highly silicic compositions on the Moon. *science*, *329*(5998), 1510-1513.

Goldich, S. S. (1938). A study in rock-weathering. *The Journal of Geology*, *46*(1), 17-58.

Goldstein, J. I., and Yakowitz, H. (1971). Metallic inclusions and metal particles in the Apollo 12 lunar soil. In *Lunar and Planetary Science Conference Proceedings* (Vol. 2, p. 177).

Goodrich, C. A., and Delaney, J. S. (2000). Fe/Mg–Fe/Mn relations of meteorites and primary heterogeneity of primitive achondrite parent bodies. *Geochimica et Cosmochimica Acta*, *64*(1), 149-160.

Goodrich, C. A., Taylor, G. J., Keil, K., Boynton, W. V., and Hill, D. H. (1984). Petrology and chemistry of hyperferroan anorthosites and other clasts from lunar meteorite ALHA81005. *Journal of Geophysical Research: Solid Earth*, *89*(S01).

Graham, A. L. (1990). Meteoritical Bulletin, No. 68. *Meteoritics*, *25*.

Grimm, R. E. (2013). Geophysical constraints on the lunar Procellarum KREEP Terrane. Journal of Geophysical Research: Planets, 118(4), 768-778.

Gross J. (2014). Can chondrite clasts in lunar meteorite Allan Hills A81005 constrain early solar system processes? Evidence from oscillatory zoning in olivine. *77th Annual Meteoritical Society Meeting;* #5381.

Gross, J. and Joy, K. H. (2016). Evolution, lunar: from magma ocean to crust formation. Encyclopedia of lunar science, 1-20.

Gross, J., and Treiman, A. H. (2011). Unique spinel-rich lithology in lunar meteorite ALHA 81005: Origin and possible connection to M3 observations of the farside highlands. *Journal of Geophysical Research: Planets*, *116*(E10).

Gross, J., Treiman, A. H., and Mercer, C. N. (2014a). Lunar feldspathic meteorites: Constraints on the geology of the lunar highlands, and the origin of the lunar crust. *Earth and Planetary Science Letters*, *388*, 318-328.

Gross, J., Isaacson, P. J., Treiman, A. H., Le, L. and Gorman, J. K. (2014b). Spinel-rich lithologies in the lunar highland crust: Linking lunar samples with crystallization experiments and remote sensing. American Mineralogist, 99(10), 1849-1859.

Gullikson, A. L., Hagerty, J. J., Reid, M. R., Rapp, J. F., and Draper, D. S. (2016). Silicic lunar volcanism: Testing the crustal melting model. *American Mineralogist*, *101*(10), 2312-2321.

Hagerty, J. J., Lawrence, D. J., Hawke, B. R., Vaniman, D. T., Elphic, R. C., and Feldman, W. C. (2006). Refined thorium abundances for lunar red spots: Implications for evolved, nonmare volcanism on the Moon. *Journal of Geophysical Research: Planets*, *111*(E6).

Hamann, C., Fazio, A., Ebert, M., Hecht, L., Wirth, R., Folco, L., Deutsch, A. and Reimold, W.U. (2018). Silicate liquid immiscibility in impact melts. *Meteoritics and Planetary Science*, *53*(8), 1594-1632.

Haskin, L.A. (2000). Basin impacts, especially large and late Imbrium. In *Workshop on New Views of the Moon III: Synthesis of sample analysis, on-surface investigation, and remote sensing information*. Lunar and Planetary Institute, p. 12.

Head, J. W. (1976). The significance of substrate characteristics in determining morphology and morphometry of lunar craters. In *Lunar and Planetary Science Conference Proceedings* (Vol. 7, pp. 2913-2929).

Heiken, G., and McKay, D. S. (1974). Petrography of Apollo 17 soils. In *Lunar and Planetary Science Conference Proceedings* (Vol. 5, pp. 843-860).

Hem, J. D. (1972). Chemical factors that influence the availability of iron and manganese in aqueous systems. *Geological Society of America Bulletin*, *83*(2), 443-450.

Hess, P. C. (1994). Petrogenesis of lunar troctolites. Journal of Geophysical Research: Planets, 99(E9), 19083-19093.

Hess, P. C. and Rutherford, M. J. (1974). Element fractionation between immiscible melts. In *Lunar and Planetary Science Conference* (Vol. 5).

Hess, P. C. and Parmentier, E. M. (1995). A model for the thermal and chemical evolution of the Moon's interior: Implications for the onset of mare volcanism. Earth and Planetary Science Letters, 134(3-4), 501-514.

Hess, P. C., Rutherford, M. J., Guillemette, R. N., Ryerson, F. J., and Tuchfeld, H. A. (1975). Residual products of fractional crystallization of lunar magmas-an experimental study. In *Lunar and Planetary Science Conference Proceedings* (Vol. 6, pp. 895-909).

Hiesinger, H., and Head III, J. W. (2006). New views of lunar geoscience: An introduction and overview. *Reviews in mineralogy and geochemistry*, *60*(1), 1-81.

Hill, P. J., Osinski, G. R., Banerjee, N. R., Korotev, R. L., Nasir, S. J., and Herd, C. D. (2019). Petrography and geochemistry of lunar meteorites Dhofar 1673, 1983, and 1984. *Meteoritics and Planetary Science*, *54*(2), 300-320.

Holleman, A.F. and Wiberg, E. (1984). Lehrbuch Der Anorganischen Chemie. Berlin, New York: Walter Gruyter Verlag, ISBN 3-11-007511-3.

Holmberg, B., and Rutherford, M. J. (1994, March). An experimental study of KREEP basalt evolution. In *Lunar and Planetary Science Conference* (Vol. 25, p. 557).

Hudgins, J. A., Spray, J. G., Kelley, S. P., Korotev, R. L., and Sherlock, S. C. (2008). A laser probe 40Ar/39Ar and INAA investigation of four Apollo granulitic breccias. *Geochimica et Cosmochimica Acta*, *72*(23), 5781-5798.

Hurwitz, D. M., and Kring, D. A. (2014). Differentiation of the South Pole–Aitken basin impact melt sheet: Implications for lunar exploration. Journal of Geophysical Research: Planets, 119(6), 1110-1133.

James, O. B. and Flohr, M. K. (1983). Subdivision of the Mg-suite noritic rocks into Mg-gabbronorites and Mg-norites. Journal of Geophysical Research: Solid Earth, 88(S02), A603-A614.

Jaumann, R., Hiesinger, H., Anand, M., Crawford, I.A., Wagner, R., Sohl, F., Jolliff, B.L., Scholten, F., Knapmeyer, M., Hoffmann, H. and Hussmann, H. (2012). Geology, geochemistry, and geophysics of the Moon: Status of current understanding. *Planetary and Space Science*, *74*(1), 15-41.

Jolliff, B. L. (1991). Fragments of quartz monzodiorite and felsite in Apollo 14 soil particles. In *Lunar and Planetary Science Conference Proceedings* (Vol. 21, pp. 101-118).

Jolliff, B. L. (1998). Large-scale separation of K-frac and REEP-frac in the source regions of Apollo impact-melt breccias, and a revised estimate of the KREEP composition. *International Geology Review*, *40*(10), 916-935.

Jolliff, B. L. and Floss, C. (1997). Liquid immiscibility in a lunar plutonic setting and the evolution of KREEPy residual melts. In *Lunar and Planetary Science Conference* (Vol. 28, p. 673).

Jolliff, B. L., Gillis, J. J., Haskin, L. A., Korotev, R. L., and Wieczorek, M. A. (2000). Major lunar crustal terranes: Surface expressions and crust-mantle origins. *Journal of Geophysical Research: Planets*, *105*(E2), 4197-4216.

Jolliff, B. L., Zeigler, R. A., Korotev, R. L., and Carpenter, P. K. (2007). Lunar meteorite Dhofar 961, MAFIC impact-melt breccia: petrographic components and possible provenance. *Meteoritics and Planetary Science Supplement*, *42*, 5311.

Jolliff, B. L., Korotev, R. L., Zeigler, R. A., and Prettyman, T. H. (2009). Connecting lunar meteorite Dhofar 961 to the South Pole-Aitken Basin through Lunar Prospector gamma-ray data. In *Lunar and Planetary Science Conference* (Vol. 40).

Jolliff, B.L., Wiseman, S.A., Lawrence, S.J., Tran, T.N., Robinson, M.S., Sato, H., Hawke, B.R., Scholten, F., Oberst, J., Hiesinger, H. and Van Der Bogert, C.H., (2011). Non-mare silicic volcanism on the lunar farside at Compton–Belkovich. Nature Geoscience, 4(8), 566.

Joy, K. H., and Arai, T. (2013). Lunar meteorites: new insights into the geological history of the Moon. *Astronomy and Geophysics*, *54*(4), 4-28.

Joy, K. H., Crawford, I. A., Russell, S. S., and Kearsley, A. T. (2010). Lunar meteorite regolith breccias: An in situ study of impact melt composition using LA-ICP-MS with implications for the composition of the lunar crust. *Meteoritics and Planetary Science*, *45*(6), 917-946.

Joy, K.H., Crawford, I. A., Huss, G. R., Nagashima, K., and Taylor, G. J. (2014). An unusual clast in lunar meteorite MacAlpine Hills 88105: A unique lunar sample or projectile debris? *Meteoritics and Planetary Science,* 49(4), 677-695.

Joy, K. H., Crawford, I. A., Anand, M., Greenwood, R. C., Franchi, I. A., and Russell, S. S. (2008). The petrology and geochemistry of Miller Range 05035: A new lunar gabbroic meteorite. *Geochimica et Cosmochimica Acta*, *72*(15), 3822-3844.

Joy, K. H., Burgess, R., Hinton, R., Fernandes, V. A., Crawford, I. A., Kearsley, A. T., and Irving, A. J. (2011). Petrogenesis and chronology of lunar meteorite Northwest Africa 4472: A KREEPy regolith breccia from the Moon. *Geochimica et Cosmochimica Acta*, *75*(9), 2420-2452.

Joy, K.H., Nemchin, A., Grange, M., Lapen, T.J., Peslier, A.H., Ross, D.K., Zolensky, M.E. and Kring, D.A. (2014). Petrography, geochronology and source terrain characteristics of lunar meteorites Dhofar 925, 961 and Sayh al Uhaymir 449. *Geochimica et Cosmochimica Acta*, *144*, 299-325.

Karner, J., Papike, J. J., and Shearer, C. K. (2003). Olivine from planetary basalts: Chemical signatures that indicate planetary parentage and those that record igneous setting and process. *American Mineralogist*, *88*(5-6), 806-816.

Karner, J., Papike, J. J., and Shearer, C. K. (2006). Comparative planetary mineralogy: Pyroxene major- and minor-element chemistry and partitioning of vanadium between pyroxene and melt in planetary basalts. *American Mineralogist*, *91*(10), 1574-1582.

Kirby, S. H., and Wegner, M. W. (1978). Dislocation substructure of mantle-derived olivine as revealed by selective chemical etching and transmission electron microscopy. *Physics and Chemistry of Minerals*, *3*(4), 309-330.

Kobayashi, S., Hasebe, N., Shibamura, E., Okudaira, O., Kobayashi, M., Yamashita, N., Karouji, Y., Hareyama, M., Hayatsu, K., d'Uston, C. and Maurice, S. (2010). Determining the absolute abundances of natural radioactive elements on the lunar surface by the Kaguya gamma-ray spectrometer. *Space science reviews*, *154*(1-4), 193-218.

Korotev, R. L. (2005). Lunar geochemistry as told by lunar meteorites. *Chemie der Erde-Geochemistry*, *65*(4), 297-346.

Korotev, R. L. (2012). Lunar meteorites from Oman. *Meteoritics and Planetary Science*, *47*(8), 1365-1402.

Korotev, R.L. (2019). *Meteorite fusion crust*. Retrieved from http://meteorites.wustl.edu/id/fusioncrust.htm

Korotev R. L. and Irving A. J. (2014) Keeping up with the lunar meteorites - 2014. *45th Lunar and Planetary Science Conference*, 1405.

Korotev R. L. and Irving A. J. (2015) Keeping up with the lunar meteorites - 2015. *46th Lunar and Planetary Science Conference*, 1942.

Korotev R. L. and Irving A. J. (2016) Not quite keeping up with the lunar meteorites – 2016. *47th Lunar and Planetary Science Conference*, 1358.

Korotev R. L. and Irving A. J. (2017) Still not keeping up with the lunar meteorites – 2017. *47th Lunar and Planetary Science Conference*, 1498.

Korotev, R. L., and Jolliff, B. L. (2001). The curious case of the lunar magnesian granulitic breccias. In *Lunar and Planetary Science Conference* (Vol. 32).

Korotev, R. L., Zeigler, R. A., and Jolliff, B. L. (2007). Do We Have a Meteorite from the South Pole-Aitken Basin of the Moon? *Meteoritics and Planetary Science Supplement*, *42*, 5257.

Korotev, R. L., Jolliff, B. L., Zeigler, R. A., Gillis, J. J., and Haskin, L. A. (2003). Feldspathic lunar meteorites and their implications for compositional remote sensing of the lunar surface and the composition of the lunar crust. *Geochimica et Cosmochimica Acta*, *67*(24), 4895-4923.

Krüger, T., Kenkmann, T., and Hergarten, S. (2017). Structural uplift and ejecta thickness of lunar mare craters: New insights into the formation of complex crater rims. Meteoritics and Planetary Science, 52(10), 2220-2240.

Lawrence, D. J., Hawke, B. R., Hagerty, J. J., Elphic, R. C., Feldman, W. C., Prettyman, T. H., and Vaniman, D. T. (2005). Evidence for a high-Th, evolved lithology on the Moon at Hansteen Alpha. *Geophysical Research Letters*, *32*(7).

Lawrence, D. J., Puetter, R. C., Elphic, R. C., Feldman, W. C., Hagerty, J. J., Prettyman, T. H., and Spudis, P. D. (2007). Global spatial deconvolution of Lunar Prospector Th abundances. Geophysical Research Letters, 34(3).

Lawrence, D.J., Feldman, W.C., Barraclough, B.L., Binder, A.B., Elphic, R.C., Maurice, S., Miller, M.C. and Prettyman, T.H., (2000). Thorium abundances on the lunar surface. Journal of Geophysical Research: Planets, 105(E8), 20307-20331.

Lawrence, D.J., Feldman, W.C., Elphic, R.C., Little, R.C., Prettyman, T.H., Maurice, S., Lucey, P.G. and Binder, A.B. (2002). Iron abundances on the lunar surface as measured by the Lunar Prospector gamma-ray and neutron spectrometers. *Journal of Geophysical Research: Planets*, *107*(E12), 13-1.

Lee, M. R., and Bland, P. A. (2004). Mechanisms of weathering of meteorites recovered from hot and cold deserts and the formation of phyllosilicates. *Geochimica et Cosmochimica Acta*, *68*(4), 893-916.

Li, Y., Dasgupta, R., and Tsuno, K. (2017). Carbon contents in reduced basalts at graphite saturation: Implications for the degassing of Mars, Mercury, and the Moon. *Journal of Geophysical Research: Planets*, *122*(6), 1300-1320.

Lilliefors, H. W. (1967). On the Kolmogorov-Smirnov test for normality with mean and variance unknown. *Journal of the American Statistical Association*, *62*: 318, 399-402.

Lin, Y., Shen, W., Liu, Y., Xu, L., Hofmann, B.A., Mao, Q., Tang, G.Q., Wu, F. and Li, X.H (2012). Very high-K KREEP-rich clasts in the impact melt breccia of the lunar meteorite SaU 169: New constraints on the last residue of the Lunar Magma Ocean. *Geochimica et Cosmochimica acta*, *85*, 19-40.

Lindstrom, M. M. and Lindstrom, D. J. (1986). Lunar granulites and their precursor anorthositic norites of the early lunar crust. *Journal of Geophysical Research: Solid Earth*, *91*(B4), 263-276.

Longhi, J. (1981, March). Modeling Equilibrium Partial Melting: Implications for Early Lunar Differentiation. In Lunar and Planetary Science Conference (Vol. 12, pp. 625-627).

Longhi, J. (1990). Silicate liquid immiscibility in isothermal crystallization experiments. In *Lunar and Planetary Science Conference Proceedings* (Vol. 20, pp. 13-24).

Longhi, J., (2003) .A new view of lunar ferroan anorthosites: Post magma ocean petrogenesis. *J.Geophys.Res*. 108. #5083.

Longhi, J., Ashwal, L.D. (1985). Two-stage models for lunar and terrestrial anorthosites: Petrogenesis without a magma ocean. In: *Proc. Lunar Planet. Sci. Conf.* 15th, pp. C571–C584.

Longhi, J. and Boudreau, A. E. (1979). Complex igneous processes and the formation of the primitive lunar crustal rocks. In Lunar and Planetary Science Conference Proceedings (Vol. 10, pp. 2085-2105).

Longhi, J., Durand, S. R., and Walker, D. (2010). The pattern of Ni and Co abundances in lunar olivines. Geochimica et Cosmochimica Acta, 74(2), 784-798.

Lucey, P. G. (2004). Mineral maps of the Moon. *Geophysical Research Letters*, *31*(8).

Lucey, P. G. and Cahill, J. T. S. (2009). The composition of the lunar surface relative to lunar samples. In Lunar and Planetary Science Conference (Vol. 40).

Lucey, P. G., Blewett, D. T., and Hawke, B. R. (1998). Mapping the FeO and TiO2 content of the lunar surface with multispectral imagery. *Journal of Geophysical Research: Planets*, *103*(E2), 3679-3699.

Lucey, P., Korotev, R.L., Gillis, J.J., Taylor, L.A., Lawrence, D., Campbell, B.A., Elphic, R., Feldman, B., Hood, L.L., Hunten, D. and Mendillo, M. (2006). Understanding the lunar surface and space-Moon interactions. *Reviews in mineralogy and geochemistry*, *60*(1), 83-219.

French, B. M., Heiken, G., Vaniman, D., and Schmitt, J. (1991). *Lunar sourcebook: A user's guide to the Moon*. CUP Archive.

McCallum, I. S. (1983, March). Formation of Mg-rich pristine rocks by crustal metasomatism. In Lunar and Planetary Science Conference (Vol. 14, pp. 473-474).

McCanta, M. C., Dyar, M. D., Rutherford, M. J., and Delaney, J. S. (2004). Iron partitioning between basaltic melts and clinopyroxene as a function of oxygen fugacity. *American Mineralogist*, *89*(11-12), 1685-1693.

McKay, D.S., Heiken, G., Basu, A., Blanford, G., Simon, S., Reedy, R., French, B.M. and Papike, J. (1991). The lunar regolith. *Lunar sourcebook*, 285-356.

Melosh, H. J. (1989). Impact cratering: A geologic process. Research supported by NASA. New York, Oxford University Press (Oxford Monographs on Geology and Geophysics, No. 11), 1989, 253 p., 11.

Melosh, H. J. (1990). Giant impacts and the thermal state of the early Earth. *Origin of the Earth*, *1*, 69-83.

Melosh, H. J., and Vickery, A. M. (1991). Melt droplet formation in energetic impact events. *Nature*, *350*(6318), 494.

Melosh, H. J., Kendall, J., Horgan, B., Johnson, B. C., Bowling, T., Lucey, P. G., and Taylor, G. J. (2017). South Pole–Aitken basin ejecta reveal the Moon's upper mantle. Geology, 45(12), 1063-1066.

Mercer, C. N., Treiman, A. H., and Joy, K. H. (2013). New lunar meteorite Northwest Africa 2996: A window into farside lithologies and petrogenesis. *Meteoritics and Planetary Science*, *48*(2), 289-315.

Morland, Z.S., Joy, K.D., Gholinia, A., and Degli-Alessandrini, G. (2019) Metal in lunar meteorite North West Africa 10989: Insights into survivability of impactor material delivered to the Moon. *50th Lunar and Planetary Science Conference*, 1275.

Moriarty, D. P., and Pieters, C. M. (2018). The Character of South Pole-Aitken Basin: Patterns of Surface and Subsurface Composition. Journal of Geophysical Research: Planets, 123(3), 729-747.

Morris, R. V. (1978). In situ reworking/gardening/of the lunar surface-Evidence from the Apollo cores. In Lunar and Planetary Science Conference Proceedings (Vol. 9, pp. 1801-1811).

Nagaoka, H., Takeda, H., Karouji, Y., Ohtake, M., Yamaguchi, A., Yoneda, S., and Hasebe, N. (2014). Implications for the origins of pure anorthosites found in the feldspathic lunar meteorites, Dhofar 489 group. *Earth, Planets and Space*, *66*(1), 115.

Neal, C. R., and Taylor, L. A. (1989). Metasomatic products of the lunar magma ocean: The role of KREEP dissemination. *Geochimica et Cosmochimica Acta*, *53*(2), 529-541.

Neal, C. R., and Taylor, L. A. (1992). Petrogenesis of mare basalts: A record of lunar volcanism. Geochimica et Cosmochimica Acta, 56(6), 2177-2211.

Neal, C. R., Taylor, L. A., and Lindstrom, M. M. (1988). Apollo 14 mare basalt petrogenesis-Assimilation of KREEP-like components by a fractionating magma. In Lunar and Planetary Science Conference Proceedings (Vol. 18, pp. 139-153).

Nicholis, M. G., and Rutherford, M. J. (2005). Pressure dependence of graphite–C–O phase equilibria and its role in lunar volcanism. *Lunar Planet. Sci. 36 (abstract 1726)*.

Norman, M. D. and Ryder, G. (1979). A summary of the petrology and geochemistry of pristine highlands rocks. In Lunar and Planetary Science Conference Proceedings (Vol. 10, pp. 531-559).

NRC, 2007. The Scientific Context for Exploration of the Moon (the 'SCEM Report'). National Research Council, National Academies Press, Washington DC.

Ohtake, M., Uemoto, K., Yokota, Y., Morota, T., Yamamoto, S., Nakamura, R., Haruyama, J., Iwata, T., Matsunaga, T. and Ishihara, Y. (2014). Geologic structure generated by large-impact basin formation observed at the South Pole-Aitken basin on the Moon. Geophysical Research Letters, 41(8), 2738-2745.

Ohtake, M., Matsunaga, T., Haruyama, J., Yokota, Y., Morota, T., Honda, C., Ogawa, Y., Torii, M., Miyamoto, H., Arai, T. and Hirata, N. (2009). The global distribution of pure anorthosite on the Moon. *Nature*, *461*(7261), 236.

Palme, H., Spettel, B., Jochum, K.P., Dreibus, G., Weber, H., Weckwerth, G., Wänke, H., Bischoff, A. and Stöffler, D. (1991). Lunar highland meteorites and the composition of the lunar crust. *Geochimica et Cosmochimica Acta*, *55*(11), 3105-3122.

Papike, J. J., and Cameron, M. (1976). Crystal chemistry of silicate minerals of geophysical interest. *Reviews of Geophysics*, *14*(1), 37-80.

Papike, J. J., and Vaniman, D. T. (1978). Luna 24 ferrobasalts and the mare basalt suite-Comparative chemistry, mineralogy, and petrology. In Mare Crisium: The View from Luna 24 (pp. 371-401).

Papike, J. J., Fowler, G. W., and Shearer, C. K. (1994). Orthopyroxene as a recorder of lunar crust evolution: An ion microprobe investigation of Mg-suite norites. American Mineralogist, 79(7-8), 796-800.

Papike, J. J., Ryder, G., and Shearer, C. K. (1998). Lunar materials. *Planetary Materials, Reviews in Mineralogy*, *36*, 5-1.

Papike, J. J., Karner, J. M., and Shearer, C. K. (2003). Determination of planetary basalt parentage: A simple technique using the electron microprobe. *American Mineralogist*, *88*(2-3), 469-472.

Papike, J. J., Fowler, G. W., Shearer, C. K., and Layne, G. D. (1996). Ion microprobe investigation of plagioclase and orthopyroxene from lunar Mg-suite norites: implications for calculating parental melt REE concentrations and for assessing postcrystallization REE redistribution. Geochimica et Cosmochimica Acta, 60(20), 3967-3978.

Parmentier, E. M., Zhong, S., and Zuber, M. T. (2002). Gravitational differentiation due to initial chemical stratification: origin of lunar asymmetry by the creep of dense KREEP?. Earth and Planetary Science Letters, 201(3-4), 473-480.

Pernet-Fisher, J., and Joy, K. (2016). The lunar highlands: old crust, new ideas. *Astronomy and Geophysics*, *57*, 26-30.

Petro, N. E. and Pieters, C. M. (2008). The lunar-wide effects of basin ejecta distribution on the early megaregolith. Meteoritics and Planetary Science, 43(9), 1517-1529.

Pieters, C. M., Tompkins, S., Head, J. W., and Hess, P. C. (1997). Mineralogy of the mafic anomaly in the South Pole-Aitken Basin: Implications for excavation of the lunar mantle. *Geophysical Research Letters*, *24*(15), 1903-1906.

Pieters, C. M., Head, J. W., Gaddis, L., Jolliff, B., and Duke, M. (2001). Rock types of South Pole-Aitken basin and extent of basaltic volcanism. *Journal of Geophysical Research: Planets*, *106*(E11), 28001-28022.

Prissel, T. C., Parman, S. W., and Head, J. W. (2016). Formation of the lunar highlands Mg-suite as told by spinel. American Mineralogist, 101(7), 1624-1635.

Prissel, T.C., Parman, S.W., Jackson, C.R.M., Rutherford, M.J., Hess, P.C., Head, J.W., Cheek, L., Dhingra, D. and Pieters, C.M. (2014). Pink Moon: The petrogenesis of pink spinel anorthosites and implications concerning Mg-suite magmatism. Earth and Planetary Science Letters, 403, 144-156.

Raedeke, L. D. and McCallum, I. S. (1980). A comparison of fractionation trends in the lunar crust and the Stillwater Complex. In Lunar Highlands Crust (pp. 133-153).

Rapp, J. F., and Draper, D. S. (2018). Fractional crystallization of the lunar magma ocean: Updating the dominant paradigm. *Meteoritics and Planetary Science*, *53*(7), 1432-1455.

Robinson, M.S., Ashley, J.W., Boyd, A.K., Wagner, R.V., Speyerer, E.J., Hawke, B.R., Hiesinger, H. and Van Der Bogert, C.H. (2012). Confirmation of sublunarean voids and thin layering in mare deposits. *Planetary and Space Science*, *69*(1), 18-27.

Roedder, E. and Weiblen, P. W. (1970). Silicate liquid immiscibility in lunar magmas, evidenced by melt inclusions in lunar rocks. *Science*, *167*(3918), 641-644.

Roedder, E. and Weiblen, P. W. (1971). Petrology of silicate melt inclusions, Apollo 11 and Apollo 12 and terrestrial equivalents. In *Lunar and Planetary Science Conference Proceedings* (Vol. 2, p. 507).

Roedder, E. and Weiblen, P. W. (1972). Petrographic features and petrologic significance of melt inclusions in Apollo 14 and 15 rocks. In *Lunar and Planetary Science Conference Proceedings* (Vol. 3, p. 251).

Rowan, L. R., and Ahrens, T. J. (1994). Observations of impact-induced molten metal-silicate partitioning. *Earth and Planetary Science Letters*, *122*(1-2), 71-88.

Ridley, W. I., Reid, A. M., Warner, J. L., and Brown, R. W. (1973). Apollo 15 green glasses. *Physics of the Earth and Planetary Interiors*, *7*(2), 133-136.

Rutherford M.J., Hess, P.C., Ryerson, F.J., Campbell, H.W., and Dick, P.A. (1976) The chemistry, origin and petrogenetic implications of lunar granite and monzonite. *Proceedings of the 7th Lunar and Planetary Science Conference*, p. 1723-1740.

Ruzicka, A., Grossman, J., Bouvier, A., and Agee, C. B. (2017). The Meteoritical Bulletin, No. 103. *Meteorit. Planet. Sci*, *52*, 1014.

Ruzicka, A., Grossman, J., Bouvier, A., Herd, C. D., and Agee, C. B. (2015). The meteoritical bulletin, No. 102. *Meteoritics and Planetary Science*, *50*(9), 1662-1662.

Ryder, G. (1991). Lunar ferroan anorthosites and mare basalt sources: The mixed connection. Geophysical Research Letters, 18(11), 2065-2068.

Rykart, R. (1995). Ouartz Monograph. The Peculiar Qualities of Rock Crystal, Smoky Quartz, Amethyst, Chalcedony, Agate, Opal and Other Varieties.

Sahu, B. K. (1977). Optimal sample size for thin-section size studies. Sedimentary Geology, 19, 185-196.

Scaillet, B. (2015). Planetary science: Carbon in the Moon. *Nature Geoscience*, *8*(10), 747.

Seddio, S. M., Jolliff, B. L., Korotev, R. L., and Zeigler, R. A. (2013). Petrology and geochemistry of lunar granite 12032, 366-19 and implications for lunar granite petrogenesis. *American Mineralogist*, *98*(10), 1697-1713.

Seddio, S. M., Korotev, R. L., Jolliff, B. L., and Wang, A. (2015). Silica polymorphs in lunar granite: Implications for granite petrogenesis on the Moon. *American Mineralogist*, *100*(7), 1533-1543.

Shearer, C. K., and Papike, J. J. (1999). INVITED REVIEW. Magmatic evolution of the Moon. *American Mineralogist*, *84*(10), 1469-1494.

Shearer, C. K., and Floss, C. (1999). Evolution of the Moon's mantle and crust as reflected in trace-element microbeam studies of lunar magmatism. Origin of the Earth and Moon, 339-359.

Shearer, C. K., and Papike, J. J. (2005). Early crustal building processes on the moon: Models for the petrogenesis of the magnesian suite. Geochimica et Cosmochimica Acta, 69(13), 3445-3461.

Shearer, C. K., Papike, J. J., and Spilde, M. N. (2001). Trace-element partitioning between immiscible lunar melts: An example from naturally occurring lunar melt inclusions. *American Mineralogist*, *86*(3), 238-246.

Shearer, C. K., Elardo, S. M., Petro, N. E., Borg, L. E., and McCubbin, F. M. (2015). Origin of the lunar highlands Mg-suite: An integrated petrology, geochemistry, chronology, and remote sensing perspective. *American Mineralogist*, *100*(1), 294-325.

Shearer, C.K., Hess, P.C., Wieczorek, M.A., Pritchard, M.E., Parmentier, E.M., Borg, L.E., Longhi, J., Elkins-Tanton, L.T., Neal, C.R., Antonenko, I. and Canup, R.M. (2006). Thermal and magmatic evolution of the Moon. *Reviews in Mineralogy and Geochemistry*, *60*(1), 365-518.

Shervais, J. W. and McGee, J. J. (1999). KREEP cumulates in the western lunar highlands: Ion and electron microprobe study of alkali-suite anorthosites and norites from Apollo 12 and 14. *American Mineralogist*, *84*(5-6), 806-820.

Smith, J.V. and Steele, I.M. (1984). Chemical substitution in silica polymorph. *Neues Jahrbuch fuer Mineralogie, Monatshefte*, p. 137-144.

Smith, J.V., Anderson, A.T., Newton, R.C., Olsen, E.J., Wyllie, P.J., Crewe, A.V., Isaacson, M.S., and Johnson, D. (1970). Petrologic history of the moon inferred from petrography, mineralogy and petrogenesis of Apollo 11 rocks. *Proceedings of the Apollo 11 Lunar Science Conference*, 1, 897–925.

Snyder, G. A., Taylor, L. A., and Halliday, A. N. (1995). Chronology and petrogenesis of the lunar highlands alkali suite: Cumulates from KREEP basalt crystallization. *Geochimica et Cosmochimica Acta*, *59*(6), 1185-1203.

Spudis, P. D. (1993). The Geology of Multi-Ring Basins, 264 pp.

Spudis, P. D., Gillis, J. J., and Reisse, R. A. (1994). Ancient multiring basins on the Moon revealed by Clementine laser altimetry. Science, 266(5192), 1848-1851.

Stegman, D. R., Jellinek, A. M., Zatman, S. A., Baumgardner, J. R., and Richards, M. A. (2003). An early lunar core dynamo driven by thermochemical mantle convection. Nature, 421(6919), 143.

Stelzner, T.H., Heide, K., Bischoff, A., Weber, D., Scherer, P., Schultz, L., Happel, M., Schrön, W., Neupert, U., Michel, R. and Clayton, R.N. (1999). An interdisciplinary study of weathering effects in ordinary chondrites from the Acfer region, Algeria. *Meteoritics and Planetary Science*, *34*(5), 787-794.

Stöffler, D. and Ryder, G. (2001). Stratigraphy and isotope ages of lunar geologic units: Chronological standard for the inner solar system. In *Chronology and evolution of Mars* (pp. 9-54). Springer, Dordrecht.

Stöffler, D., Ryder, G., Ivanov, B. A., Artemieva, N. A., Cintala, M. J., and Grieve, R. A. (2006). Cratering history and lunar chronology. *Reviews in Mineralogy and Geochemistry*, *60*(1), 519-596.

Szalay, J. R., and Horányi, M. (2016). Lunar meteoritic gardening rate derived from in situ LADEE/LDEX measurements. Geophysical Research Letters, 43(10), 4893-4898.

Takeda, H., Yamaguchi, A., Bogard, D.D., Karouji, Y., Ebihara, M., Ohtake, M., Saiki, K. and Arai, T. (2006). Magnesian anorthosites and a deep crustal rock from the farside crust of the moon. *Earth and Planetary Science Letters*, *247*(3-4), 171-184.

Taylor, G. J. (2009). Ancient lunar crust: Origin, composition, and implications. Elements, 5(1), 17-22.

Taylor, L.A. and Day, J.M.D. (2005) FeNi metal grains in La Paz mare basalt meteorites and Apollo 12 basalts. *36th Lunar and Planetary Science Conference*, 1417.

Taylor, S. R. (1982). *Planetary science: A lunar perspective* (Vol. 3303). Houston: Lunar and Planetary Institute.

Taylor, S. R., and Jakes, P. (1974). The geochemical evolution of the Moon. In *Lunar and Planetary Science Conference Proceedings* (Vol. 5, pp. 1287-1305).

Taylor, S. R., and McLennan, S. (2009). *Planetary crusts: their composition, origin and evolution* (Vol. 10). Cambridge University Press.

Treiman, A. H., and Gross, J. (2013). Basalt Related to Lunar Mg-Suite Plutonic Rocks: A Fragment in Lunar Meteorite ALH 81005. *Meteoritics and Planetary Science Supplement*, *76*.

Treiman, A. H., Maloy, A. K., Shearer, C. K., and Gross, J. (2010). Magnesian anorthositic granulites in lunar meteorites Allan Hills A81005 and Dhofar 309: Geochemistry and global significance. *Meteoritics and Planetary Science*, *45*(2), 163-180.

Vaniman, D. T., and Papike, J. J. (1977). Very low TI/VLT/basalts-A new mare rock type from the Apollo 17 drill core. In Lunar and Planetary Science Conference Proceedings (Vol. 8, pp. 1443-1471).

Vaniman, D. T., Papike, J. J., and Schweitzer, E. L. (1978). The Apollo 16 drive tube 60009/60010. II-Petrology and major element partitioning among the regolith components. In *Lunar and Planetary Science Conference Proceedings* (Vol. 9, pp. 1827-1860).

Vaughan, W. M., and Head, J. W. (2014). Impact melt differentiation in the South Pole-Aitken basin: Some observations and speculations. Planetary and Space Science, 91, 101-106.

Velbel, M. A. (2009). Dissolution of olivine during natural weathering. *Geochimica et Cosmochimica Acta*, *73*(20), 6098-6113.

Wang, X. and Zhao, S. (2018). New insights into lithology distribution across the Moon. *Journal of Geophysical Research: Planets*, *122*(10), 2034-2052.

Warner, J. L., Simonds, C. H., and Phinney, W. C. (1976, March). Genetic distinction between anorthosites and Mg-rich plutonic rocks: new data from 76255. In *Lunar and Planetary Science Conference* (Vol. 7).

Warner, J. L., Phinney, W. C., Bickel, C. E., and Simonds, C. H. (1977). Feldspathic granulitic impactites and pre-final bombardment lunar evolution. In *Lunar and Planetary Science Conference Proceedings* (Vol. 8, pp. 2051-2066).

Warren, P. H. (1983). Al-Sm-Eu-Sr systematics of eucrites and Moon rocks: Implications for planetary bulk compositions. Geochimica et Cosmochimica Acta, 47(9), 1559-1571.

Warren, P. H. (1985). The magma ocean concept and lunar evolution. *Annual Review of Earth and Planetary Sciences*, *13*(1), 201-240.

Warren, P. H. (1986). Anorthosite assimilation and the origin of the Mg/Fe-related bimodality of pristine moon rocks: Support for the magmasphere hypothesis. Journal of Geophysical Research: Solid Earth, 91(B4), 331-343.

Warren, P. H. (1993). A concise compilation of petrologic information on possibly pristine nonmare Moon rocks. *American Mineralogist*, *78*(3-4), 360-376.

Warren, P. H. (1994). Lunar and martian meteorite delivery services. *Icarus*, *111*(2), 338-363.

Warren, P. H. (2012). Let's get real: not every lunar rock sample is big enough to be representative for every purpose. In *Second Conference on the Lunar Highlands Crust* (Vol. 1677, pp. 59-60).

Warren, P. H., and Wasson, J. T. (1977). Pristine nonmare rocks and the nature of the lunar crust. In *Lunar and Planetary Science Conference Proceedings* (Vol. 8, pp. 2215-2235).

Warren, P. H. and Wasson, J. T. (1980). Further foraging for pristine nonmare rocks-Correlations between geochemistry and longitude. In *Lunar and Planetary Science Conference Proceedings* (Vol. 11, pp. 431-470).

Warren, P. H., ULFF-MØLLER, F., and Kallemeyn, G. W. (2005). "New" lunar meteorites: Impact melt and regolith breccias and large-scale heterogeneities of the upper lunar crust. *Meteoritics and Planetary Science*, *40*(7), 989-1014.

Wenk, H. R., and Bulakh, A. (2003) Minerals: Their Constitution and Origin.

Wetzel, D. T., Hauri, E. H., Saal, A. E., and Rutherford, M. J. (2015). Carbon content and degassing history of the lunar volcanic glasses. *Nature Geoscience*, *8*(10), 755.

Wicks, F. J., and Whittaker, E. J. W. (1977). Serpentine textures and serpentinization. *The Canadian Mineralogist*, *15*(4), 459-488.

Wieczorek, M.A., Jolliff, B.L., Khan, A., Pritchard, M.E., Weiss, B.P., Williams, J.D., Hood, L.L., Righter, K., Neal, C.R., Shearer, C.K. and McCallum, I.S. (2006). New views of the moon. *Rev. Min. Geochem*, *60*, 221-364.

Wilhelms, D. E., John, F., and Trask, N. J. (1987). *The geologic history of the Moon* (No. 1348).

Wilson, M. J. (2004). Weathering of the primary rock-forming minerals: processes, products and rates. *Clay Minerals*, *39*(3), 233-266.

Wood, J. A. (1975). The nature and origin of Boulder 1, Station 2, Apollo 17. The moon, 14(3-4), 505-517.

Wood, J. A., Dickey Jr, J. S., Marvin, U. B., and Powell, B. N. (1970). Lunar anorthosites and a geophysical model of the moon. *Geochimica et Cosmochimica Acta Supplement*, *1*, 965.

Wu, Y., Xue, B., Zhao, B., Lucey, P., Chen, J., Xu, X., Li, C. and Ouyang, Z. (2012) Global estimates of lunar iron and titanium contents from the Chang'E-1 IIM data. *Journal of Geophysical Research: Planets*, *117*(E2).

Yamashita, N., Hasebe, N., Reedy, R.C., Kobayashi, S., Karouji, Y., Hareyama, M., Shibamura, E., Kobayashi, M.N., Okudaira, O., d'Uston, C. and Gasnault, O. (2010). Uranium on the Moon: Global distribution and U/Th ratio. *Geophysical Research Letters*, *37*(10).

Zeigler, R. A., Korotev, R. L., Jolliff, B. L., and Haskin, L. A. (2005). Petrography and geochemistry of the LaPaz Icefield basaltic lunar meteorite and source crater pairing with Northwest Africa 032. *Meteoritics and Planetary Science*, *40*(7), 1073-1101.

Zeigler, R. A., Korotev, R. L., Haskin, L. A., Jollif, B. L., and Gillis, J. J. (2006). Petrography and geochemistry of five new Apollo 16 mare basalts and evidence for post-basin deposition of basaltic material at the site. *Meteoritics and Planetary Science*, *41*(2), 263-284.

Zeng, X., Joy, K.H., Li, S., Pernet-Fisher, J.F., Li, X., Martin, D.J., Li, Y. and Wang, S. (2018). Multiple lithic clasts in lunar breccia Northwest Africa 7948 and implication for the lithologic components of lunar crust. *Meteoritics and Planetary Science*, *53*(5), 1030-1050.

Zhang, X., Zhu, M. H., and Bugiolacchi, R. (2019). Mafic minerals in the South Pole-Aitken basin. Journal of Geophysical Research: Planets.

Zhong, S., Parmentier, E. M., and Zuber, M. T. (2000). A dynamic origin for the global asymmetry of lunar mare basalts. Earth and Planetary Science Letters, 177(3-4), 131-140.

Table 1: Electron microprobe conditions for mapping and data collection.

Mineral type	Beam current (nA)	Beam diameter (μm)	Element	Count time (s)
Olivine and pyroxene	25	1	Mg, Fe, Si, Al, Ca, Na Mn, Ti, Ni, Cr, Co	20 40
Plagioclase, glass, and quartz	20	3	K, Na Ca, Al, Si Fe, Mg, Mn, Ti, Cr	10 20 40
Metal and sulfide	25	1	Fe, Ni, Mg, Mn, Al Cr, S, Ti, Co	20 40

Table 2: Nomenclature used to describe clasts in NWA 10291 and 11182.

Clast classification		Description
Lithic	Mafic	Igneous clasts containing anorthitic plagioclase, olivine, and pyroxene; can contain ilmenite
	Evolved	Clasts containing one or more of the following phases: high-K plagioclase, silica, apatite
	Symplectite	Intergrowth of fayalitic olivine and hedenbergitic pyroxene with a complementary silica-phase; can contain ilmenite
Impact-related	Impact melt breccia	Formed from impacted material that did not fully melt or mix, resulting in mineral and other impacted material fragments set in a glassy or microcrystalline groundmass of plagioclase, olivine, and pyroxene; can contain vesicles
	Recrystallized impact melt	Impacted material that fully melted and mixed; produces plagioclase laths with crystalline olivine and pyroxene; has a quenched texture
	Granulite	Ca-rich plagioclase groundmass with granulitic olivine and pyroxene inclusions; can contain small inclusions of ilmenite or Fe-Ni metal
Glass bead		Rounded and melted glassy material with vesicular texture
Mineral grains		Grains that contain >99% of one mineral – pyroxene, olivine, plagioclase, ilmenite, Fe-Ni metal, sulfide, or zircon

Table 3: Inventory of clasts measured in NWA 10291 and 11182.

Clast Inventory		NWA 10291	NWA 11182
Lithic	Mafic	11	13
	Evolved	3	-
	Symplectite	2	-
Impact-related	Impact melt breccia	13	2
	Recrystallized impact melt	7	9
	Granulite	1	14
Glass bead		1	-
Mineral grains	Plagioclase	3	13
	Pyroxene	11	10
	Olivine	1	5
	Metal	5	4
	Sulfide	4	-
	Ilmenite	1	-
	Silica	3	-
	Zircon	1	-
Total		66	70

Table 4: Average chemistry of olivine, plagioclase, and pyroxene in mafic clasts in NWA 10291.

NWA 10291 – lithic clasts

	Mafic						Evolved
	Anorthositic Norite	Olivine Gabbro	Olivine Norite	Peridotite	Troctolitic Anorthosite	Symplectite	Symplectite
	Clast 8	Clast 1A	Clast 15	Clast 20	Clast 33	Clast 19	Clast 21
Oxide wt%	Olivine (n=4)	Olivine (n=4)	Olivine (n=4)	Olivine (n=2)	Olivine (n=5)	Olivine (n=4)	Olivine (n=3)
SiO_2	36.53 ± 0.14	36.91 ± 0.09	36.47 ± 0.06	37.20 ± 0.12	35.41 ± 0.20	29.03 ± 0.14	29.71 ± 0.23
TiO_2	0.08 ± 0.02	0.04 ± 0.01	b.d.	b.d.	b.d.	0.73 ± 0.27	0.11 ± 0.03
Al_2O_3	0.09 ± 0.06	0.11 ± 0.12	0.05 ± 0.02	b.d.	b.d.	b.d.	b.d.
Cr_2O_3	b.d.	b.d.	b.d.	b.d.	b.d.	b.d.	b.d.
FeO	31.67 ± 0.28	31.43 ± 0.35	31.55 ± 0.20	31.58 ± 0.07	32.92 ± 0.18	67.45 ± 0.16	65.48 ± 0.87
MnO	0.30 ± 0.05	0.28 ± 0.03	0.31 ± 0.09	0.34 ± 0.04	b.d.	0.75 ± 0.01	0.73 ± 0.01
MgO	30.32 ± 0.14	30.82 ± 0.36	30.41 ± 0.28	31.25 ± 0.01	29.64 ± 0.12	1.01 ± 0.11	2.41 ± 0.10
NiO	b.d.	b.d.	b.d.	b.d.	0.42 ± 0.36	b.d.	b.d.
CaO	0.43 ± 0.19	0.18 ± 0.03	0.14 ± 0.02	b.d.	0.25 ± 0.01	0.34 ± 0.02	0.67 ± 0.17
CoO	b.d.	0.04 ± 0.01	0.05 ± 0.02	b.d.	0.07 ± 0.01	b.d.	b.d.
Na_2O	b.d.	b.d.	b.d.	b.d.	b.d.	b.d.	b.d.
K_2O	b.d.	b.d.	b.d.	b.d.	n.a.	n.a.	n.a.
SO_3	b.d.	b.d.	b.d.	b.d.	n.a.	n.a.	n.a.
Total	99.59	99.90	99.20	100.66	99.15	99.43	99.36
afu							
Si	1.004	1.005	1.005	1.005	0.986	0.983	0.994
Ti	0.002	0.001	-	-	-	0.019	0.003
Al	0.001	0.005	0.002	-	-	-	-
Cr	-	-	-	-	-	-	-
Fe	0.726	0.716	0.725	0.714	0.767	1.910	1.832
Mn	0.007	0.006	0.007	0.008	0.008	0.022	0.021
Mg	1.239	1.251	1.246	1.259	1.231	0.051	0.120
Ni	-	-	-	-	0.009	-	-
Ca	0.013	0.005	0.004	0.004	0.008	0.012	0.024
Co	-	0.001	0.001	0.001	0.001	-	-
Na	-	-	-	-	-	-	-
K	-	-	-	-	-	-	-
S	-	-	-	-	-	-	-
Total cation	2.995	2.991	2.993	2.993	3.012	2.999	3.002
Fo (Mg#)	63.054	63.612	63.205	63.816	61.609	2.600	6.152
Fa	36.946	36.388	36.795	36.184	38.391	97.400	93.848

Mg#=Fo=Mg/(Mg+Fe); Fa = Fe/(Mg+Fe); wt% = weight percent; afu = atoms per formula unit; b.d.=below detection; n.a.=not analyzed; Fo = forsterite; Fa = fayalite

NWA 10291 – lithic clasts

	Mafic							
	Anorthosite	Anorthositic Norite	Anorthositic Gabbro	Norite	Noritic Anorthosite	Olivine Gabbro	Olivine Norite	Pyroxenite
	Clast 9	Clast 8	Clast 12	Clast 10	Clast 20	Clast 1A	Clast 15	Clast 41
Oxide wt%	Plagioclase (n=5)	Plagioclase (n=5)	Plagioclase (n=7)	Plagioclase (n=4)	Plagioclase (n=5)	Plagioclase (n=5)	Plagioclase (n=3)	Plagioclase (n=3)
SiO_2	43.52 ± 0.08	43.25 ± 0.40	44.02 ± 0.26	46.52 ± 0.06	44.53 ± 0.17	45.68 ± 0.62	45.73 ± 0.17	45.14 ± 0.12
TiO_2	b.d.	b.d.	b.d.	0.04 ± 0.01	b.d.	0.04 ± 0.02	b.d.	b.d.
Al_2O_3	35.52 ± 0.09	35.57 ± 0.26	34.84 ± 0.23	32.96 ± 0.31	34.46 ± 0.25	34.06 ± 0.40	33.38 ± 0.26	35.11 ± 0.21
Cr_2O_3	b.d.	b.d.	b.d.	b.d.	b.d.	b.d.	b.d.	b.d.
FeO	0.13 ± 0.02	0.29 ± 0.01	0.28 ± 0.03	0.19 ± 0.03	0.68 ± 0.09	0.38 ± 0.04	0.42 ± 0.01	0.60 ± 0.03
MnO	b.d.	b.d.	b.d.	b.d.	b.d.	b.d.	b.d.	b.d.
MgO	0.07 ± 0.01	0.13 ± 0.09	0.09 ± 0.04	0.22 ± 0.13	0.11 ± 0.05	0.21 ± 0.03	0.25 ± 0.09	0.02 ± 0.01
NiO	b.d.	b.d.	b.d.	b.d.	b.d.	b.d.	b.d.	n.a.
CaO	19.93 ± 0.06	19.95 ± 0.25	19.36 ± 0.18	17.68 ± 0.27	19.32 ± 0.20	18.63 ± 0.34	18.32 ± 0.15	18.33 ± 0.12
CoO	b.d.	b.d.	b.d.	b.d.	b.d.	b.d.	b.d.	n.a.
Na_2O	0.41 ± 0.03	0.43 ± 0.15	0.80 ± 0.09	1.40 ± 0.06	0.70 ± 0.06	0.92 ± 0.07	1.10 ± 0.08	0.87 ± 0.09
K_2O	b.d.	b.d.	0.05 ± 0.01	0.07 ± 0.01	b.d.	0.14 ± 0.05	0.12 ± 0.02	0.05 ± 0.02
SO_3	b.d.	b.d.	b.d.	b.d.	b.d.	b.d.	b.d.	n.a.
Total	99.62	99.71	99.50	99.12	99.91	100.09	99.36	100.19
afu								
Si	2.026	2.015	2.052	2.161	2.069	2.109	2.127	2.082
Ti	-	-	-	0.001	-	0.001	-	-
Al	1.949	1.953	1.914	1.804	1.887	1.854	1.830	1.908
Cr	-	-	-	-	-	-	-	-
Fe	0.005	0.011	0.011	0.007	0.026	0.015	0.016	0.023
Mn	-	-	-	-	-	-	-	-
Mg	0.005	0.009	0.001	0.015	0.008	0.014	0.017	0.002
Ni	-	-	-	-	-	-	-	-
Ca	0.994	0.996	0.967	0.880	0.962	0.922	0.913	0.905
Co	-	-	-	-	-	-	-	-
Na	0.037	0.039	0.073	0.126	0.063	0.082	0.099	0.078
K	-	-	0.001	0.004	-	0.008	0.007	0.003
S	-	-	-	-	-	-	-	-
Total cation	5.018	5.027	5.028	5.001	5.019	5.008	5.011	5.004
An	96.329	96.197	92.753	87.119	93.659	90.996	89.582	91.758
Ab	3.610	3.729	6.962	12.492	6.138	8.156	9.694	7.917
Or	-	-	0.285	0.389	-	0.848	0.725	0.325

NWA 10291 – lithic clasts

	Symplectite	
	Clast 19	Clast 21
Oxide wt%	Plagioclase (n=2)	Plagioclase (n=1)
SiO_2	49.40 ± 0.38	43.88
TiO_2	0.03 ± 0.01	0.04
Al_2O_3	32.23 ± 0.43	34.61
Cr_2O_3	b.d.	b.d.
FeO	1.44 ± 0.06	1.98
MnO	b.d.	b.d.
MgO	0.04 ± 0.01	0.87
NiO	n.a.	n.a.
CaO	16.27 ± 0.29	18.31
CoO	n.a.	n.a.
Na_2O	1.32 ± 0.11	0.35
K_2O	0.25 ± 0.01	b.d.
SO_3	n.a.	n.a.
Total	101.00	100.11
afu		
Si	2.246	2.041
Ti	0.001	0.001
Al	1.727	1.898
Cr	-	-
Fe	0.055	0.077
Mn	-	-
Mg	0.002	0.060
Ni	-	-
Ca	0.793	0.912
Co	-	-
Na	0.117	0.031
K	0.015	-
S	-	-
Total cation	4.955	5.024
An	85.778	96.578
Ab	12.641	3.332
Or	1.582	-

An = Ca/(Ca+Na+K); Mg# = Mg/(Mg+Fe); Ab= Na/(Ca+Na+K); Or=K/(Ca+Na+K); wt% = weight percent; afu = atoms per formula unit; b.d.=below detection; n.a.=not analyzed; An = anorthite; Ab = albite; Or = orthoclase

NWA 10291 – lithic clasts

	Mafic							
	Anorthosite	Anorthositic Norite		Anorthositic Gabbro	Norite		Noritic Anorthosite	
	Clast 9	Clast 8	Clast 8	Clast 12	Clast 10	Clast 10	Clast 2	Clast 2
Oxide wt%	High-Ca Pyroxene (n=1)	Low- Ca Pyroxene (n=1)	High-Ca Pyroxene (n=3)	High-Ca Pyroxene (n=2)	Low-Ca Pyroxene (n=1)	High-Ca Plagioclase (n=5)	Low-Ca Pyroxene (n=2)	High-Ca Pyroxene (n=4)
SiO_2	48.81	52.50	51.23 ± 0.04	48.76 ± 0.68	53.12	52.28 ± 0.16	47.54 ± 1.04	49.46 ± 1.11
TiO_2	0.55	0.89	1.31 ± 0.07	0.78 ± 0.22	0.37	0.95 ± 0.05	0.52 ± 0.15	0.59 ± 0.17
Al_2O_3	1.00	1.38	2.43 ± 0.11	1.06 ± 0.08	1.23	1.30 ± 0.11	0.93 ± 0.09	1.25 ± 0.21
Cr_2O_3	0.30	0.25	0.46 ± 0.03	0.26 ± 0.17	0.52	0.50 ± 0.02	b.d.	b.d.
FeO	30.31	15.98	9.95 ± 0.16	26.26 ± 1.24	16.13	8.12 ± 0.23	36.98 ± 4.28	23.75 ± 4.96
MnO	0.40	0.22	0.14 ± 0.02	0.35 ± 0.04	0.21	0.14 ± 0.04	0.36 ± 0.04	0.40 ± 0.08
MgO	8.42	20.55	15.58 ± 0.08	7.64 ± 1.74	21.57	15.96 ± 0.14	5.67 ± 2.92	9.56 ± 2.92
NiO	b.d.	b.d.	b.d.	b.d.	b.d.	b.d.	b.d.	b.d.
CaO	9.87	8.23	18.46 ± 0.31	14.36 ± 1.18	6.24	20.39 ± 0.30	8.03 ± 0.01	14.63 ± 0.88
CoO	b.d.	b.d.	b.d.	b.d.	b.d.	b.d.	b.d.	b.d.
Na_2O	0.08	0.13	0.16 ± 0.04	0.08 ± 0.01	0.07	0.11 ± 0.02	b.d.	b.d.
K_2O	b.d.	b.d.	b.d.	b.d.	b.d.	b.d.	b.d.	b.d.
SO_3	b.d.	b.d.	b.d.	b.d.	b.d.	b.d.	b.d.	n.a.
Total	99.81	100.14	99.78	99.61	99.52	99.76	100.39	100.09
afu								
Si	1.959	1.942	1.910	1.950	1.965	1.942	1.949	1.943
Ti	0.017	0.025	0.037	0.024	0.010	0.027	0.016	0.018
Al	0.047	0.060	0.107	0.050	0.054	0.057	0.045	0.057
Cr	0.010	0.007	0.014	0.008	0.015	0.015	-	-
Fe	1.017	0.494	0.310	0.879	0.499	0.252	1.271	0.792
Mn	0.014	0.007	0.004	0.012	0.007	0.004	0.013	0.013
Mg	0.503	1.133	0.866	0.454	1.190	0.884	0.344	0.550
Ni	-	-	-	-	-	-	-	-
Ca	0.425	0.326	0.738	0.616	0.247	0.811	0.353	0.615
Co	-	-	-	-	-	-	-	-
Na	0.006	0.009	0.012	0.006	0.005	0.008	-	-
K	-	-	-	-	-	-	-	-
S	-	-	-	-	-	-	-	-
Total cation	3.999	4.004	3.999	4.001	3.994	4.000	4.002	4.004
Mg#	33.112	69.622	73.626	33.858	70.447	77.822	21.244	41.535
En	25.886	58.003	45.257	23.334	61.444	45.391	17.464	28.174
Fs	52.290	16.723	16.213	45.073	25.777	12.947	64.608	40.368
Wo	21.825	37.733	38.558	31.593	12.779	41.662	17.929	31.458

Mg# = Mg/(Mg+Fe); En = Mg/(Mg+Fe+Ca); Fs = Fe/(Mg+Fe+Ca); Wo = Ca/(Mg+Fe+Ca); wt% = weight percent; afu = atoms per formula unit; b.d.=below detection; n.a.=not analyzed; En = enstatite; Fs = ferrosilite; Wo = wollastonite

NWA 10291 – lithic clasts

Oxide wt%	Mafic						
	Olivine Gabbro	Olivine Norite		Peridotite		Pyroxenite	
	Clast 1A	Clast 15	Clast 15	Clast 20	Clast 20	Clast 41	Clast 41
	Low-Ca Pyroxene (n=5)	Low-Ca Pyroxene (n=4)	High-Ca Pyroxene (n=1)	Low-Ca Pyroxene (n=1)	High-Ca Pyroxene (n=2)	Low-Ca Plagioclase (n=3)	High-Ca Pyroxene (n=7)
SiO_2	53.12 ± 0.12	52.21 ± 0.23	52.20	52.92	52.41 ± 0.23	48.31 ± 0.35	49.63 ± 0.22
TiO_2	0.47 ± 0.07	0.42 ± 0.03	0.66	0.64	0.83 ± 0.04	0.35 ± 0.03	0.40 ± 0.01
Al_2O_3	1.02 ± 0.16	1.23 ± 0.25	1.42	1.24	1.77 ± 0.21	0.77 ± 0.09	1.04 ± 0.06
Cr_2O_3	0.47 ± 0.07	0.59 ± 0.05	0.48	0.49	0.62 ± 0.06	0.26 ± 0.04	0.39 ± 0.03
FeO	18.52 ± 0.57	17.88 ± 0.52	15.43	17.36	10.94 ± 0.90	33.44 ± 0.81	26.76 ± 1.25
MnO	0.36 ± 0.03	0.32 ± 0.04	0.25	0.37	0.16 ± 0.07	0.48 ± 0.02	0.40 ± 0.01
MgO	21.74 ± 0.36	20.91 ± 0.49	19.27	20.76	16.63 ± 0.60	9.80 ± 0.45	9.75 ± 0.22
NiO	b.d.	b.d.	b.d.	b.d.	b.d.	b.d.	b.d.
CaO	4.66 ± 0.88	5.61 ± 0.77	9.84	6.81	16.86 ± 1.33	b.d.	11.05 ± 0.87
CoO	b.d.	b.d.	b.d.	b.d.	b.d.	b.d.	b.d.
Na_2O	0.03 ± 0.01	b.d.	b.d.	0.06	0.04 ± 0.01	b.d.	b.d.
K_2O	b.d.	b.d.	b.d.	b.d.	b.d.	n.a.	b.d.
SO_3	b.d.	b.d.	b.d.	b.d.	b.d.	n.a.	b.d.
Total	100.43	99.22	99.58	100.67	100.28	99.59	99.50
afu							
Si	1.961	1.953	1.947	1.951	1.940	1.953	1.968
Ti	0.013	0.012	0.018	0.018	0.023	0.011	0.012
Al	0.044	0.054	0.0602	0.054	0.077	0.037	0.049
Cr	0.015	0.017	0.014	0.014	0.018	0.008	0.012
Fe	0.572	0.559	0.481	0.535	0.339	1.131	0.888
Mn	0.011	0.010	0.008	0.012	0.005	0.016	0.013
Mg	1.196	1.166	1.071	1.141	0.917	0.591	0.576
Ni	-	-	-	-	-	-	-
Ca	0.184	0.225	0.393	0.269	0.668	0.264	0.468
Co	-	-	-	-	-	-	-
Na	0.002	-	-	0.004	0.003	-	-
K	-	-	-	-	-	-	-
S	-	-	-	-	-	-	-
Total cation	3.998	4.000	3.996	3.998	3.991	4.014	3.991
Mg#	67.682	67.587	68.998	68.070	73.076	34.292	39.566
En	61.259	58.771	55.055	58.661	47.660	29.764	29.794
Fs	29.285	28.674	24.737	27.517	17.595	56.956	45.953
Wo	9.456	11.555	20.208	13.822	34.745	13.280	24.252

Mg# = Mg/(Mg+Fe); En = Mg/(Mg+Fe+Ca); Fs = Fe/(Mg+Fe+Ca); Wo = Ca/(Mg+Fe+Ca); wt% = weight percent; afu = atoms per formula unit; b.d.=below detection; n.a.=not analyzed; En = enstatite; Fs = ferrosilite; Wo = wollastonite

NWA 10291 – lithic clasts

	Mafic		
	Symplectite	Symplectite	
	Clast 19	Clast 21	Clast 15
Oxide wt%	High-Ca Pyroxene (n=5)	Low- Ca Pyroxene (n=1)	High-Ca Pyroxene (n=4)
SiO_2	47.22 ± 0.28	47.36	47.82 ± 0.24
TiO_2	0.80 ± 0.11	0.82	0.82 ± 0.03
Al_2O_3	0.96 ± 0.12	1.17	1.17 ± 0.04
Cr_2O_3	b.d.	0.18	0.14 ± 0.01
FeO	32.96 ± 1.11	35.14	31.84 ± 1.53
MnO	0.38 ± 0.04	0.48	0.50 ± 0.02
MgO	1.66 ± 0.21	6.26	3.00 ± 0.20
NiO	b.d.	b.d.	b.d.
CaO	15.59 ± 0.87	7.73	15.18 ± 1.67
CoO	b.d.	0.05	b.d.
Na_2O	b.d.	b.d.	b.d.
K_2O	n.a.	n.a.	n.a.
SO_3	n.a.	n.a.	n.a.
Total	99.64	98.65	100.56
afu			
Si	1.961	1.962	1.952
Ti	0.025	0.015	0.025
Al	0.047	0.048	0.056
Cr	0.001	0.006	0.005
Fe	1.145	1.218	1.088
Mn	0.013	0.017	0.017
Mg	0.103	0.387	0.182
Ni	-	-	-
Ca	0.694	0.343	0.663
Co	-	0.002	-
Na	-	-	-
K	-	-	-
S	-	-	-
Total cation	3.990	3.996	3.993
Mg#	8.242	24.101	14.357
En	5.304	19.856	9.434
Fs	58.951	62.528	56.296
Wo	35.745	17.616	34.270

Mg# = Mg/(Mg+Fe); En = Mg/(Mg+Fe+Ca); Fs = Fe/(Mg+Fe+Ca); Wo = Ca/(Mg+Fe+Ca); wt% = weight percent; afu = atoms per formula unit; b.d.=below detection; n.a.=not analyzed; En = enstatite; Fs = ferrosilite; Wo = wollastonite

NWA 10291

Oxide wt%	Glass Bead (n=3)	Mineral Grains Chromite (n=3)	Ilmenite (n=2)	Element wt%	Sulfide
SiO_2	45.57 ± 0.10	b.d.	b.d.	Si	b.d.
TiO_2	0.52 ± 0.04	8.77 ± 3.88	52.57 ± 0.16	Ti	b.d.
Al_2O_3	9.04 ± 0.04	10.12 ± 1.67	0.13 ± 0.02	Cr	b.d.
Cr_2O_3	0.50 ± 0.07	40.34 ± 3.88	0.07 ± 0.01	Fe	62.81 ± 0.35
FeO	19.51 ± 0.37	36.44 ± 3.13	43.87 ± 0.40	Mn	b.d.
MnO	0.31 ± 0.06	0.41 ± 0.01	b.d.	Mg	b.d.
MgO	14.44 ± 0.64	3.17 ± 0.22	1.76 ± 0.03	Ni	b.d.
NiO	b.d.	b.d.	b.d.	Ca	0.10 ± 0.01
CaO	9.50 ± 0.45	0.08 ± 0.02	0.17 ± 0.01	Co	b.d.
CoO	b.d.	b.d.	0.08 ± 0.01	P	b.d.
Na_2O	b.d.	0.06 ± 0.03	b.d.	S	36.76 ± 0.09
K_2O	b.d.	0.05 ± 0.01	b.d.		
SO_3	b.d.	b.d.	b.d.		
Total	99.58	99.54	99.07	Total	99.78
Mg#	-	13.45	-		
Cr#	-	82.20	-		
Ti#	-	17.80	51.88		

Mg# = Mg/(Mg+Fe); Cr# = Cr/(Cr+Ti); Ti# = Ti/(Ti+Cr); wt% = weight percent; afu = atoms per formula unit; b.d.=below detection; n.a.=not analyzed

Table 5: Average chemistry of pyroxene and plagioclase in representative clasts in NWA 11182.

NWA 11182 – lithic clasts

	Mafic					
	Anorthosite		Norite	Noritic Anorthosite	Peridotite	
	Clast 3	Clast 3	Clast 48	Clast 9	Clast 24	Clast 24
Oxide wt%	Low-Ca Pyroxene (n=1)	High-Ca Pyroxene (n=4)	Low-Ca Pyroxene (n=3)	Low-Ca Pyroxene (n=5)	Low-Ca Pyroxene (n=9)	High-Ca Pyroxene (n=2)
SiO_2	53.33	51.15 ± 0.21	53.37 ± 0.13	52.79 ± 0.22	53.62 ± 0.13	50.72 ± 0.31
TiO_2	0.38	1.22 ± 0.12	0.75 ± 0.07	0.23 ± 0.01	0.70 ± 0.02	1.22 ± 0.05
Al_2O_3	0.79	1.55 ± 0.18	1.91 ± 0.65	1.56 ± 0.08	1.59 ± 0.11	2.80 ± 0.38
Cr_2O_3	0.33	0.35 ± 0.03	0.24 ± 0.03	0.82 ± 0.03	0.47 ± 0.01	0.74 ± 0.01
FeO	22.76	17.18 ± 1.05	18.02 ± 0.35	16.96 ± 0.48	14.47 ± 0.19	7.79 ± 0.28
MnO	0.32	0.23 ± 0.04	0.36 ± 0.01	0.42 ± 0.05	0.26 ± 0.02	b.d.
MgO	20.25	12.92 ± 0.25	21.67 ± 0.04	20.66 ± 0.30	26.07 ± 0.28	16.23 ± 0.19
NiO	b.d.	b.d.	b.d.	b.d.	b.d.	b.d.
CaO	2.86	15.90 ± 0.98	4.20 ± 0.56	6.76 ± 0.65	2.64 ± 0.36	19.22 ± 0.77
CoO	b.d.	b.d.	b.d.	b.d.	b.d.	b.d.
Na_2O	b.d.	b.d.	b.d.	b.d.	b.d.	b.d.
K_2O	b.d.	b.d.	b.d.	b.d.	n.a.	b.d.
SO_3	b.d.	b.d.	b.d.	b.d.	n.a.	b.d.
Total	101.11	100.58	99.58	100.28	99.89	99.11
afu						
Si	1.979	1.939	1.955	1.952	1.941	1.890
Ti	0.011	0.035	0.021	0.006	0.019	0.034
Al	0.035	0.069	0.082	0.068	0.068	0.123
Cr	0.010	0.010	0.007	0.024	0.013	0.022
Fe	0.706	0.545	0.552	0.524	0.438	0.243
Mn	0.010	0.008	0.011	0.013	0.008	-
Mg	1.120	0.730	1.183	1.139	1.407	0.902
Ni	-	-	-	-	-	-
Ca	0.114	0.646	0.165	0.268	0.103	0.768
Co	-	-	-	-	-	-
Na	-	-	-	-	-	-
K	-	-	-	-	-	-
S	-	-	-	-	-	-
Total cation	3.990	3.986	3.981	3.996	4.000	3.995
Mg#	55.151	57.391	68.188	68.489	76.260	78.785
En	38.826	38.010	68.274	58.969	72.232	47.162
Fs	31.573	28.341	29.071	27.153	22.488	12.707
Wo	29.602	33.649	8.655	13.878	5.280	40.131

NWA 11182 – lithic clasts

	Mafic					
	Anorthosite	Norite	Noritic Anorthosite	Peridotite	Granulite	Mineral grain
	Clast 3	Clast 48	Clast 9	Clast 24	Clast 14	Clast 36
Oxide wt%	Plagioclase (n=5)	Plagioclase (n=3)	Plagioclase (n=5)	Plagioclase (n=5)	Altered olivine (n=3)	Altered olivine (n=5)
SiO_2	44.30 ± 0.24	44.39 ± 0.17	44.38 ± 0.09	44.24 ± 0.31	35.66 ± 0.93	41.30 ± 2.99
TiO_2	b.d.	b.d.	b.d.	0.05 ± 0.01	0.05 ± 0.02	0.16 ± 0.11
Al_2O_3	35.47 ± 0.21	35.93 ± 0.41	36.46 ± 0.13	35.13 ± 0.82	1.58 ± 0.21	0.76 ± 0.14
Cr_2O_3	b.d.	b.d.	b.d.	b.d.	0.07 ± 0.07	0.09 ± 0.06
FeO	0.22 ± 0.03	0.67 ± 0.25	0.15 ± 0.01	1.90 ± 0.51	33.34 ± 1.73	22.84 ± 2.90
MnO	b.d.	b.d.	b.d.	b.d.	0.07 ± 0.02	0.15 ± 0.03
MgO	b.d.	0.51 ± 0.30	0.08 ± 0.01	0.93 ± 0.60	18.96 ± 1.88	27.64 ± 2.50
NiO	b.d.	b.d.	b.d.	b.d.	0.03 ± 0.01	-
CaO	19.66 ± 0.15	18.95 ± 0.21	19.40 ± 0.11	18.04 ± 0.52	1.07 ± 0.06	1.65 ± 0.94
CoO	b.d.	b.d.	b.d.	b.d.	b.d.	-
Na_2O	0.43 ± 0.03	0.42 ± 0.02	0.44 ± 0.01	0.38 ± 0.04	0.16 ± 0.01	0.11 ± 0.03
K_2O	b.d.	b.d.	b.d.	0.10 ± 0.04	0.12 ± 0.02	0.17 ± 0.08
SO_3	b.d.	b.d.	b.d.	b.d.	b.d.	-
Total	100.22	101.00	100.97	100.84	91.10	94.89
afu						
Si	2.047	2.035	2.032	2.040	1.081	1.122
Ti	-	-	-	0.002	0.001	0.003
Al	1.931	1.941	1.967	1.909	0.057	0.024
Cr	-	-	-	-	0.002	0.002
Fe	0.008	0.026	0.006	0.073	0.848	0.531
Mn	-	-	-	-	0.002	0.003
Mg	-	0.035	0.006	0.064	0.854	1.124
Ni	-	-	-	-	0.001	-
Ca	0.973	0.931	0.952	0.892	0.035	0.046
Co	-	-	-	-	-	-
Na	0.038	0.037	0.039	0.034	0.009	0.006
K	-	-	-	0.006	0.004	0.006
S	-	-	-	-	-	-
Total cation	5.006	5.010	5.004	5.022	2.895	2.868
An/Mg#	96.142	96.031	95.983	95.686	50.152	68.366
Ab	3.785	3.844	3.927	3.657	-	-
Or	-	-	-	0.656	-	-

Mg# = Mg/(Mg+Fe); En = Mg/(Mg+Fe+Ca); Fs = Fe/(Mg+Fe+Ca); Wo = Ca/(Mg+Fe+Ca); An = Ca/(Ca+Na+K); Mg# = Mg/(Mg+Fe); Ab= Na/(Ca+Na+K); Or=K/(Ca+Na+K); wt% = weight percent; afu = atoms per formula unit; b.d.=below detection; n.a.=not analyzed

Table 6: Fe/Mn ratio of olivine in NWA 10291 and NWA 11182.

Fe/Mn ratio – olivine

	NWA 10291			NWA 11182		
	Ave	Min	Max	Ave	Min	Max
Lithic	107	94	119	80	80	80
Symplectite	89	89	89	-	-	-
Impact melt breccia	101	78	120	100	100	100
Recrystallized impact melt	124	91	231	96	93	99
Granulite	131	131	131	104	80	134
Mineral grain	105	60	189	119	92	155

Table 7: Fe/Mn ratio of pyroxene in NWA 10291 and NWA 11182.

Fe/Mn ratio – pyroxene

	NWA 10291			NWA 11182		
	Ave	Min	Max	Ave	Min	Max
Lithic	69	45	94	55	43	79
Symplectite	78	65	91	-	-	-
Impact melt breccia	58	45	74	55	54	57
Recrystallized impact melt	77	52	160	60	48	71
Granulite	62	62	62	62	44	89
Mineral grain	61	40	88	57	25	80

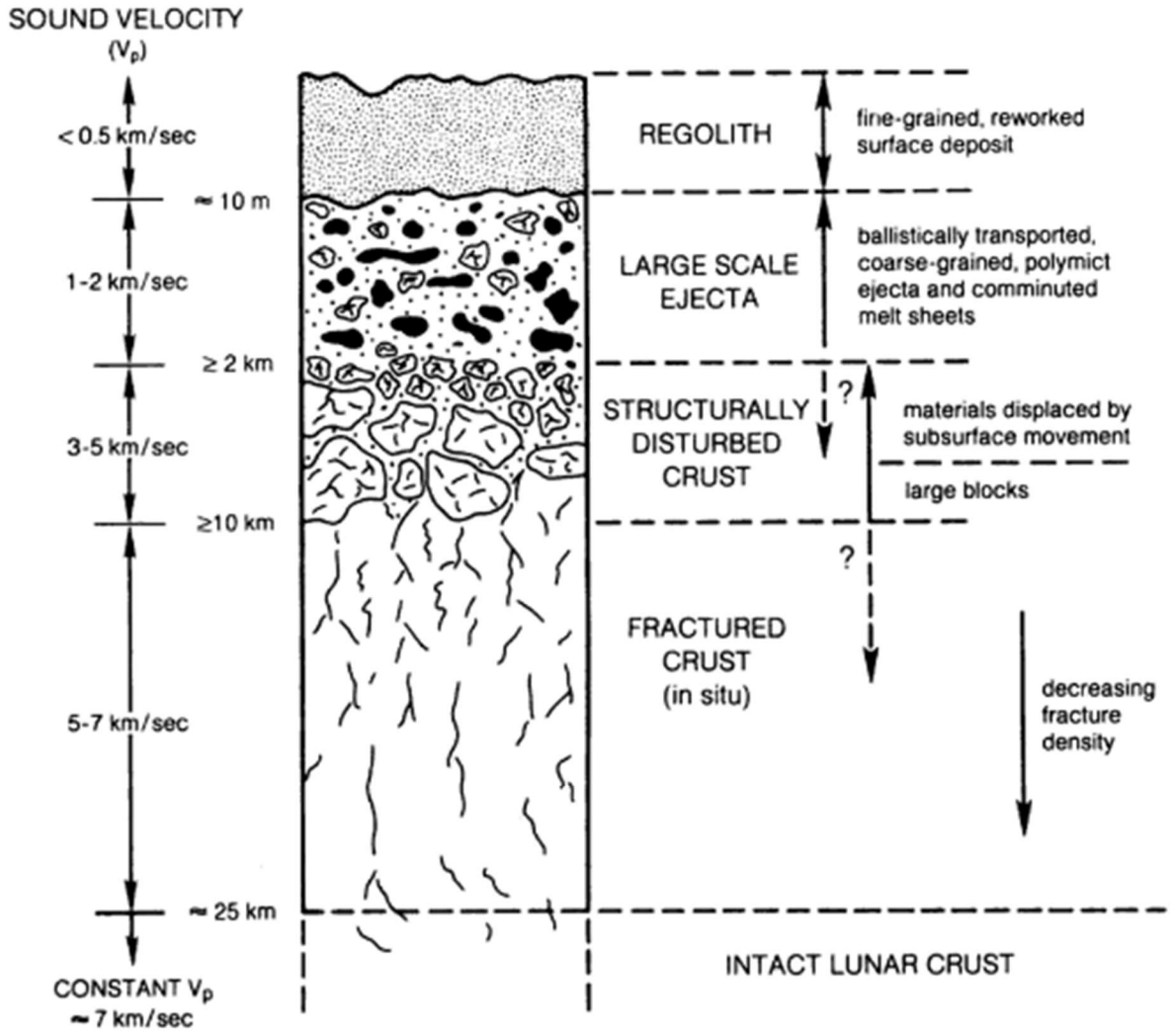

Figure 1: Structure of the lunar regolith.

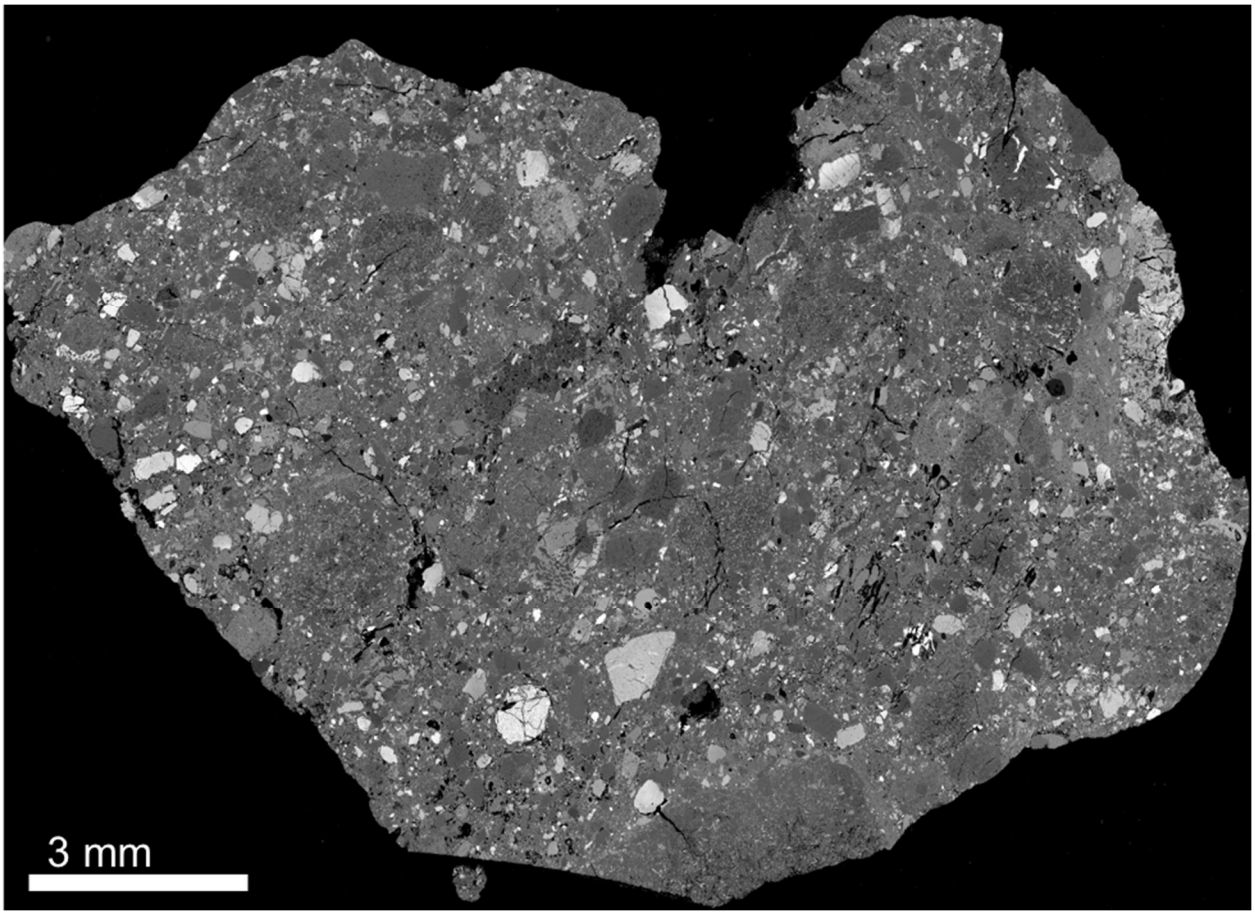

Figure 2: Full Back Scattered Electron (BSE) image of NWA 10291.

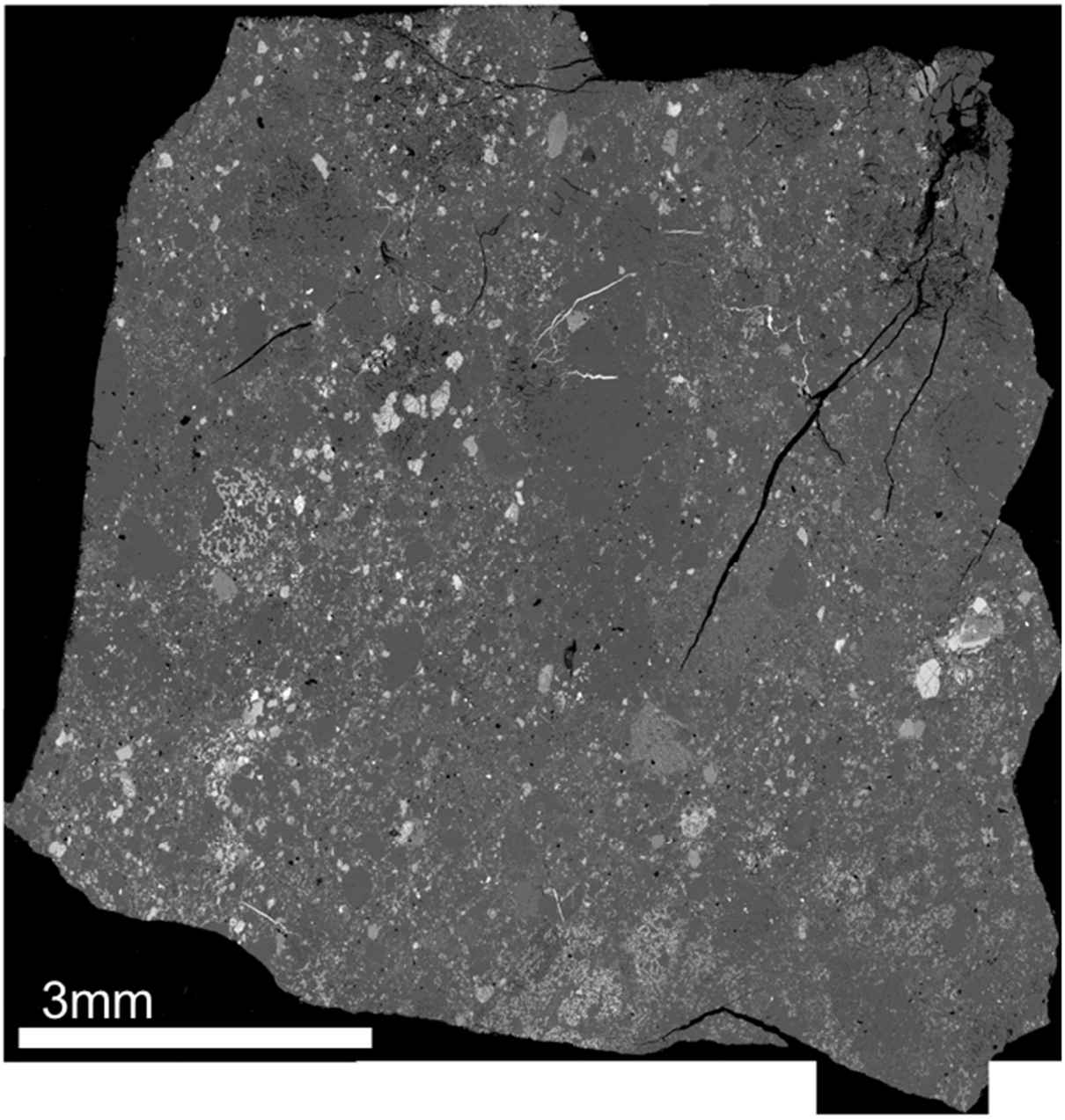

Figure 3: Full Back Scattered Electron (BSE) image of NWA 11182.

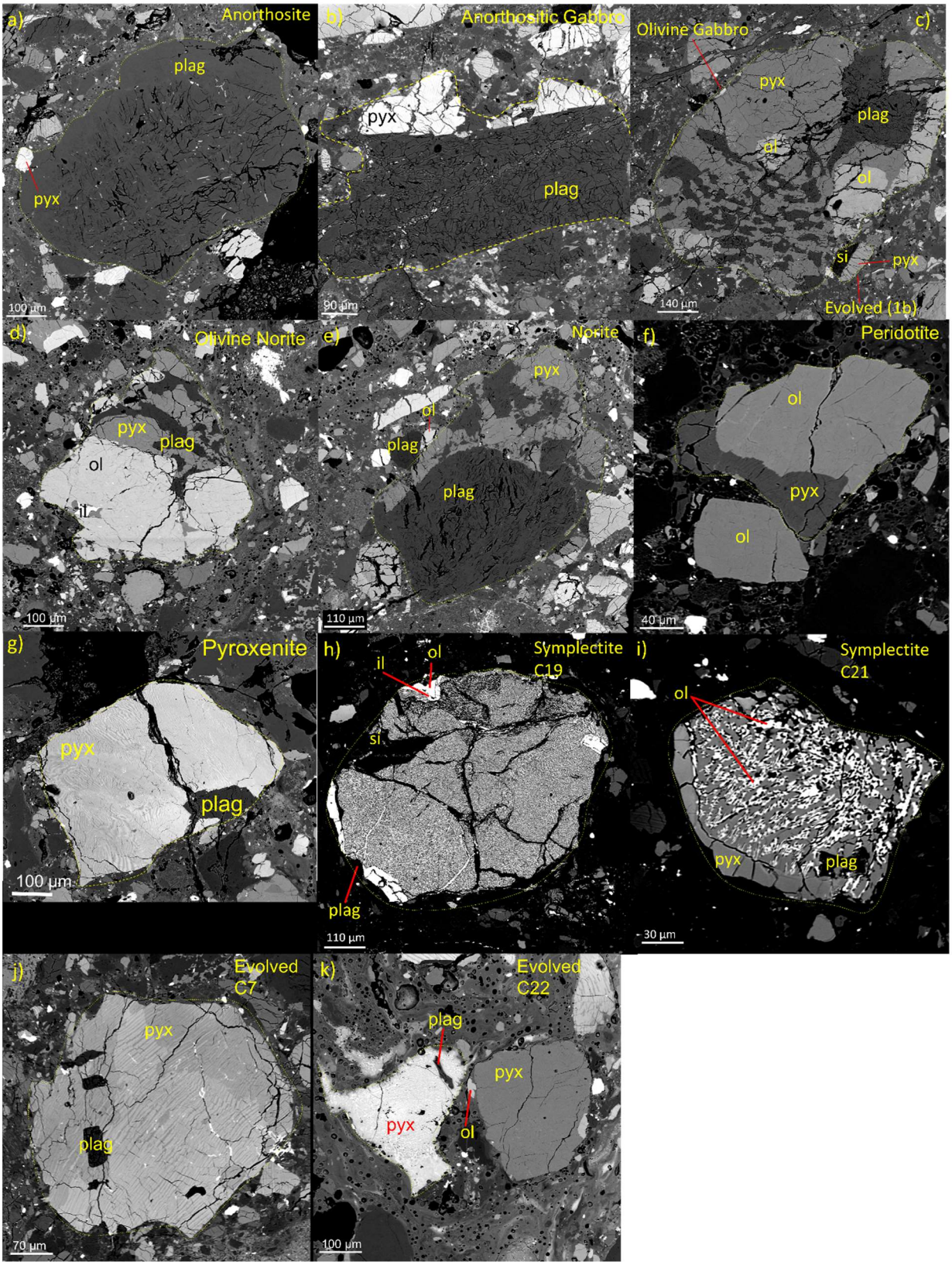

Figure 4: BSE images of representative lithic clasts in NWA 10291.

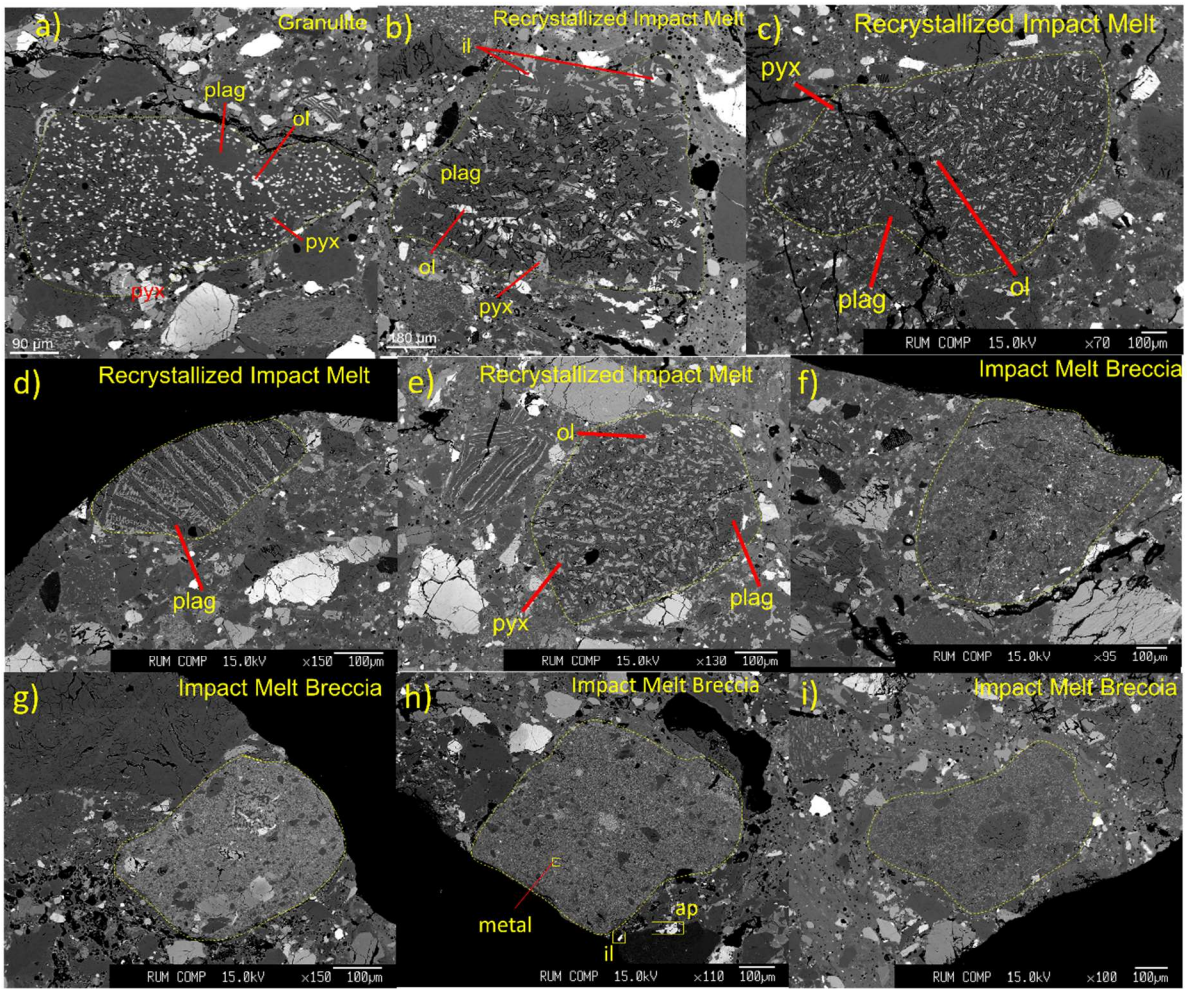

Figure 5: BSE images of representative impact-related clasts in NWA 10291.

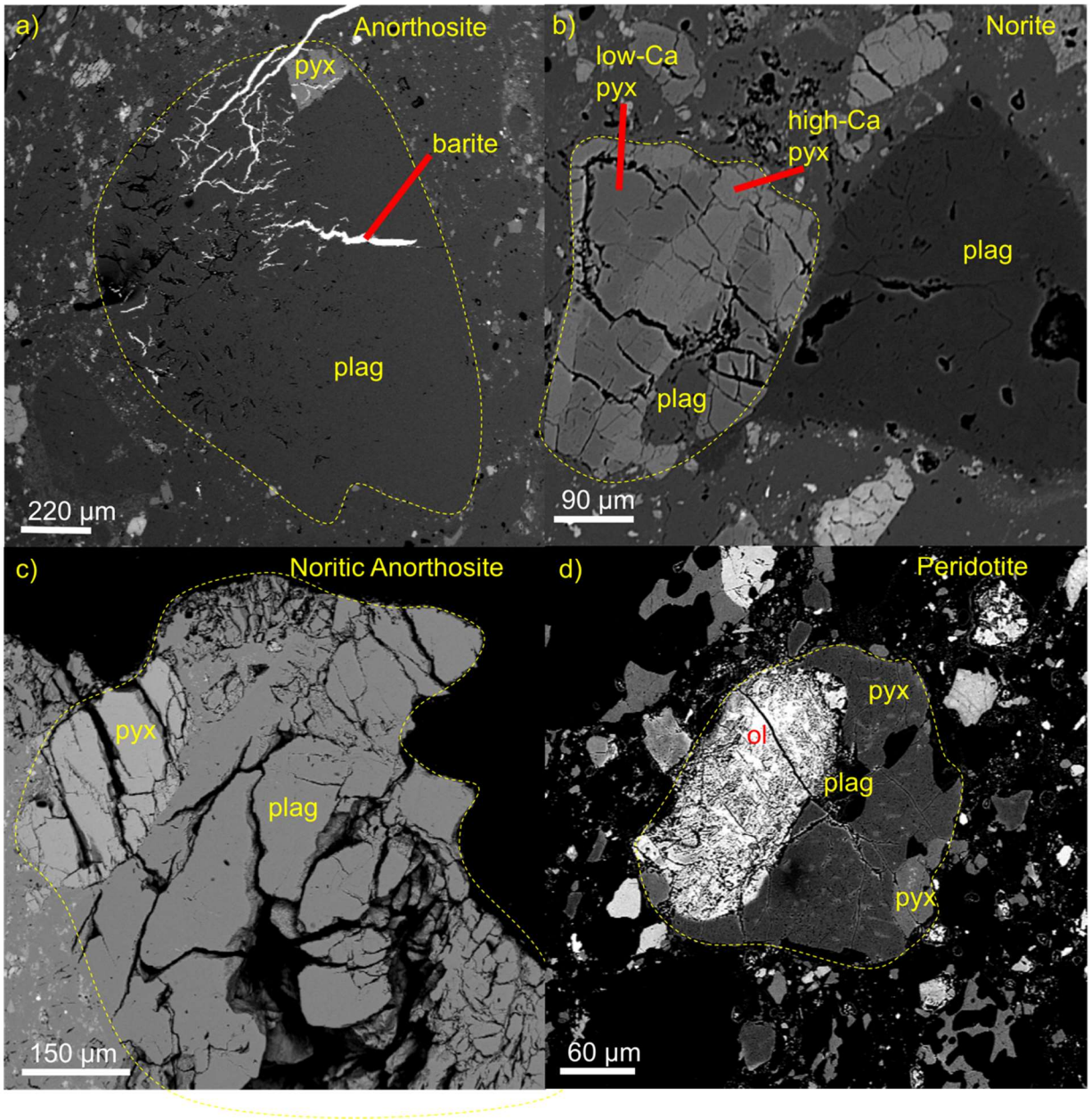

Figure 6: BSE images of representative lithic clasts in NWA 11182.

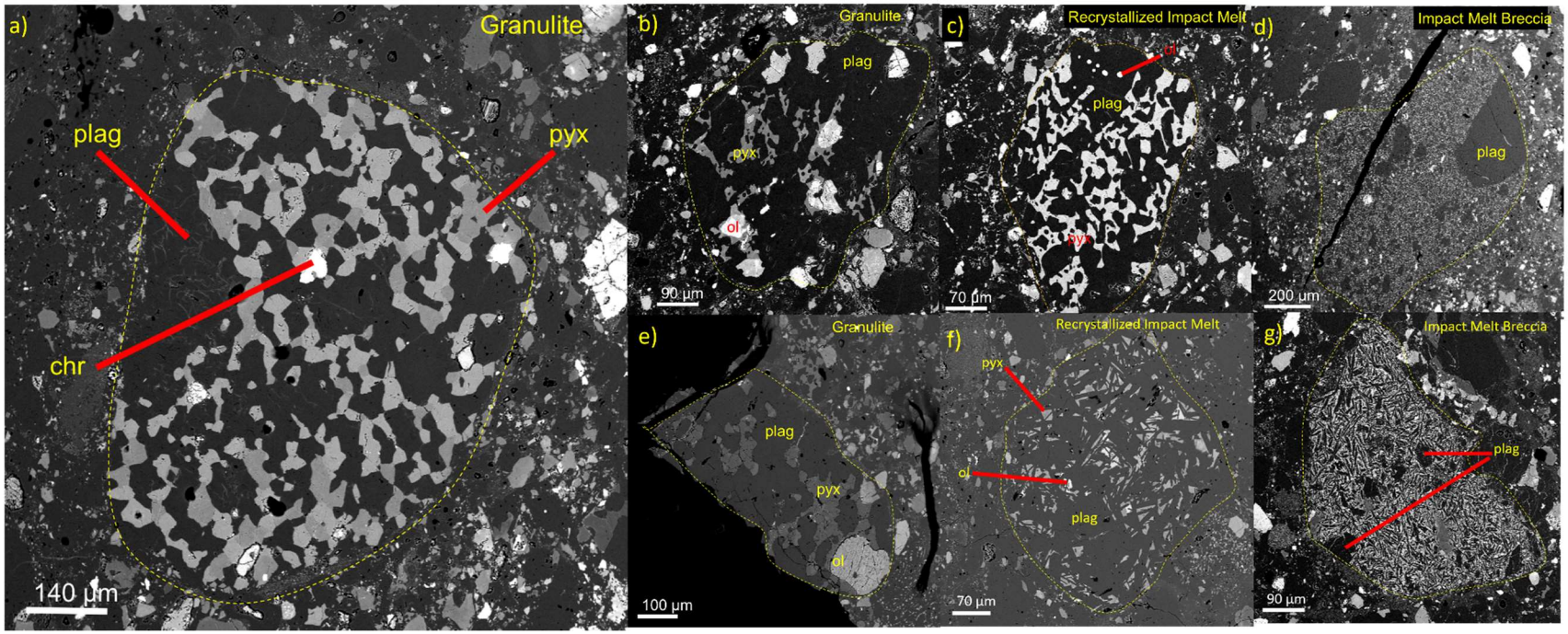

Figure 7: BSE images of representative impact-related clasts in NWA 11182.

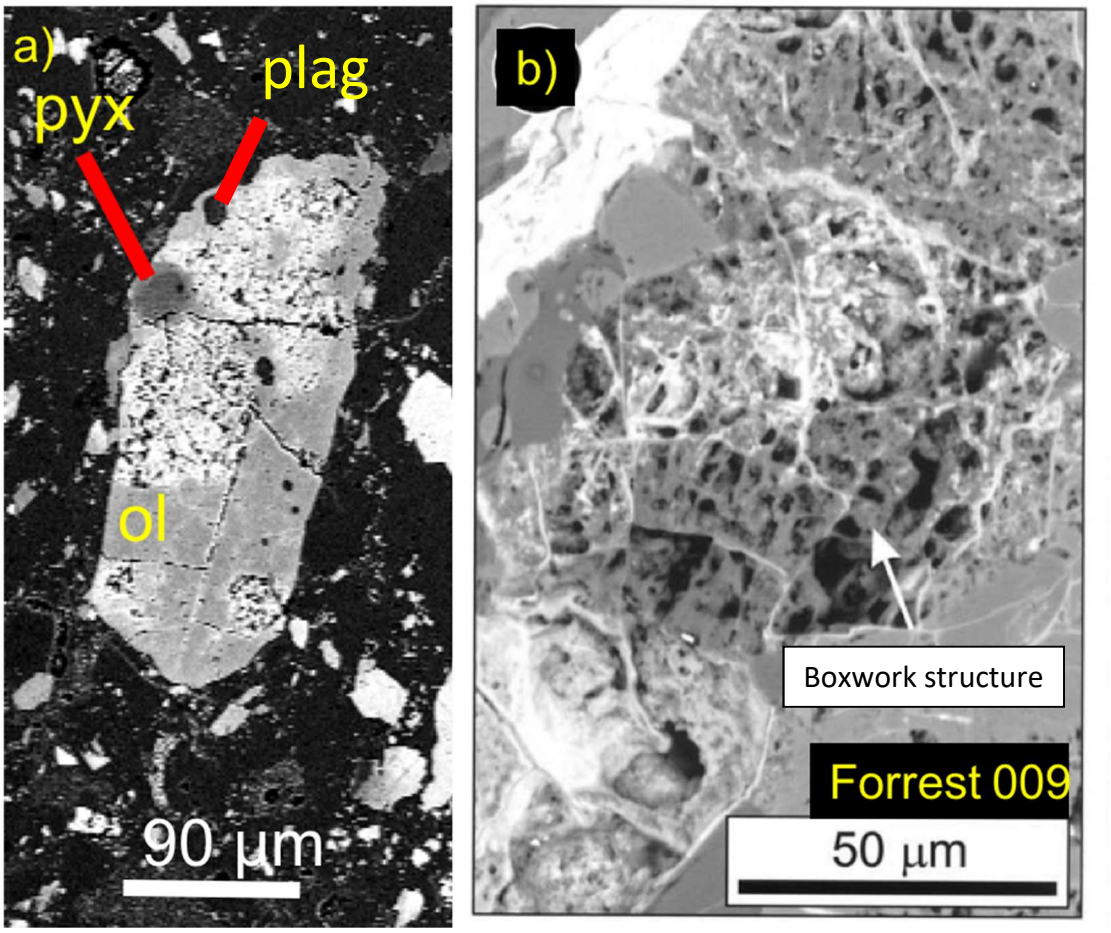

Figure 8: BSE images of altered olivine mineral grain in lunar NWA 11182 and L6 chondrite Forrest 009.

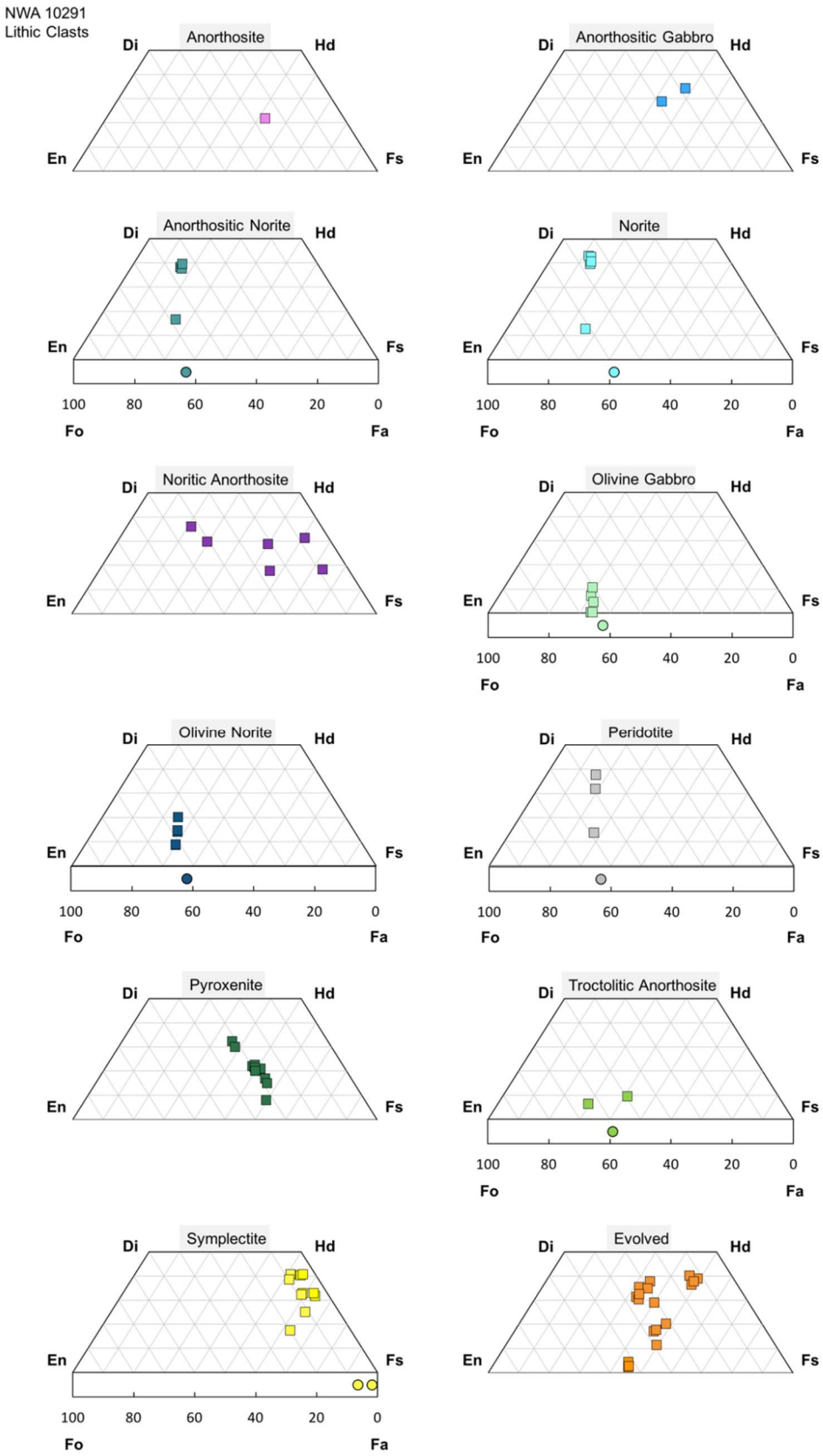

Figure 9: Mafic mineral chemistry of lithic clasts in NWA 10291.

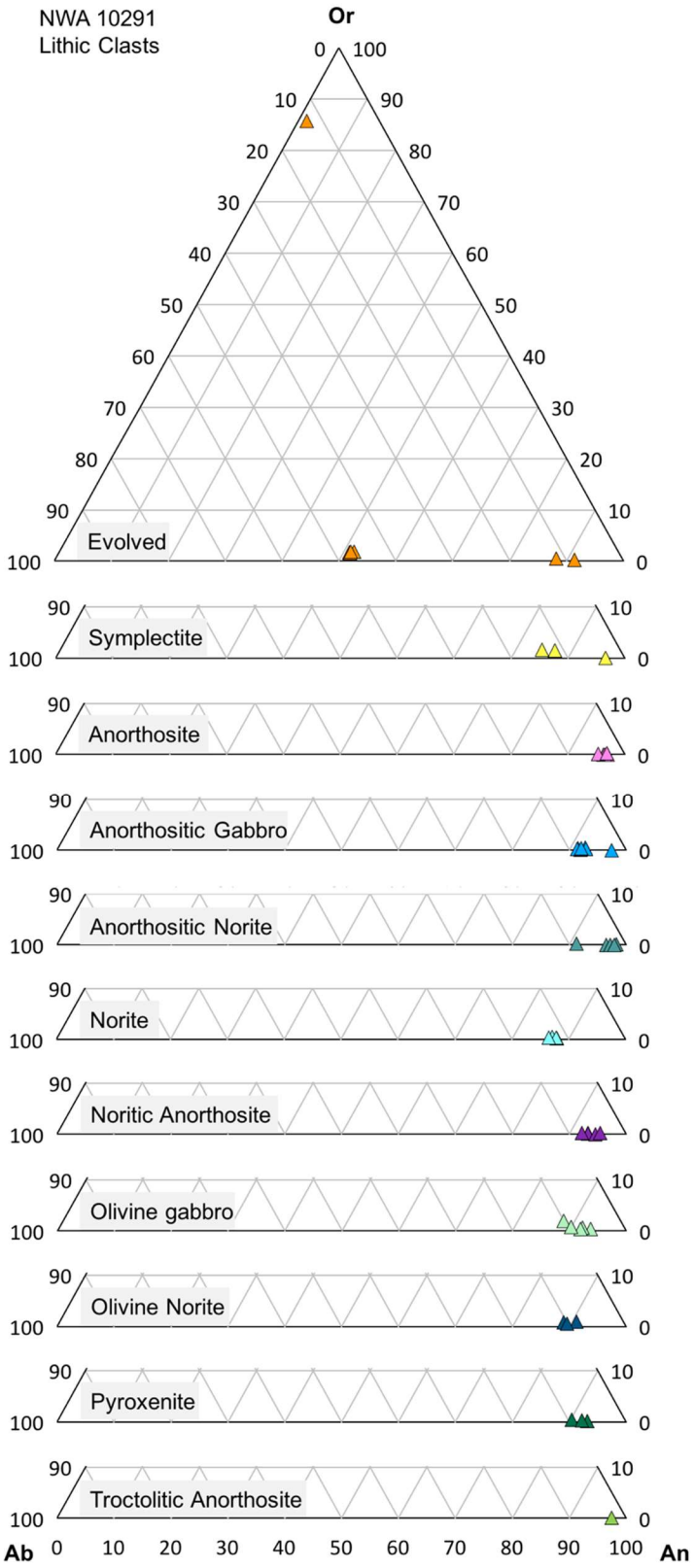

Figure 10: Plagioclase mineral chemistry of lithic clasts in NWA 10291.

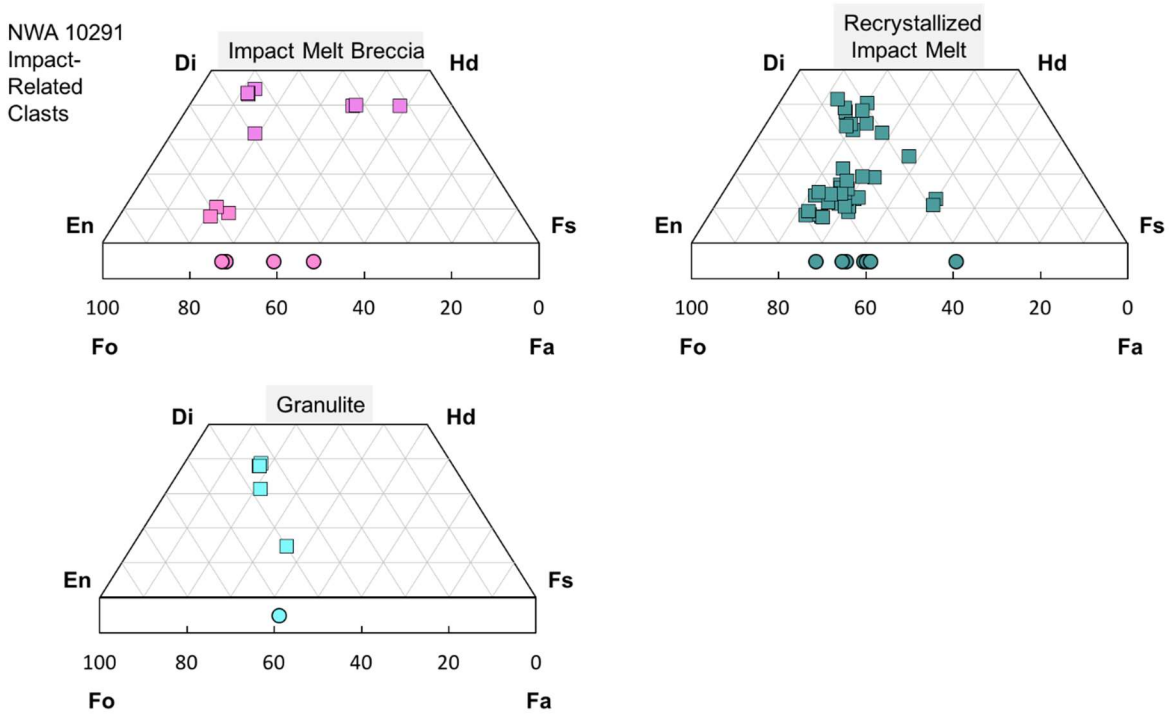

Figure 11: Mafic mineral chemistry of impact-related clasts in NWA 10291.

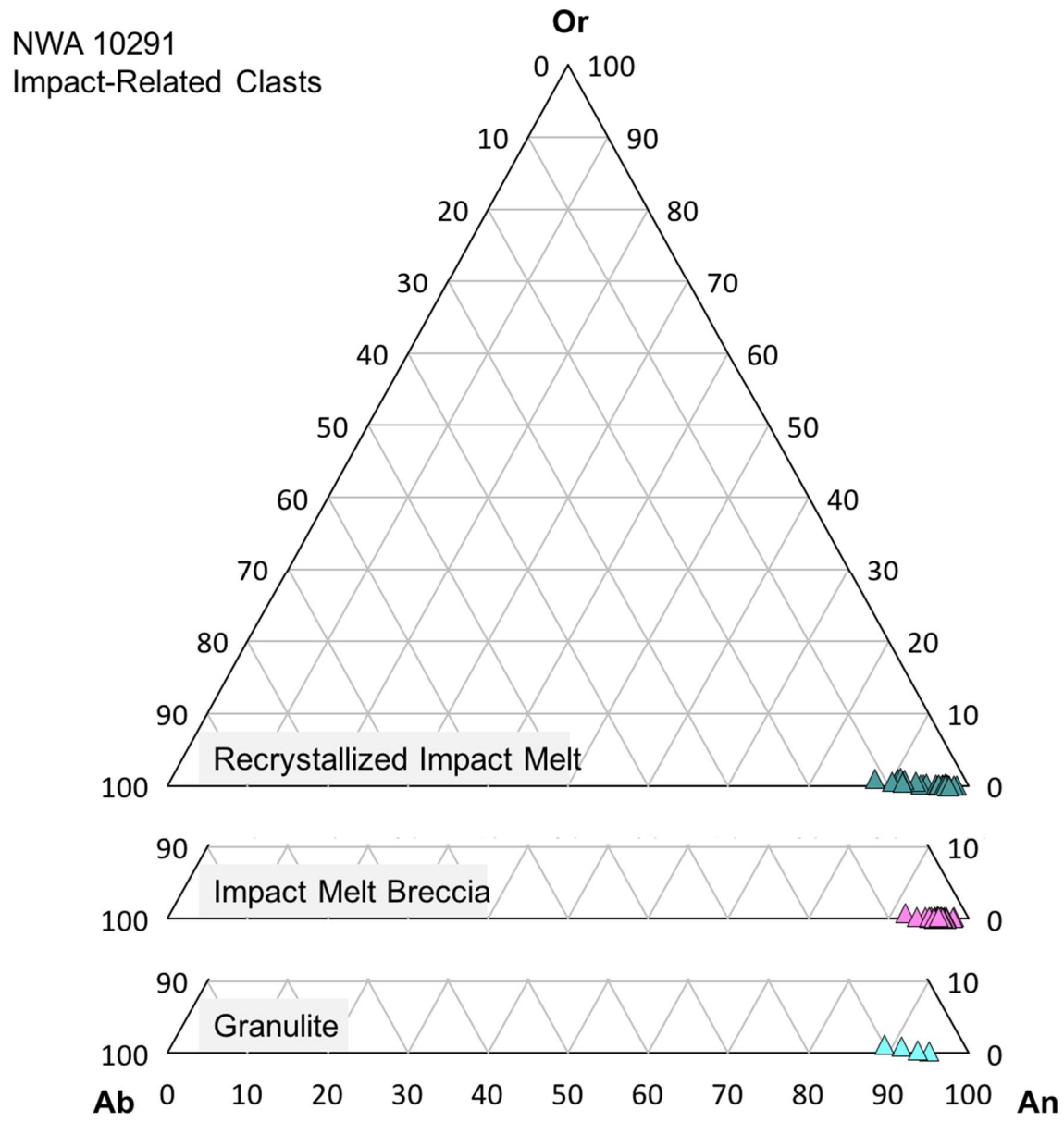

Figure 12: Plagioclase mineral chemistry of impact-related clasts in NWA 10291.

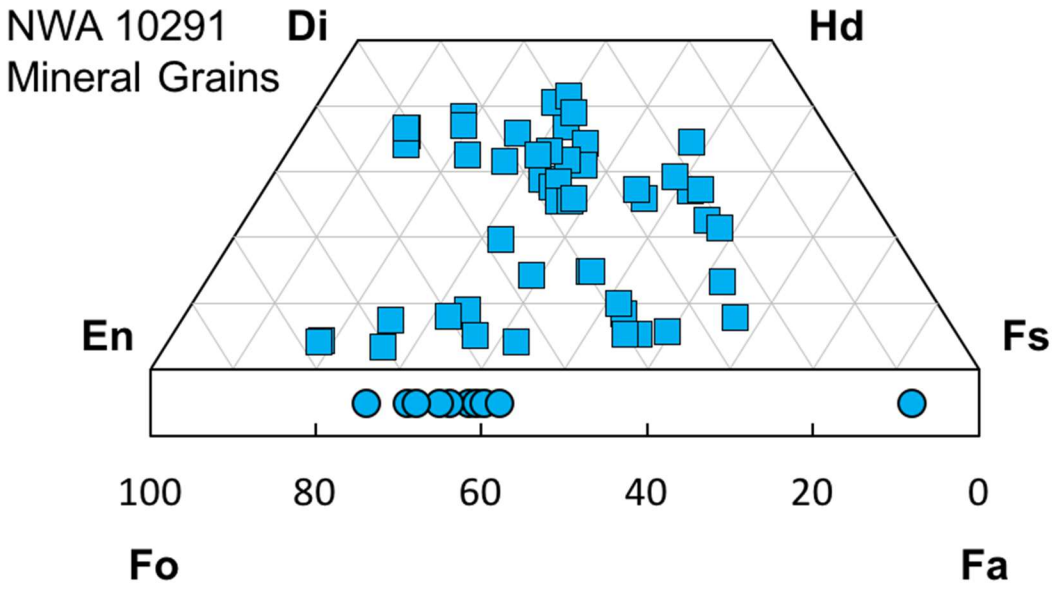

Figure 13: Mafic mineral chemistry of mineral grains in NWA 10291.

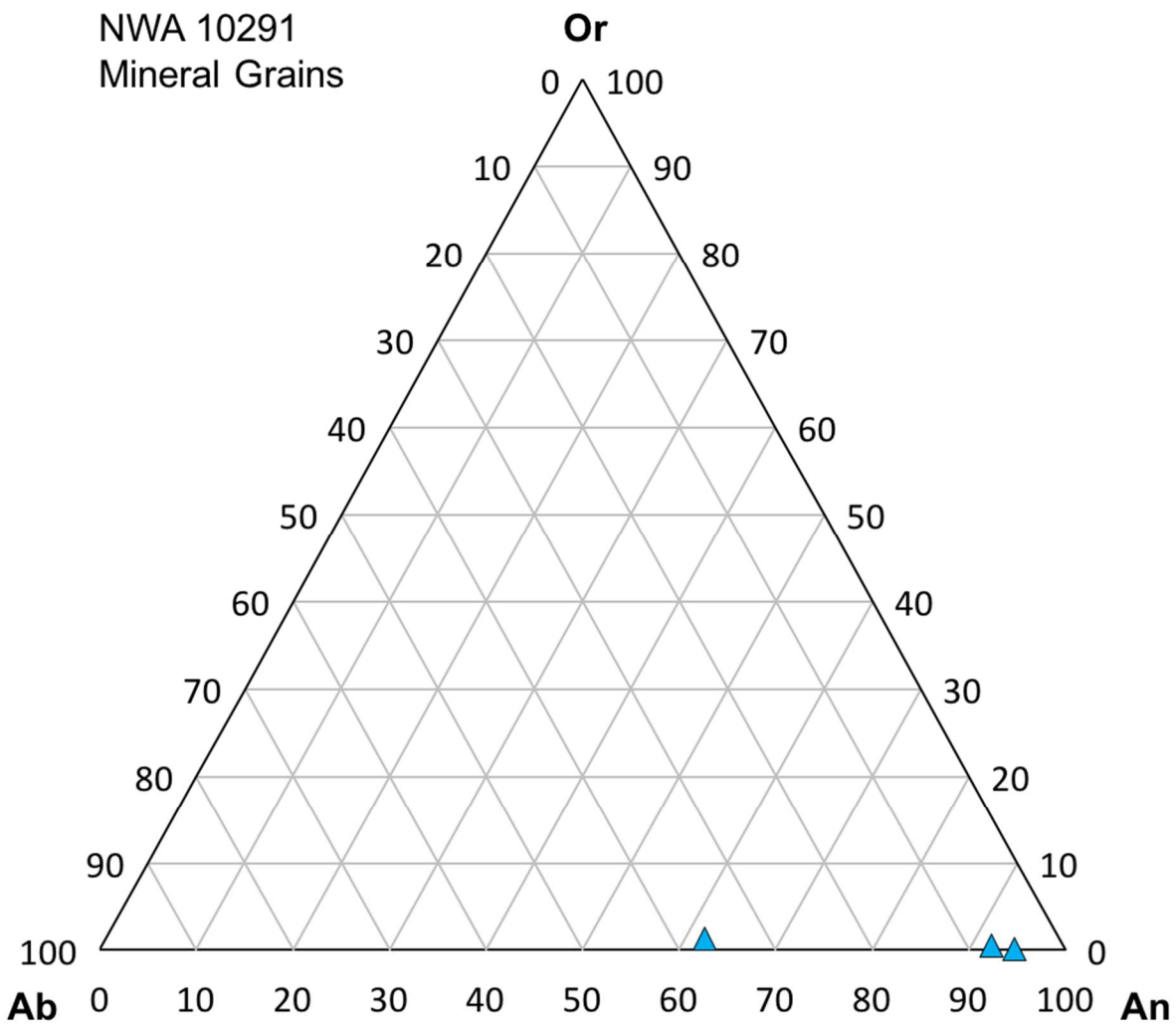

Figure 14: Plagioclase mineral chemistry of mineral grains in NWA 10291.

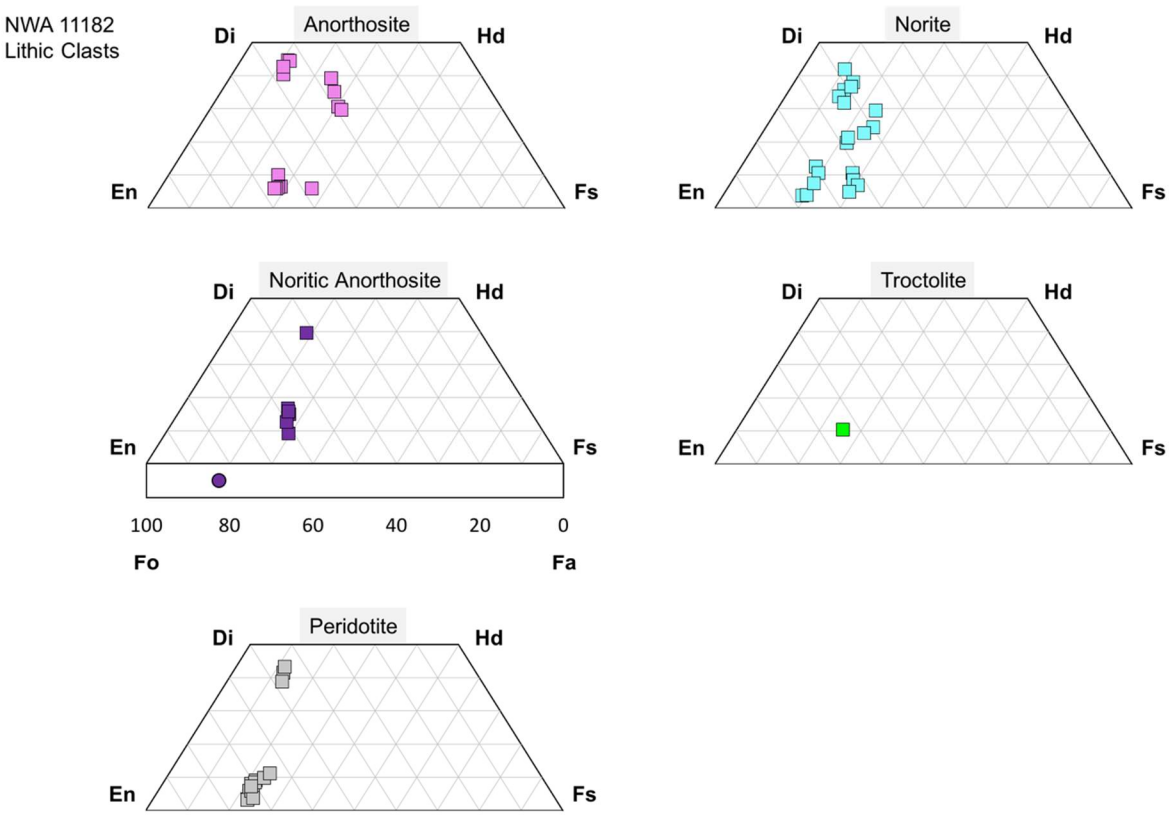

Figure 15: Mafic mineral chemistry of lithic clasts in NWA 11182.

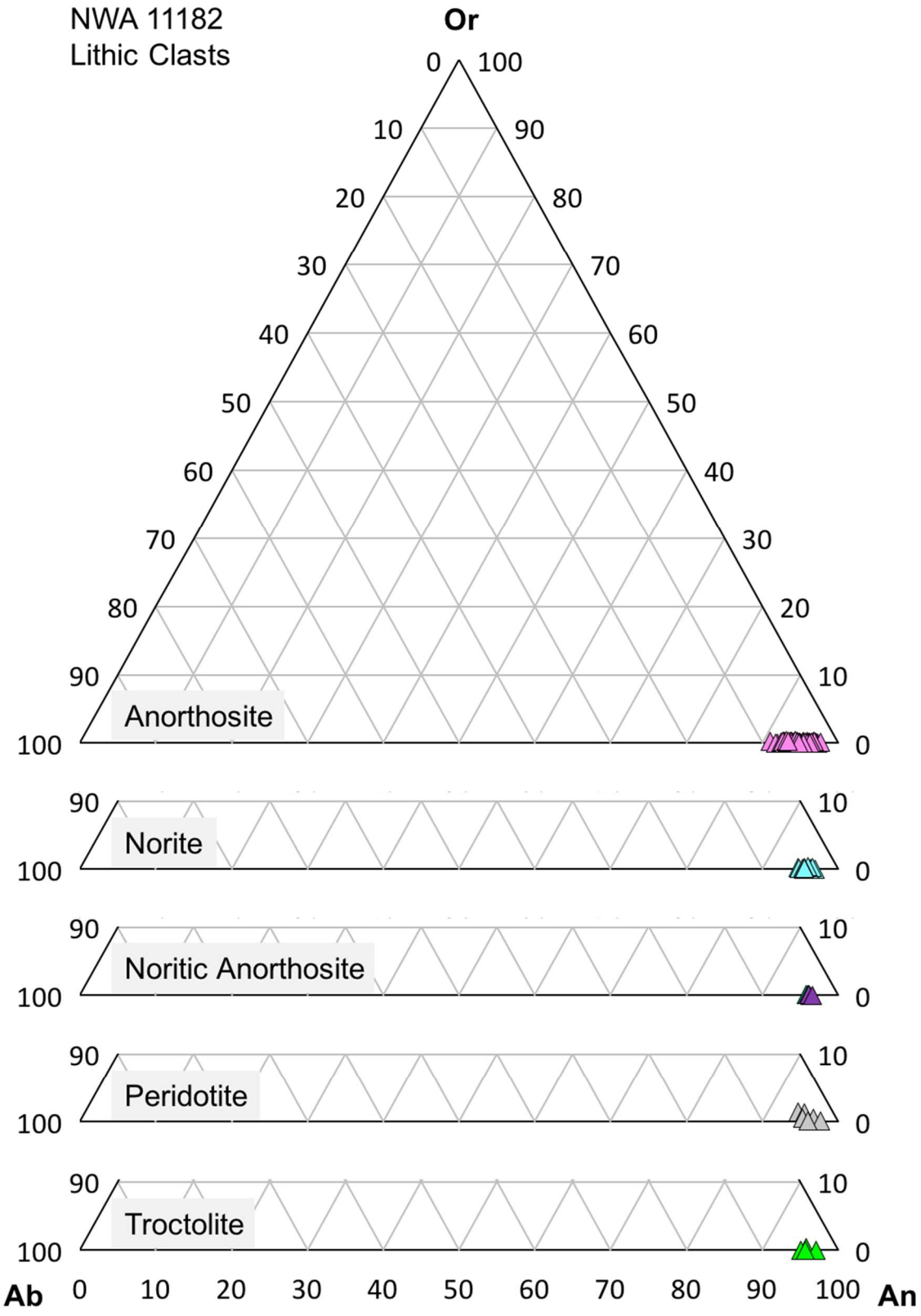

Figure 16: Plagioclase mineral chemistry of lithic clasts in NWA 11182.

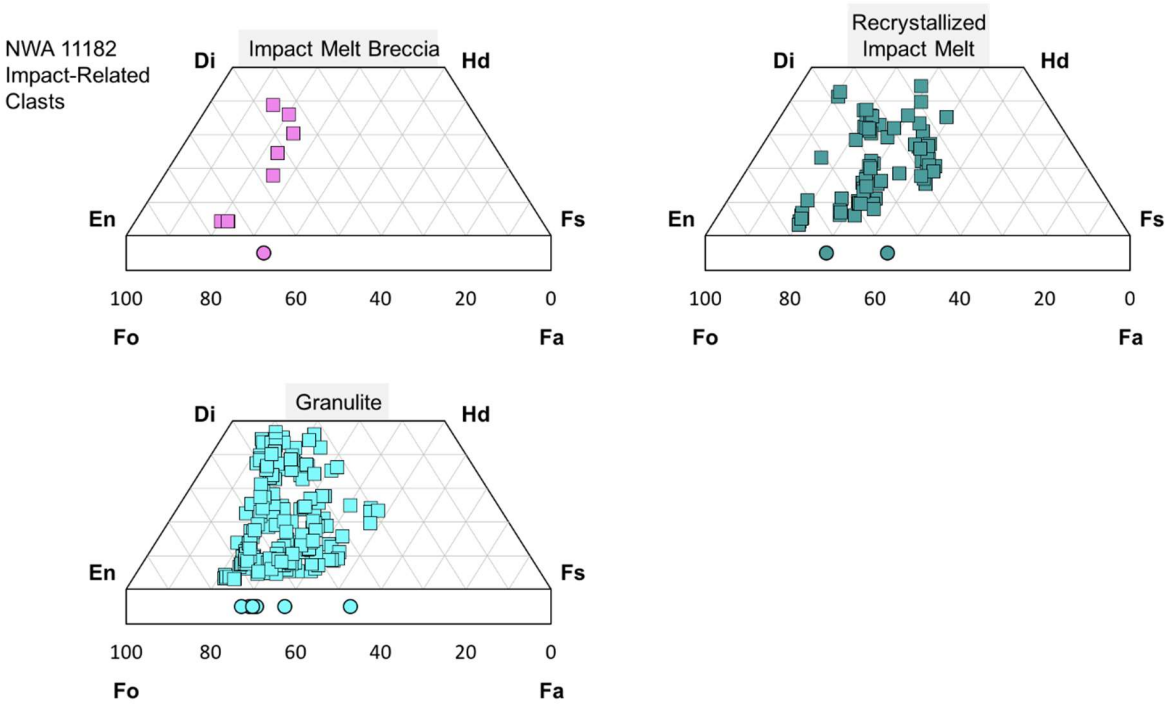

Figure 17: Mafic mineral chemistry of impact-related clasts in NWA 11182.

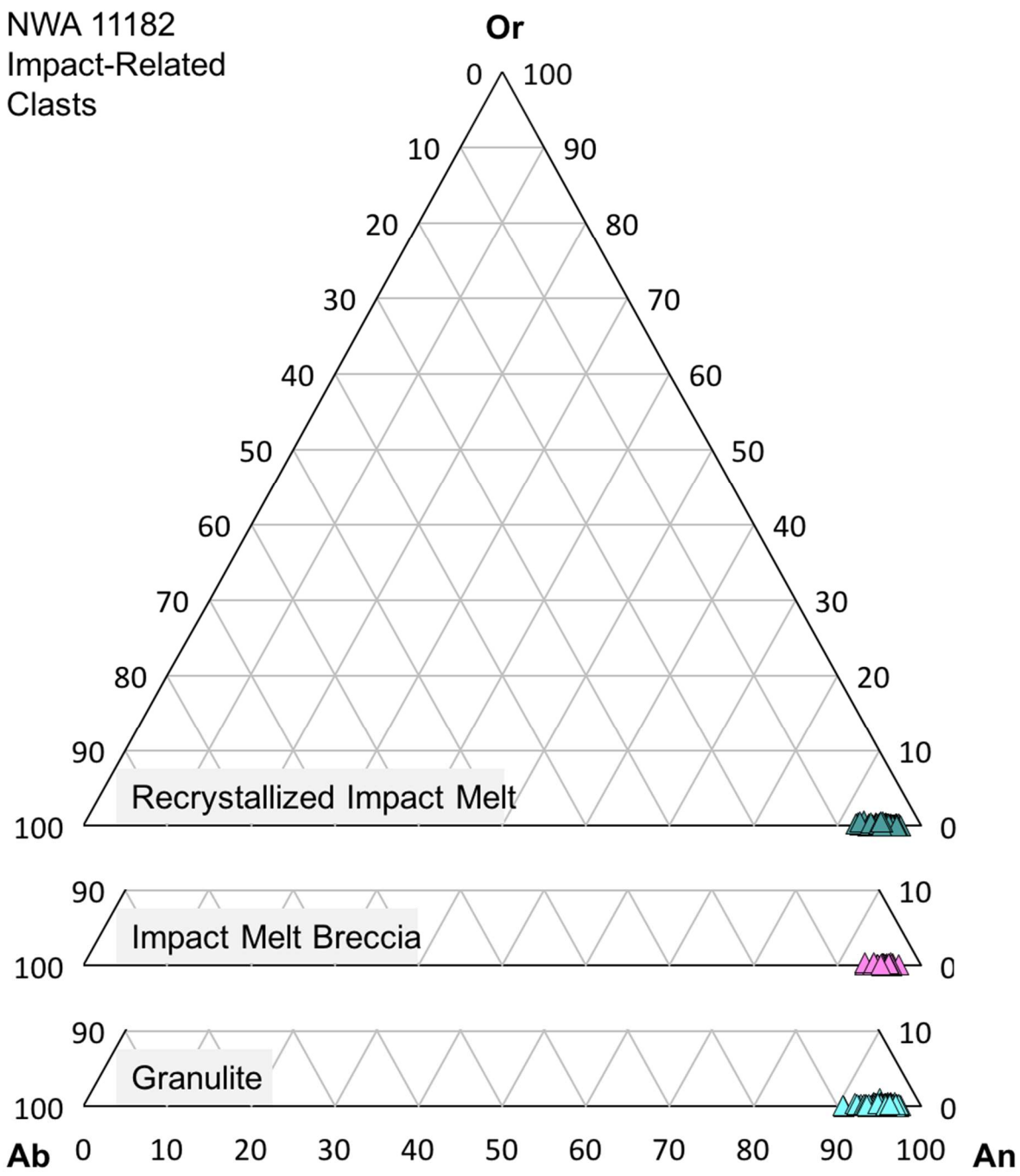

Figure 18: Plagioclase mineral chemistry of impact-related clasts in NWA 11182.

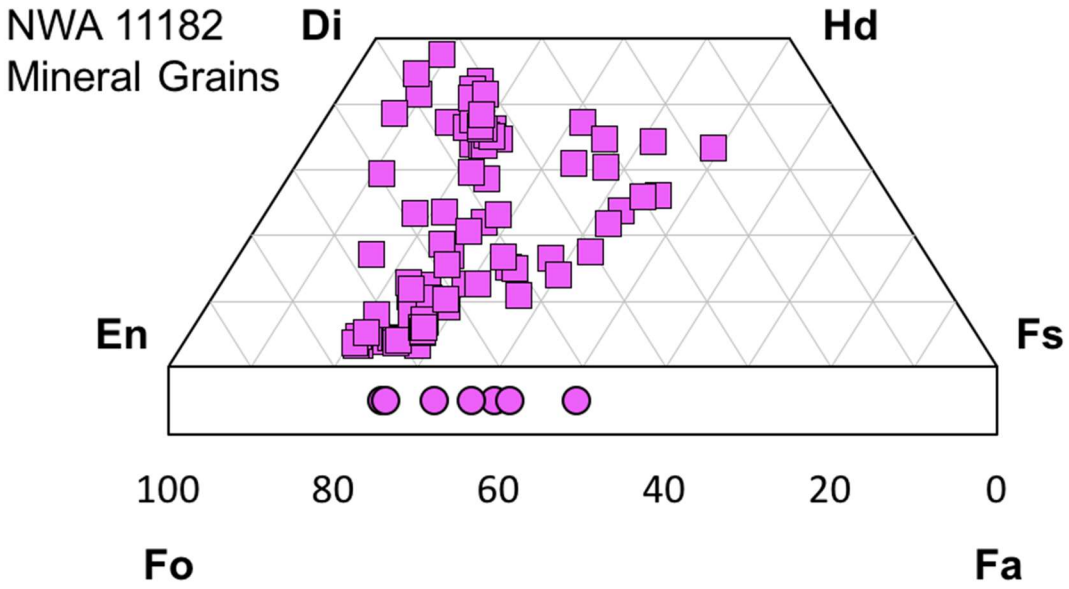

Figure 19: Mafic mineral chemistry of mineral grains in NWA 11182.

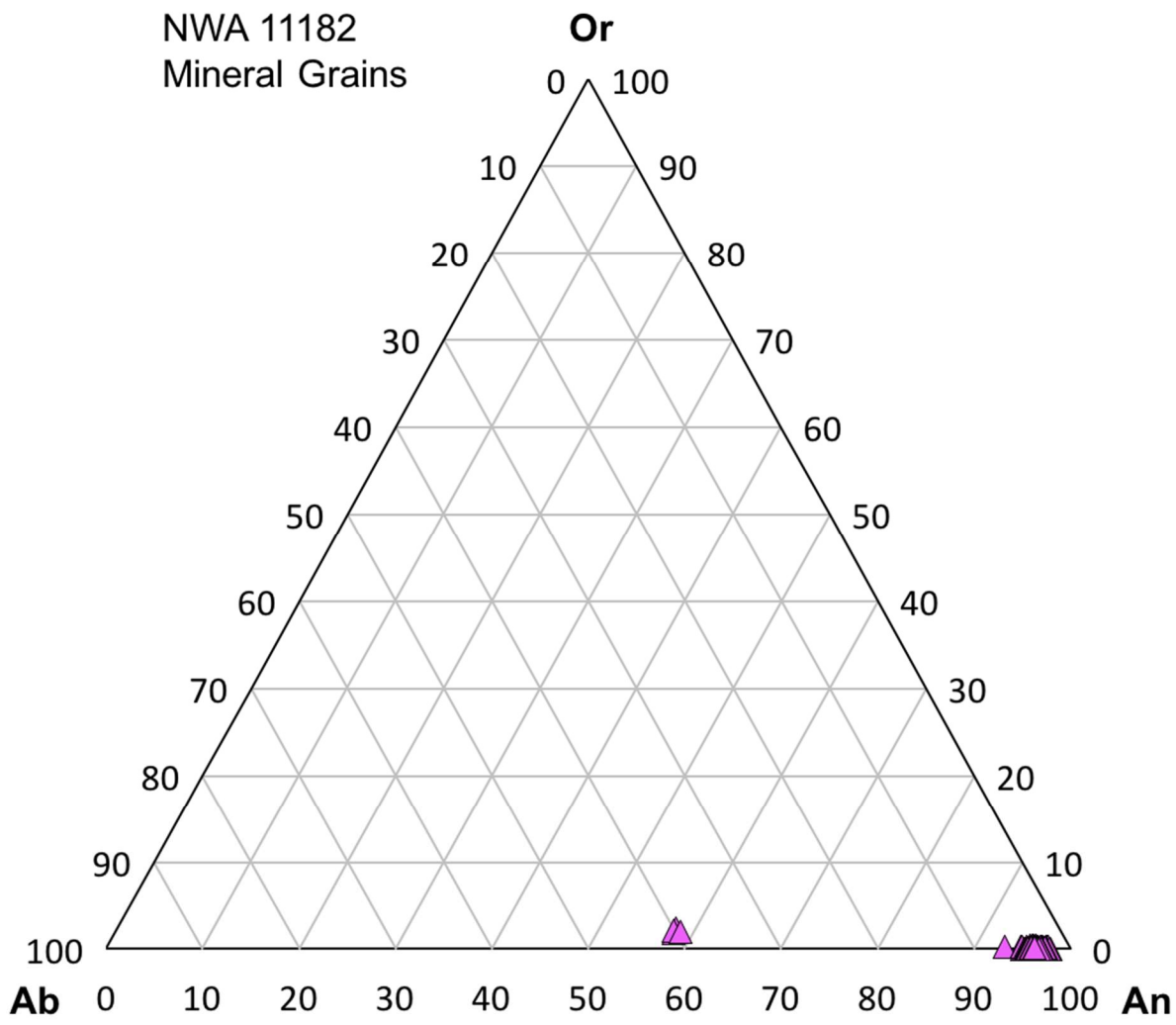

Figure 20: Plagioclase mineral chemistry of mineral grains in NWA 11182.

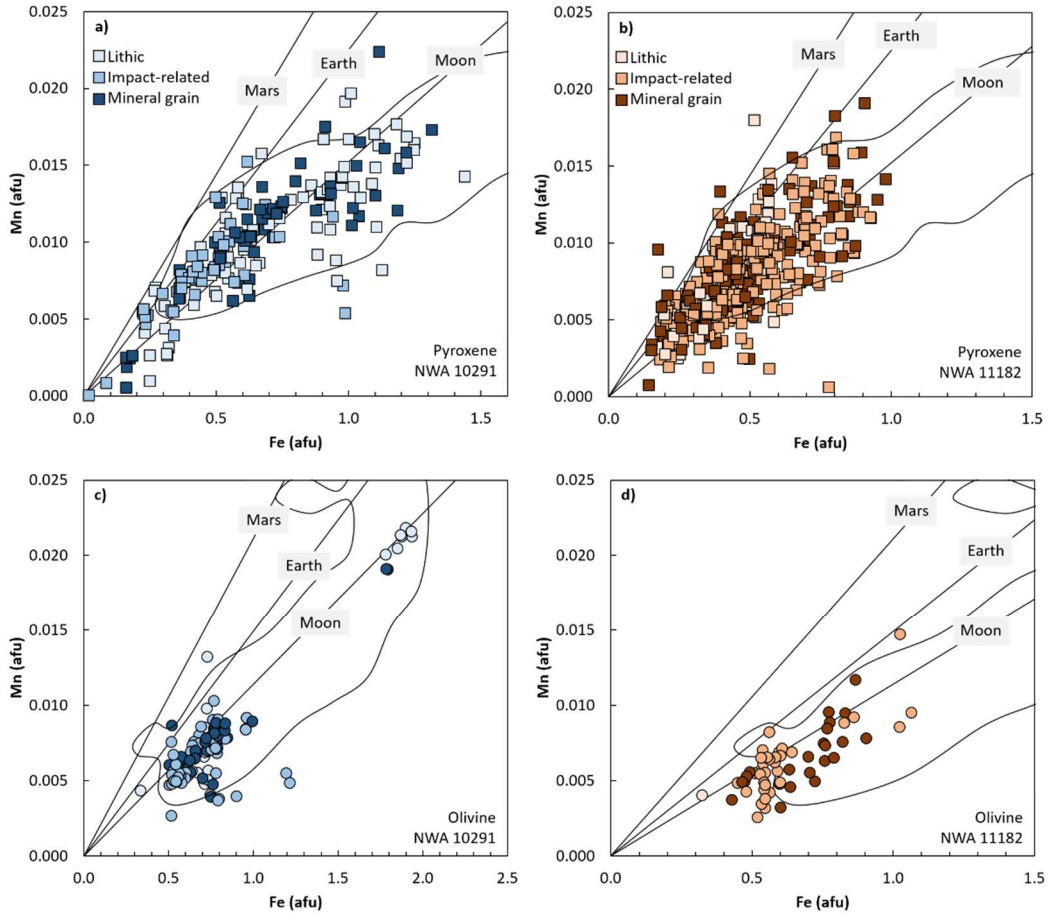

Figure 21: Fe/Mn ratio of pyroxene and olivine in NWA 10291 and NWA 11182.

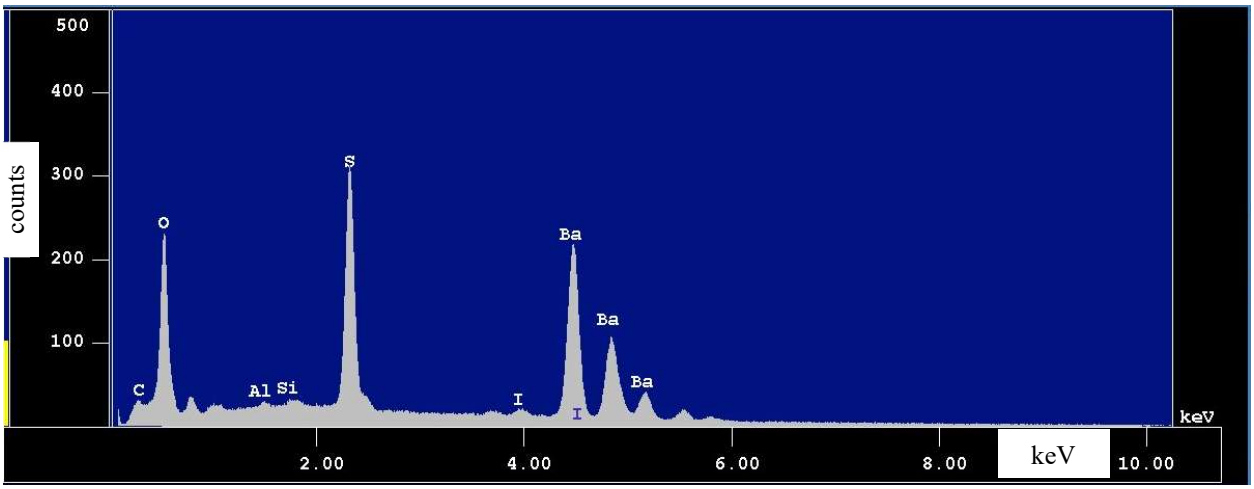

Figure 22: Energy Dispersive Spectroscopy (EDS) spectra of barite grains in NWA 11182.

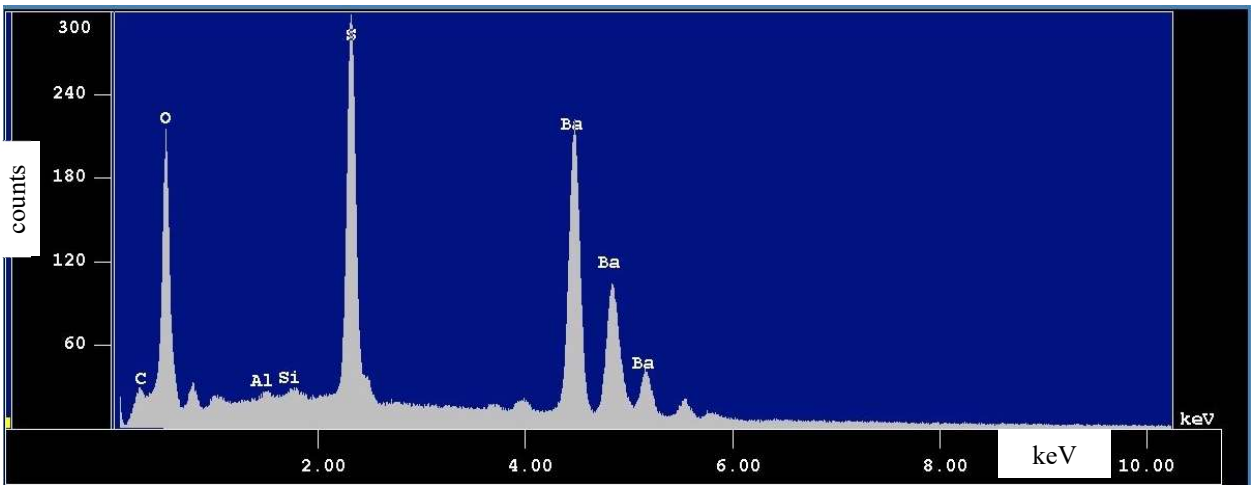

Figure 23: Energy Dispersive Spectroscopy (EDS) spectra of barite vein in NWA 11182.

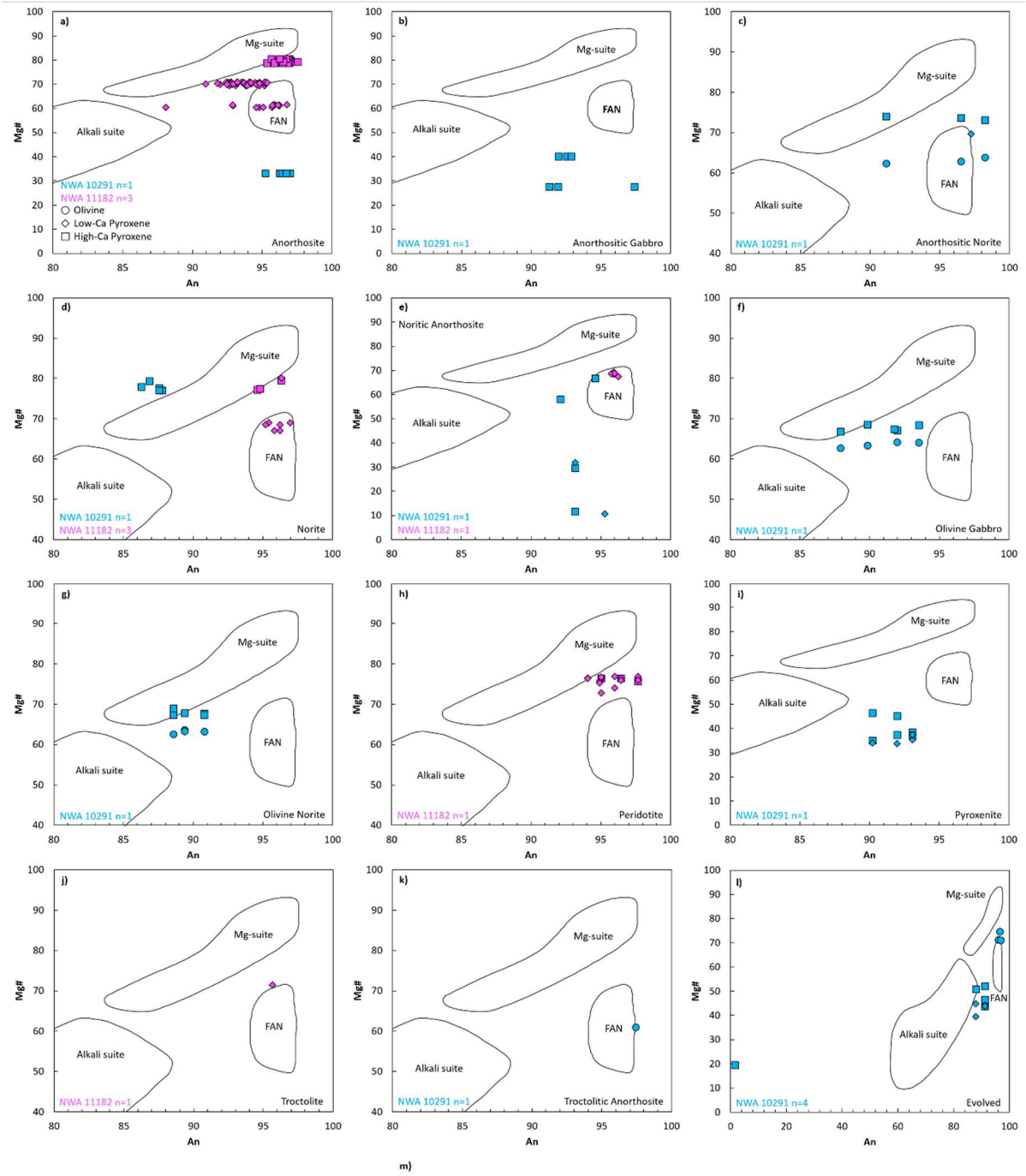

Figure 24: An/Mg# of lithic clasts in NWA 10291 and 11182.

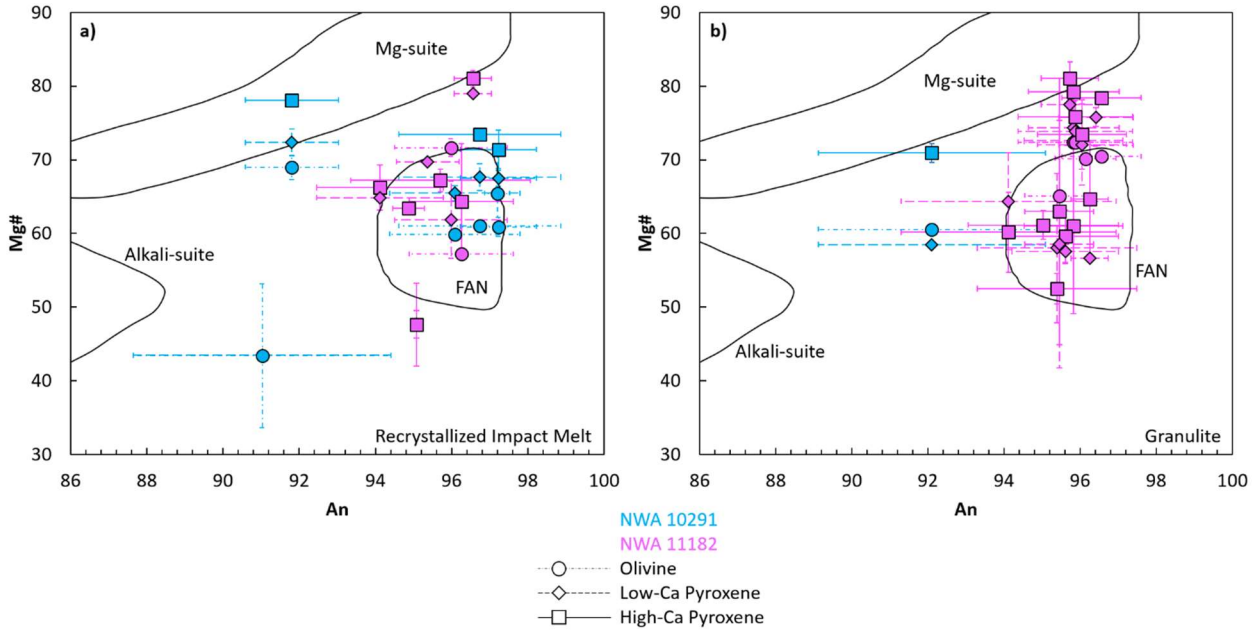

Figure 25: An/Mg# of impact-related clasts in NWA 10291 and 11182.

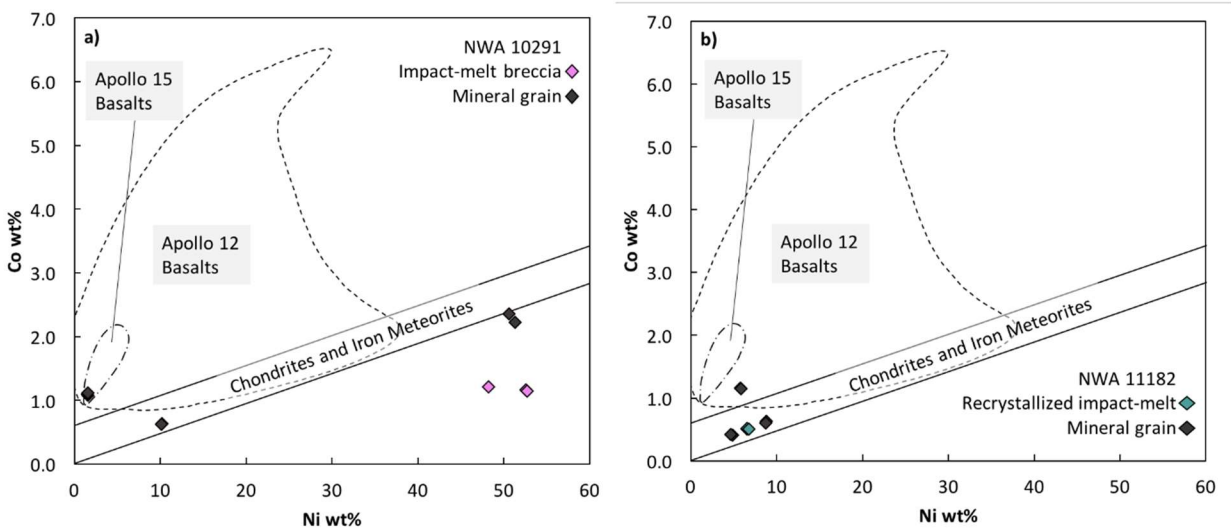

Figure 26: Ni/Co ratios in Fe-Ni metal in NWA 10291 and 11182.

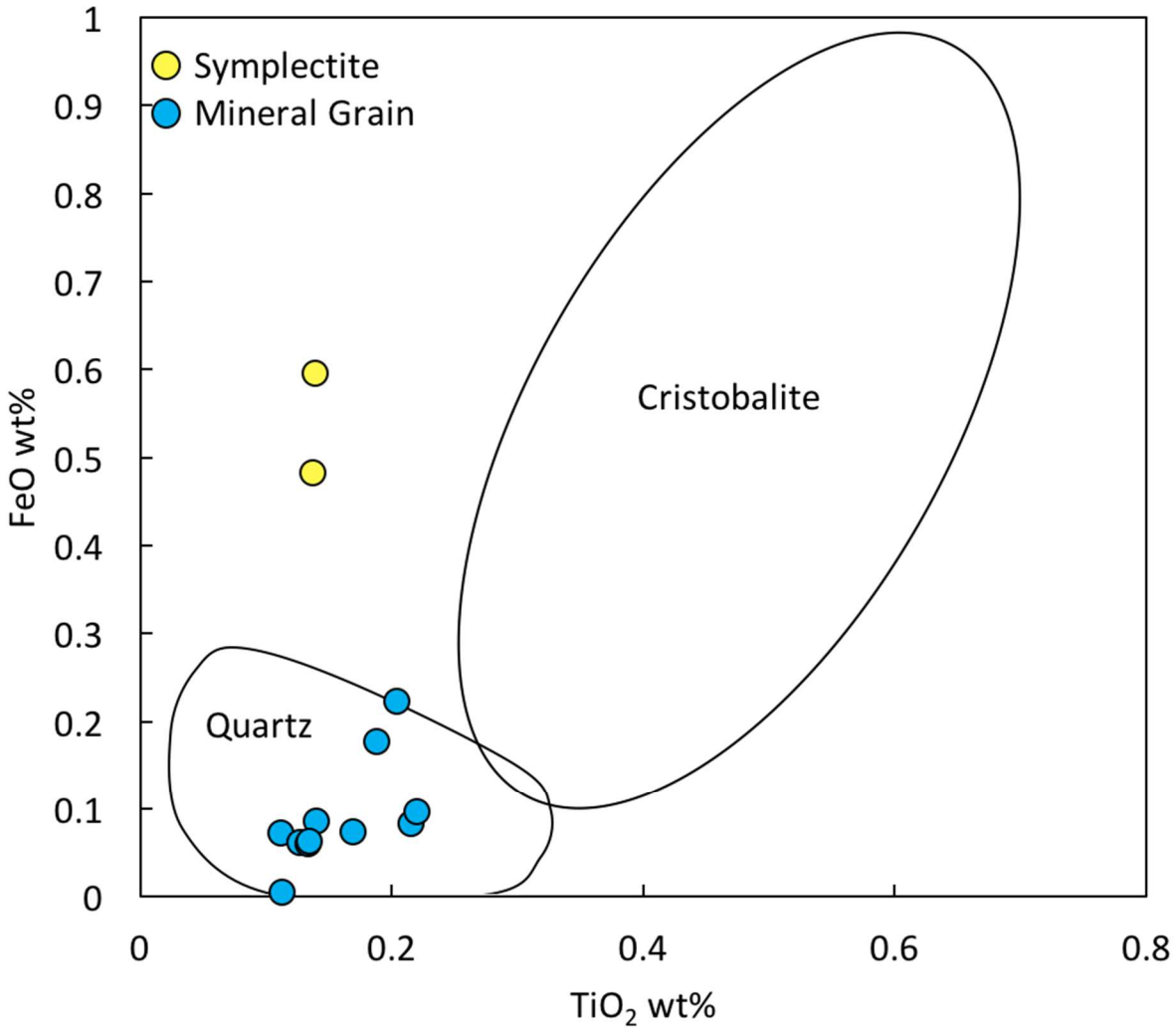

Figure 27: TiO_2/FeO of silica-phases in NWA 10291.

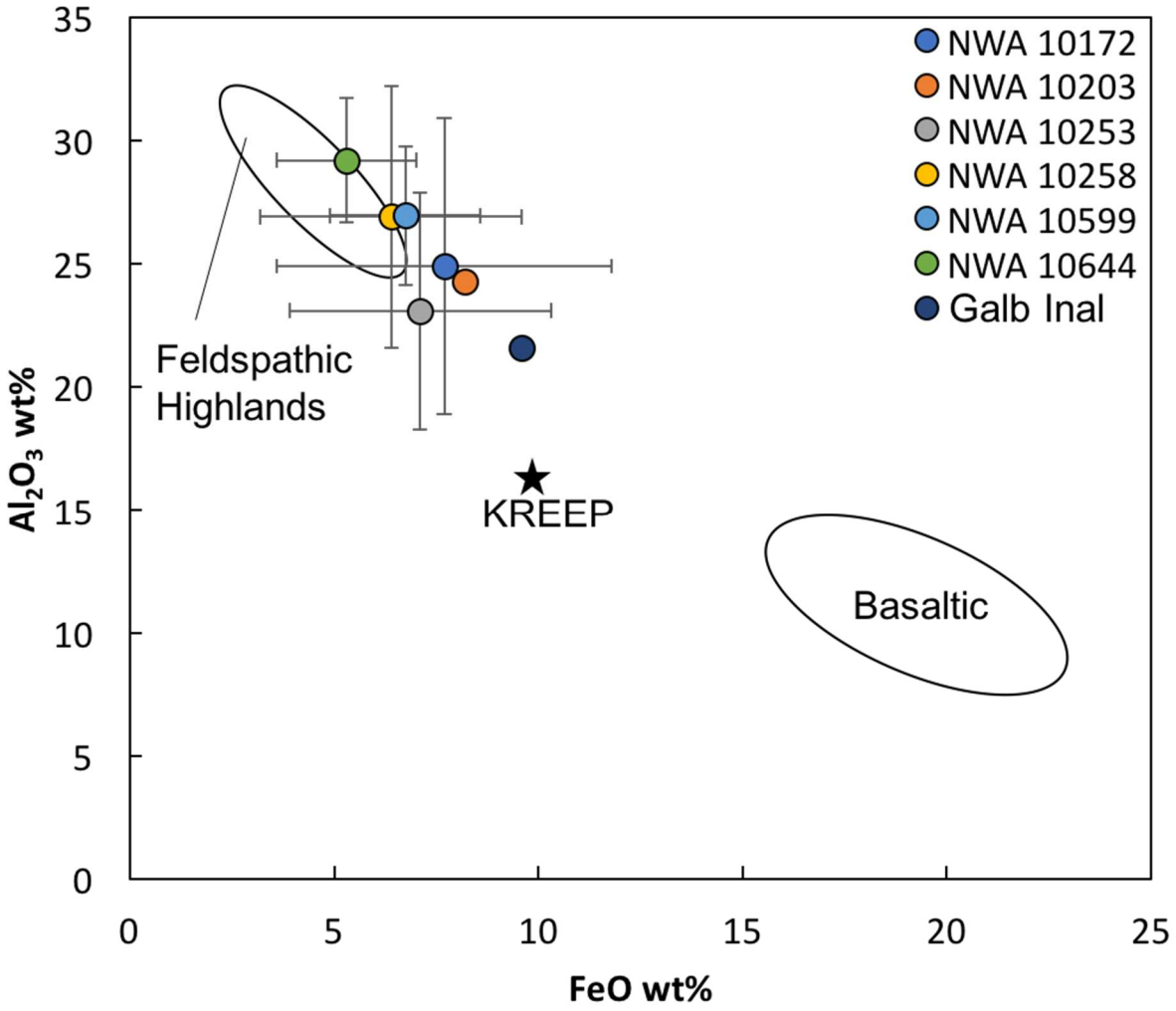

Figure 28: Bulk composition of meteorites paired to NWA 10291.

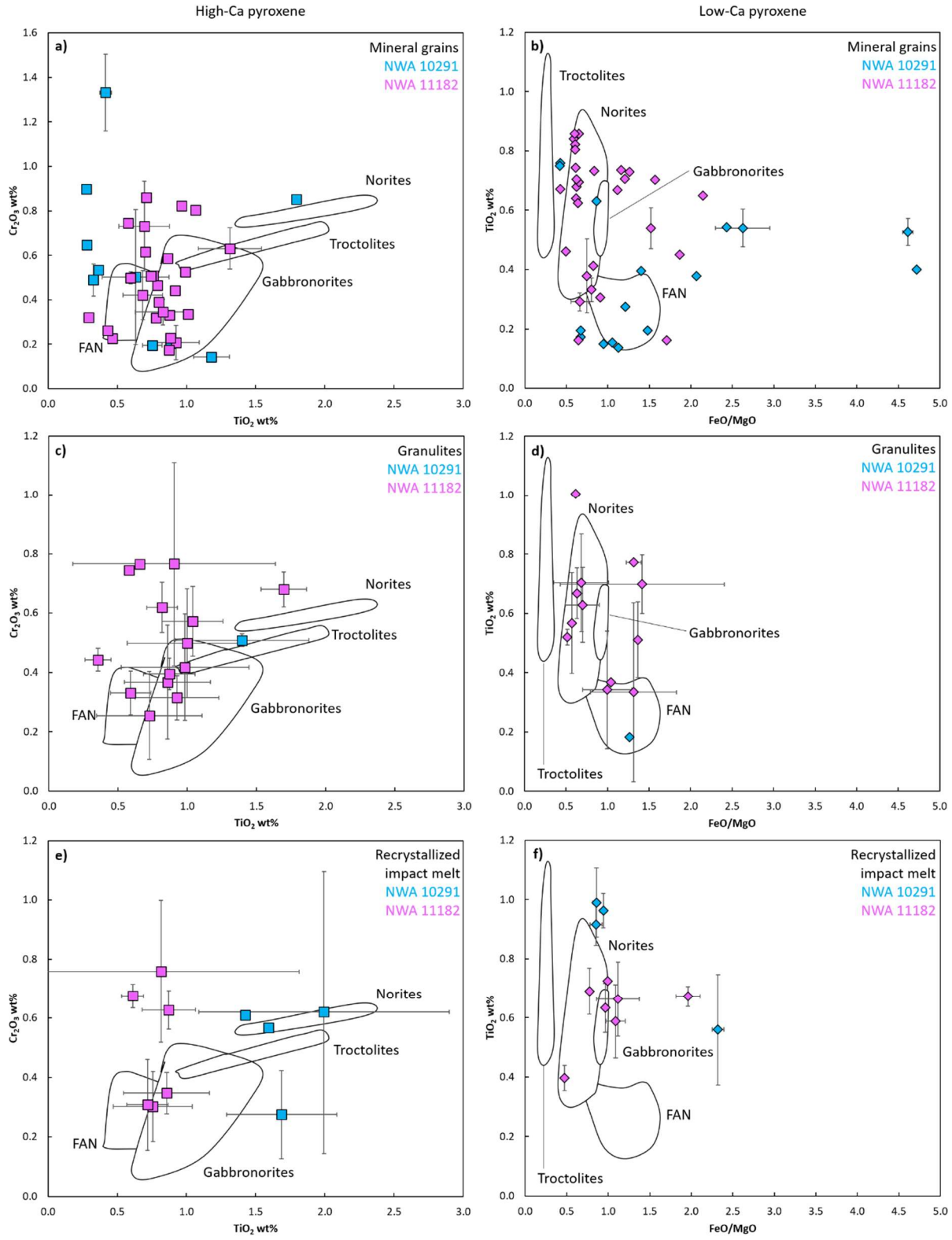

Figure 29: Potential Highland lithology parentage of pyroxene mineral grains, granulites, and recrystallized impact melt in NWA 10291 and 11182.

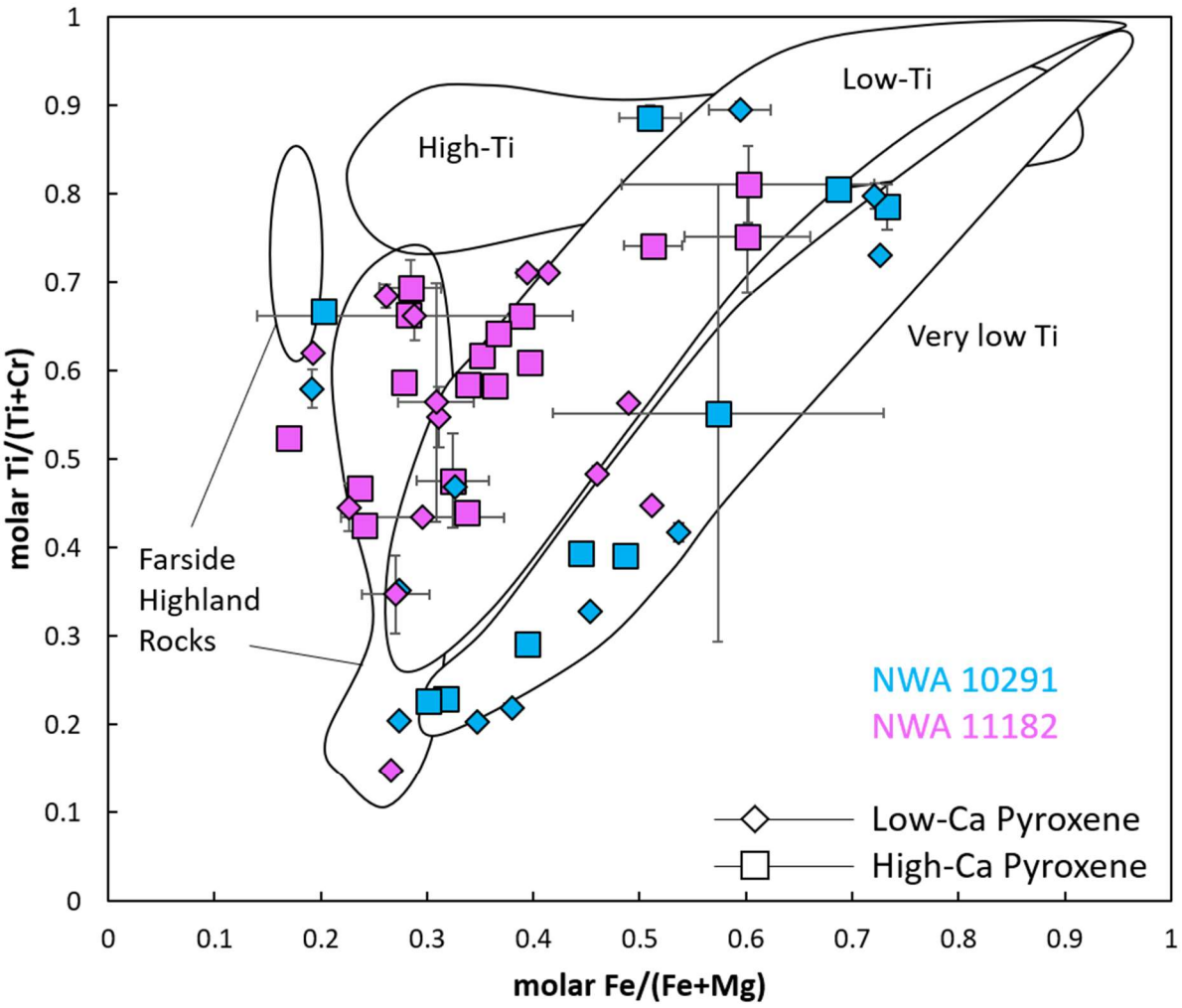

Figure 30: Potential basaltic parentage for pyroxene mineral grains in NWA 10291 and 11182.

Figure 1: Structure of the lunar regolith. Vertical structure of the lunar regolith. Image from the Lunar Sourcebook, Figure 4.22, page 93 (French et al., 1991).

Figure 2: Full Back Scattered Electron (BSE) image of NWA 10291, showing the size, shape, and variety of the different lunar lithologies present.

Figure 3: Full Back Scattered Electron (BSE) image of NWA 11182, showing the size, shape, and variety of the different lunar lithologies present.

Figure 4: BSE images of representative lithic clasts in NWA 10291; a) anorthosite clast composed of a large plagioclase and a small pyroxene; b) fractured anorthositic gabbro clast; c) olivine gabbro with anhedral grain boundaries and ophitic texture, a small evolved clast made of silica and pyroxene rests in the matrix nearby; d) olivine norite with a large olivine and ilmenite inclusion adjacent to a mixture of lath-like plagioclase and pyroxene; e) norite clast composed of plagioclase and pyroxene with olivine and plagioclase grains in the matrix; f) peridotite clast composed of olivine and pyroxene; g) pyroxenite clast that displays exsolution in a flow-like pattern with plagioclase inclusion; h) symplectite clast C19 that shows fine-grained intergrowth of fayalitic olivine and hedenbergite; a plagioclase grain lines on side of the grain boundary; a crack penetrates part of the clast that contains evidence of silica remaining in the hole; i) symplectite clast C21 with intergrowths of fayalitic olivine and hedenbergite; plagioclase resides in a hole in the clast; j) evolved clast composed of exsolved pyroxene with Na-rich plagioclase inclusions; k) evolved clast with exsolved pyroxene and a Na-rich plagioclase inclusion next to a pyroxene mineral grain; the grain boundary shows interaction between the clast and the surrounding melt; plag=plagioclase, pyx=pyroxene, ol=olivine, si=silica, il=ilmenite; yellow dotted line represents the outline of each clast.

Figure 5: BSE images of representative impact-related clasts in NWA 10291; a) granulite clast showing granulitic (rounded) olivine and pyroxene grains set in plagioclase; b-e) recrystallized impact melt with microcrystalline (b, c, e) to skeletal (quenched; d) olivine and pyroxene grains within plagioclase; f-i) microcrystalline, polymict impact melt breccias with various lithological inclusions, such as plagioclase, pyroxene, and olivine mineral grains one impact melt breccia (h) contains an Fe-Ni metal and is next to an evolved lithology containing ilmenite, apatite, and Na-rich plagioclase; plag=plagioclase, pyx=pyroxene, ol=olivine, il=ilmenite, ap=apatite, metal=Fe-Ni metal; yellow dotted line represents the outline of each clast.

Figure 6: BSE images of representative lithic clasts in NWA 11182; a) anorthosite clast containing large fractures that are filled with terrestrial barite; b) norite clast with both low- and high-Ca pyroxene and plagioclase; Na-rich plagioclase grain lies in the matrix to the right; c) noritic anorthosite; this clast is located on the edge of the sample, is heavily fractured, and broken; d) peridotite clast with plagioclase enclosed in pyroxene and a large altered olivine; the altered olivine is pitted and fractured and likely has been terrestrially weathered into iddingsite; plag=plagioclase, pyx=pyroxene, ol=olivine; yellow dotted line represents the outline of each clast.

Figure 7: BSE images of representative impact-related clasts in NWA 11182; a) granulitic low- and high-Ca pyroxene grains enclosed by plagioclase; small inclusions of chromite are present; b) coarse grained granulite clast with poikiolitically enclosed pyroxene and olivine; the olivine shows similar cracks and pits to the peridotite clast and its chemistry has been altered, likely into iddingsite; c) a granulite clast that contains pyroxene and a large altered olivine; d-e) recrystallized impact melt clasts with pyroxene and olivine grains enclosed in plagioclase; f-g) impact melt breccias with microcrystalline pyroxene and larger inclusions of plagioclase,

pyroxene, and olivine grains; plag=plagioclase, pyx=pyroxene, ol=olivine, chr=chromite; yellow dotted line represents the outline of each clast.

Figure 8: BSE images of altered olivine mineral grain in lunar NWA 11182 compared to L6 chondrite Forrest 009; a) altered olivine grain in the matrix of NWA 11182 with pyroxene and plagioclase inclusions; the altered olivine is pitted along the cracks and the chemistry is changed in the cracked section to likely iddingsite; b) altered olivine in L6 chondrite Forrest 009; white arrow points to the "boxwork" structure; modified after Lee and Bland (2004); plag=plagioclase, pyx=pyroxene, ol=olivine.

Figure 9: Mafic mineral chemistry of lithic clasts in NWA 10291. Chemistry of pyroxene and olivine in lithic clasts in NWA 10291; En=enstatite (Mg-rich), Fs=ferrosilite (Fe-rich), Di=diopside (Mg-Ca-rich), Hd=hedenbergite (Fe-Ca-rich), Fo=forsterite (Mg-rich), Fa=fayalite (Fe-rich).

Figure 10: Plagioclase mineral chemistry of lithic clasts in NWA 10291. Mineral chemistry of plagioclase in lithic clasts in NWA 10291; An=anorthosite (Ca-rich), Ab=albite (Na-rich), Or=orthoclase (K-rich).

Figure 11: Mafic mineral chemistry of impact-related clasts in NWA 10291. Mineral chemistry of pyroxene and olivine in impact-related clasts in NWA 10291; En=enstatite (Mg-rich), Fs=ferrosilite (Fe-rich), Di=diopside (Mg-Ca-rich), Hd=hedenbergite (Fe-Ca-rich), Fo=forsterite (Mg-rich), Fa=fayalite (Fe-rich).

Figure 12: Plagioclase mineral chemistry of impact-related clasts in NWA 10291. Mineral chemistry of plagioclase in impact-related clasts in NWA 10291; An=anorthosite (Ca-rich), Ab=albite (Na-rich), Or=orthoclase (K-rich).

Figure 13: Mafic mineral chemistry of mineral grains in NWA 10291. Mineral chemistry of pyroxene and olivine mineral grains in NWA 10291; En=enstatite (Mg-rich), Fs=ferrosilite (Fe-rich), Di=diopside (Mg-Ca-rich), Hd=hedenbergite (Fe-Ca-rich), Fo=forsterite (Mg-rich), Fa=fayalite (Fe-rich).

Figure 14: Plagioclase mineral chemistry of mineral grains in NWA 10291. Chemistry of plagioclase mineral grains clasts in NWA 10291; An=anorthosite (Ca-rich), Ab=albite (Na-rich), Or=orthoclase (K-rich).

Figure 15: Mafic mineral chemistry of lithic clasts in NWA 11182. Mineral chemistry of pyroxene and olivine in lithic clasts in NWA 11182; En=enstatite (Mg-rich), Fs=ferrosilite (Fe-rich), Di=diopside (Mg-Ca-rich), Hd=hedenbergite (Fe-Ca-rich), Fo=forsterite (Mg-rich), Fa=fayalite (Fe-rich).

Figure 16: Plagioclase mineral chemistry of lithic clasts in NWA 11182. Mineral chemistry of plagioclase in lithic clasts in NWA 11182; An=anorthosite (Ca-rich), Ab=albite (Na-rich), Or=orthoclase (K-rich).

Figure 17: Mafic mineral chemistry of impact-related clasts in NWA 11182. Mineral chemistry of pyroxene and olivine in impact-related clasts in NWA 11182; En=enstatite (Mg-rich), Fs=ferrosilite (Fe-rich), Di=diopside (Mg-Ca-rich), Hd=hedenbergite (Fe-Ca-rich), Fo=forsterite (Mg-rich), Fa=fayalite (Fe-rich).

Figure 18: Plagioclase mineral chemistry of impact-related clasts in NWA 11182. Mineral chemistry of plagioclase in impact-related clasts in NWA 11182; An=anorthosite (Ca-rich), Ab=albite (Na-rich), Or=orthoclase (K-rich).

Figure 19: Mafic mineral chemistry of mineral grains in NWA 11182. Mineral chemistry of pyroxene and olivine mineral grains in NWA 11182; En=enstatite (Mg-rich), Fs=ferrosilite (Fe-

rich), Di=diopside (Mg-Ca-rich), Hd=hedenbergite (Fe-Ca-rich), Fo=forsterite (Mg-rich), Fa=fayalite (Fe-rich).

Figure 20: Plagioclase mineral chemistry of mineral grains in NWA 11182. Chemistry of plagioclase in mineral grains in clasts in NWA 11182; An=anorthosite (Ca-rich), Ab=albite (Na-rich), Or=orthoclase (K-rich).

Figure 21: Fe/Mn ratio of pyroxene and olivine in NWA 10291 and NWA 11182. Plot of Fe versus Mn in atoms per formula unit (afu) to indicate planetary parentage. The field represents data of other lunar meteorites from Fagan et al. (2002), Anand et al. (2003), Zeigler et al. (2005), and Joy et al. (2008). Trendlines for Earth, Mars, and the Moon are from Papike et al. (1998) and Karner et al. (2003, 2006).

Figure 22: Energy Dispersive Spectroscopy (EDS) spectra of barite grains in NWA 11182. EDS spectra of terrestrial barite found as grains in NWA 11182.

Figure 23: Energy Dispersive Spectroscopy (EDS) spectra of barite vein in NWA 11182. EDS spectra of terrestrial barite that filled veins in NWA 11182.

Figure 24: An/Mg# of lithic clasts in NWA 10291 and 11182. Anorthite component (An=100*Ca/(Ca+Na)) in plagioclase versus magnesium number (Mg#=100*Mg/(Mg+Fe)) of olivine or pyroxene; a) anorthosite clasts in NWA 10291 are more ferroan than those in NWA 11182; b) anorthositic gabbro clasts in NWA 10291 are ferroan and trend toward alkali enrichment; c) anorthositic norite clast in NWA 10291; d) norite clasts in NWA 11182 are more Ca-rich than those of NWA 10291; e) noritic anorthosite clasts in NWA 10291 show much more varied composition than those in NWA 11182; f) olivine gabbro clasts in NWA 10291 have an intermediate composition between Mg-suite and FAN; g) olivine norite clasts in NWA 10291; h) peridotite clasts in NWA 11182 are compositionally intermediate between Mg-suite and FAN; i)

pyroxenite clasts in NWA 10291 tend toward alkali enrichment; troctolite clasts in NWA 11182 may be similar to FAN; k) troctolitic anorthosite in NWA 10291 may be compositionally similar to FAN; l) symplectite clasts in NWA 10291 are ferroan; m) evolved clasts in NWA 10291 vary compositionally; fields for Mg-suite, FAN, and alkali-suite are from Goodrich et al. (1984) and Mercer et al. (2013). Circle=olivine, diamond=low-Ca pyroxene, square=high-Ca pyroxene, blue=NWA 10291, pink=NWA 11182, n=number of clasts plotted.

Figure 25: An/Mg# of impact-related clasts in NWA 10291 and 11182. Average anorthite component (An=100*Ca/(Ca+Na)) in plagioclase versus average magnesium number (Mg#=100*Mg/(Mg+Fe)) of olivine or pyroxene of impact-related clasts in NWA 10291 and NWA 11182; a) impact melt breccia clasts in both meteorites tend to be of intermediate composition between Mg-suite and FAN; b) recrystallized impact melt in both meteorites varies in composition, which is consistent with the mafic clast compositionally variability; c) granulites in NWA 11182 range from ferroan composition to intermediate between Mg-suite and FAN; granulites in NWA 10291 are more alkali-rich. Symbols denote average mineral composition in a single clast; bars indicate the range of values measured in the mineral. Symbols and colors as in Figure 24.

Figure 26: Ni/Co ratios in Fe-Ni metal in NWA 10291 and 11182. Nickel versus Co element weight percent (el. wt%) of metal grains in both meteorites shows strong indication of exogenous origin; fields from Taylor and Day (2005), Day et al. (2006), and Morland et al. (2019).

Figure 27: TiO2/FeO of silica-phases in NWA 10291. Composition of silica-phases found in NWA 10291 indicates that the polymorph is quartz for the mineral grains; silica in symplectites is higher in FeO, which is most likely related to the formation of the symplectites; fields from Seddio et al. (2015).

Figure 28: Bulk composition of meteorites paired to NWA 10291. Bulk composition of meteorites paired to NWA 10291; fields from Korotev et al. (2003) and data from Ruzicka et al. (2015, 2017) and Bouvier et al. (2016, 2017).

Figure 29: Potential Highland lithology parentage of pyroxene mineral grains, granulites, and recrystallized impact melt in NWA 10291 and 11182. Plots of high- and low-Ca pyroxene in mineral grains, granulites, and recrystallized impact melt in NWA 10291 and 11182 used to determine if they are related to Highland rocks. Symbols denote average mineral composition in a single clast; bars indicate the range of values measured in the mineral. Fields are from Treiman et al., (2010) and references therein.

Figure 30: Potential basaltic parentage for pyroxene mineral grains in NWA 10291 and 11182. Plots of high- and low-Ca pyroxene mineral grains in NWA 10291 and 11182 to identify basaltic parentage of material in the meteorites; while NWA 11182 shows a strong affinity to highland material, pyroxene grains in NWA 10291 trend mostly in the very low Ti basalt and high Ti basalt fields. Symbols denote average mineral composition in a single clast; bars indicate the range of values measured in the mineral. Fields are from Mercer et al. (2013) and Hill et al. (2019) and references therein.